Raghbendra Tiwari

Frequency Converter Solutions and Control Methods for Variable Speed Operation of Pumped Storage Plants

Doctoral thesis

NTNU
Norwegian University of Science and Technology
Thesis for the Degree of
Philosophiae Doctor
Faculty of Information Technology and Electrical
Engineering
Department of Electric Energy

NTNU
Norwegian University of
Science and Technology

Raghbendra Tiwari

Frequency Converter Solutions and Control Methods for Variable Speed Operation of Pumped Storage Plants

Thesis for the Degree of Philosophiae Doctor

Trondheim, December 2023

Norwegian University of Science and Technology
Faculty of Information Technology and Electrical Engineering
Department of Electric Energy

NTNU
Norwegian University of
Science and Technology

Smooth seas do not make skillful sailors.
                                    - Unknown

Abstract

Pumped storage hydropower plants (PSHP) are widely used for bulk energy storage around the world. The variable speed operation of these plants further enables their capability to regulate the power in pump mode as well. In most PSHPs, the variable-speed operation is achieved by the combination of a doubly-fed induction machine (DFIM) and a reversible pump turbine (RPT). The importance of this energy storage system is increasing at the same rate as the penetration of intermittent renewable energy sources like wind and solar into the grid. To better utilize these pollution-free energy sources, the PSHPs with fixed-speed synchronous machine units are being considered for conversion to variable-speed operation.

The variable-speed operation of a synchronous machine in a fixed-speed PSHP can be executed by introducing a full-size converter between the generator transformer and the stator of the machine. The converter decouples the machine rotation from the grid frequency, and thus the speed of the machine can be adjusted to vary the pumping power and to allow the RPT to run at the maximum possible efficiency over a wide range of operations.

There exist several converter topologies for variable speed drives in industrial applications. This thesis focuses mainly on the converter topologies and their control to enable the variable speed operation of the synchronous machine in a fixed-speed PSHP.

First, the converter topologies like neutral point clamped converter, active neutral point clamped converter, and modular multilevel converter have been evaluated and compared for this application based on the application-associated requirements. The analytical loss equations for the semiconductor devices have been derived and used for analyzing the loss at different operating conditions of the converter.

Second, the control method of these converters has been proposed for fast startup of the plant in both pump and turbine operation, fast mode transition from the turbine to pump and vice versa, and during low voltage ride through (LVRT) conditions on the grid terminals. The methods have been tested and verified in the laboratory using a full-size two-level three-phase converter, a synchronous machine, and a hardware-emulated reversible pump turbine.

With the full-size converter, critical operations like the startup in pump mode and the mode transition from the turbine to pump and vice versa can be executed quite faster than the existing DFIM technology. The startup can be accomplished in less than 30 seconds, and the mode transition can be performed in less than a minute which is crucial in following the varying power generation from intermittent renewable energy sources.

The summary of contributions of this PhD research is listed as follows:

1. Analytical loss equations for the PWM modulated ANPC converter and Modular Multilevel Converter have been derived. These equations are a useful tool for loss analysis of these types of converters and determining the rating of the semiconductor devices.

2. A detailed loss analysis of multilevel converters has been carried out and the best possible converter solution to enable the variable speed operation in a fixed speed pumped storage power plant has been proposed. This method can serve as a converter selection method for this technology.

3. A Control strategy to start and stop the power plant in turbine (generation) mode and pump mode has been proposed and verified in a laboratory with a 100 kVA prototype experimental arrangement.

4. Control strategy for the transition of mode from the turbine to pump and vice versa has been proposed and verified in the laboratory. This feature is crucial in adapting intermittently varying power generation from renewable sources like wind and solar.

Acknowledgments

First of all, I would like to sincerely thank my supervisor, prof. Roy Nilsen for trusting me as the best candidate for this research topic and for the knowledge I have gained through numerous discussions over the course of this PhD. I would also like to thank my co-supervisor, prof. Arne Nysveen for providing insight into the overall picture of this research and giving valuable inputs on our publications. I would like to extend my thanks to HydroCen, which funded this research project.

I would like to thank William Gullvik for his immense support while establishing the laboratory setup. It would have been difficult to execute this work without your support. I would also like to thank our project partner SINTEF Energy Research. A few special people I cannot fail to acknowledge are Olve Mo, Kjell Ljøkelsøy, Salvatore D´Arco, and Santiago Sanchez Acevedo, who supported me immensely in the laboratory.

I would like to thank Thomas Haugen for his extremely intelligent and important work in the development of the control platform for executing the laboratory work. I would also like to thank all the people working in the laboratory who were involved in the installation of the machines. I also thank Anyuan Chen for his help while working in the laboratory.

My sincere thanks go to prof. em. Torbjørn Nielsen and associate prof. Pål-Tore Storli for their help in understanding the characteristics of the reversible pump turbine. Before those discussions, the reversible pump turbine was a mysterious machine to me.

My thanks also go to my fellow PhD candidates of that time Anirudh B. Acharya, Tor Inge Reistad, Aravinda Perera, Andreas Giakannis, Gard Rødal, and Tobias N. Ubostad for all the knowledge-building technical discussions, and the refreshing

chats.

Contents

List of Tables

List of Symbols

Acronyms

AFE	Active Front End
ANPC	Active Neutral Point Clamped
BIGT	Bi-Mode Insulated Gate Transistor
CAN	Controller Area Network
CCS	Circulating Current Suppression
CFSM	Converter Fed Synchronous Machine
DFIM	Doubly Fed Induction Machine
EMI	Electromagnetic Interference
GTO	Gate Turn-Off
IGBT	Insulated-Gate Bipolar Transistor
IGCT	Integrated Gate-Commutated Thyristor
IEGT	Injection Enhanced Gate Transistor
IM	Induction Machine
LCI	Load-Commutated Inverter
LVRT	Low Voltage Ride Through
MMC	Modular Multilevel Converter
MOSFET	Metal-Oxide-Semiconductor Field-Effect Transistor
MTPA	Maximum Torque Per Ampere
NPC	Neutral Point Clamped
PSHP	Pumped Storage Hydropower Plant
PWM	Pulse Width Modulation
RPT	Reversible Pump Turbine
SM	Synchronous Machine
STATCOM	Static Compensator
THD	Total Harmonic Distortion
TSO	Transmission System Operator
VSC	Voltage Source Converter

Chapter 1

Introduction

1.1 Background

At present, pumped storage hydropower plants (PSHPs) are realized with a re-versible pump turbine (RPT) and an AC machine (generator/motor) connected to the same shaft. In most PSHPs, the AC machine is a synchronous machine di-rectly connected to the grid, and therefore, the set of machines runs at a constant speed depending upon the frequency of the grid regardless of the amount of water flowing into the turbine/pump. This also leads to constant power consumption in pump mode. However, it is a well-proven theory that the turbine/pump operates at optimal efficiency only if its speed is varied according to the variation in the water flow. Further, the variation in speed also provides the control of power in the pumping mode which contributes to the frequency stability of the grid.

In most PSHPs around the world, variable speed operation of hydraulic machines is currently being achieved with the help of Doubly Fed Induction Machine (DFIM) technology. In this technology, a frequency converter of approximately 20–30% capacity of the stator rating is required to achieve a variation of $\pm$ 10% in speed [1]. Even though the system has been widely used for over 30 years, it still ex-hibits a long start-up procedure that takes 5–20 minutes. The procedure includes depressing the water below the runner level, altering the phase sequence of the stator connection, short-circuiting the stator winding, and synchronization to the grid. Depending upon the type of converter connected to the rotor winding, it may need an additional arrangement (e.g., soft starter or pony motor) to accelerate the machine to the synchronous speed. Moreover, it makes the system unable to dy-namically switch the operation from generating mode to pumping mode or vice versa.

1

The fast start-up, dynamic mode switching, and speed variation are important requirements to balance the ever-increasing number of renewable energy sources being introduced to the grid. The faster the control of the system is, the more effectively the pollution-free renewable energy can be utilized. This can be achieved by decoupling the turbine/generator sets from the AC grid using a full-size back-to-back converter-fed synchronous machine (CFSM). In a fixed-speed pumped storage plant, the converter is placed between the AC machine and the generator transformer to enable variable-speed operation. Such full-size converters can be designed to deliver high starting torque, which in turn starts the system in 30–60 seconds in pump mode, and even faster in turbine mode. Therefore, this thesis mainly focuses on the converter topology and the control of such a full-size converter.

1.2   Scope of the research

The role of the pumped storage plants is becoming more prominent as more and more renewable energy sources like wind and solar are being connected to the grid. Fast start-up of PSHPs in pump mode and fast transition from generation to pumping mode and vice versa are foreseen as important requirements to adapt to the varying power generation from renewable energy sources. Therefore, the full-size converter-fed synchronous machine is going to be the primary technology for the pumped storage plants for variable speed operation and for the fast control of power flow to the grid. However, there is no well-known method in the literature for selecting the converter topology and its control for pumped storage plant applications. Therefore, the thesis focuses on addressing the methods for the selection of converter topology and control of the converters for PSHP application as shown in the schematic of Fig. 1.1. The details on the state-of-the-art of this technology and the basis of the research questions are presented in Chapter 2.

The thesis is organized into multiple chapters, each dedicated to addressing specific research questions that have been formulated to explore and explain various aspects of the chosen topic.

Research question 1: There exist many types of converter topologies for industrial applications. What type of converter topology can fulfill the requirements of converting a fixed-speed pumped storage plant with a synchronous machine to a variable-speed pumped storage plant?

Research question 2: When the synchronous machine is isolated from the grid using a back-to-back converter, can the speed of the machine be allowed to deviate more from its steady state value to contribute to the virtual inertia? The conventional way of designing the mechanical time constant (T_m) of the electrical
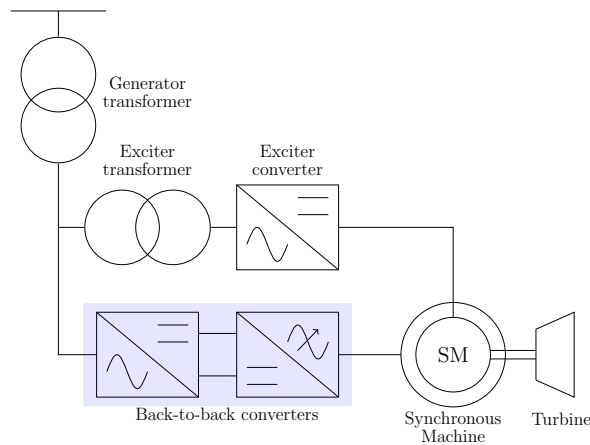
Figure 1.1: Schematic of Converter Fed Synchronous Machine Technology. The selection of the converter topology and the development of control strategies for the back-to-back converters (shaded in the figure) is the main focus of this research.

machine in a hydropower plant is $T_m/T_w > 6$, where T_w is the acceleration time of the water through the penstock. Can this be relaxed for the electrical machine?

Research question 3: When the synchronous machine is connected to the grid via a back-to-back converter, how the setup can be controlled to start and stop the machine? How the transition of the mode from turbine to pump and vice versa can be executed seamlessly to adapt to the power generation from wind and solar energy sources?

Research question 4: What will be the consequences of a voltage dip on the grid side in the operation of the power plant while running in the pump mode or in the generation mode in such a full-size converter fed operation?

1.3 Methodology

The research in this thesis consists basically of two parts: the converter solution for the application, and the control methods for the converters. The modeling of hydraulics systems and simulation studies have been the basis for finding the requirements of the converters. A set of analytical equations have been derived to determine the loss at different operating points of the possible converter topologies. A detailed evaluation and comparison of the converter topologies have been carried out to determine the method of selection of the converter for this application.

The secondary layer control method for the operation of the pumped storage plant does not rely on the converter topologies. Therefore, the proposed control strate-

gies have been experimentally verified in a laboratory with a two-level three-phase back-to-back converter-fed synchronous machine of 100 kVA. The reversible pump-turbine characteristics have been emulated using another set of back-to-back converters connected to a squirrel cage induction machine. The control software for the synchronous machine converter has been developed during this work using Avnet Picozed System-on-Module. The secondary control layer and the emulation of the pumped storage plant components are executed in MATLAB-based OPAL-RT real-time simulation system.

1.4 Major contributions of the thesis

The research conducted over the course of this Ph.D. program has resulted in the following noteworthy contributions:

1. Analytical loss equations for the PWM modulated ANPC converter and Modular Multilevel Converter have been derived. These equations serve as useful tools for assessing losses in these converter types and for determining the appropriate semiconductor device ratings.

2. A detailed loss analysis of multilevel converters has been carried out and the best possible converter solution to enable the variable speed operation in a fixed speed pumped storage power plant has been proposed. This approach can serve as a converter selection method for this technology.

3. A Control strategy to start and stop the power plant in turbine (generation) mode and pump mode has been proposed and verified with a 100 kVA prototype experimental arrangement in a laboratory.

4. Control strategy for the transition of mode from the turbine to pump and vice versa has been proposed and verified in the laboratory. This feature is crucial for effectively adapting to intermittent power generation from renewable sources like wind and solar.

1.5 Outline of the thesis

Chapter 1 presents the brief background of the application and identifies the research questions. The contributions of the thesis and the list of publications are also presented.

In Chapter 2, the state-of-the-art of variable speed operation of the pumped storage plant has been discussed. Two major technologies, DFIM and CFSM are described and the advantages of CFSM for the effective integration of renewable

energy sources like wind and solar are presented. This chapter establishes the identification of the research gaps the thesis has addressed.

Chapter 3 presents the overall model of a pumped storage plant including the waterway, tunnel, and reversible pump turbine. The simulation results with various control parameters of the governor are analyzed to check how the slow response of the governor can contribute to less oscillation in the penstock and waterway. The impact of the speed variation on the size of the converter is also discussed.

In Chapter 4, the modeling of a wound rotor synchronous machine, which is commonly used in fixed-speed pumped storage power plants, is presented. The modeling has been further simplified to mathematically determine the control parameters for the stator and exciter current controllers.

Chapter 5 presents the possible converter topologies suitable for enabling variable speed operation of a pumped storage power plant. Analytical loss equations are derived to calculate the loss at critical speed points to dimension the semiconductor devices. The converter topologies are compared for various figures of merits relevant to this application.

In Chapter 6, the converter topology for the grid-side converter is discussed. The reactive power compensation and the virtual inertia contribution using the inertial energy of the rotating shaft, and its impact on the size of the converter are also outlined.

In Chapter 7, the overall control method for the full-size converter-fed operation of a pumped storage power plant is presented. A method to seamlessly switch the operation mode from pump to turbine and turbine to pump is proposed. In addition, the low-voltage-ride-through cases in both pump and turbine modes are tested. The results from a laboratory prototype to verify these control methods are also presented.

Finally, Chapter 8 presents the conclusions of this research work and further suggestions that could not be carried out within the time frame of this research.

1.6   List of publications

1.6.1   Publications related to this PhD research

J1: **Raghbendra Tiwari**, Roy Nilsen, Olve Mo, and Arne Nysveen, "*Control Methods for Operation of Pumped Storage Plants with Full-size Back-to-Back Converter Fed Synchronous Machines*", IEEE Transactions on Industry Applications, Nov-Dec, 2023, DOI: 10.1109/IAS48185.2021.9677283.

C1: **Raghbendra Tiwari**, and Roy Nilsen, "*Analytical Loss Equations for Three Level Active Neutral Point Clamped Converters*", IECON 2020 - 46th Annual Conference of the IEEE Industrial Electronics Society, Singapore, 2020, pp. 1285–1290, DOI: 10.1109/IECON43393.2020.9254393.

C2: **Raghbendra Tiwari**, Roy Nilsen, and Arne Nysveen, "*Active NPC Converter for Variable Speed Operation of Pumped Storage Hydropower Plant*", IECON 2020 - 46th Annual Conference of the IEEE Industrial Electronics Society, Singapore, 2020, pp. 1211–1216, DOI: 10.1109/IECON43393.2020.9255403.

C3: **Raghbendra Tiwari**, Roy Nilsen, and Arne Nysveen, "*Modular Multilevel Converter for Variable Speed Operation of Pumped Storage Hydropower Plant*", PCIM Europe digital days 2021; International Exhibition and conference for Power Electronics, Intelligent Motion, Renewable Energy and Energy Management, Germany, 2021, pp. 1361–1368.

C4: **Raghbendra Tiwari**, Roy Nilsen, and Arne Nysveen, "*Evaluation and Comparison between Multilevel Converters for Variable Speed Operation of Pumped Storage Power Plants with Full-size Converters*", 2021 IEEE IAS Annual Meeting, 2021, DOI: 10.1109/IAS48185.2021.9677283.

C5: **Raghbendra Tiwari**, Roy Nilsen, and Olve Mo, "*Control Strategies for Variable Speed Operation of Pumped Storage Plants with Full-size Converter Fed Synchronous Machines*", 2021 IEEE Energy Conversion Congress and Exposition (ECCE), 2021, pp. 61–68, DOI: 10.1109/ECCE47101.2021.959504.

The publications C1, C2, C3, and C4 are related to the content of Chapter 5, which discusses the selection of the converter topology for this application. Similarly, papers C5 and J1 are related to Chapter 7, which presents the control methods and the experimental results. The overview of the publications and their correlation to the contributions are presented in Fig 1.2.

1.6.2   Other publications during the PhD research

The following publications were prepared in the course of PhD study but have not been included as part of this thesis.

C6: **Raghbendra Tiwari**, and Roy Nilsen, "*Active Compensation of Unbalanced Load Currents in Grid-Connected Voltage Source Converters*", International Conference on Power Electronics and ECCE Asia (ICPE 2019 – ECCE Asia), May 2019, Busan, Korea (South).
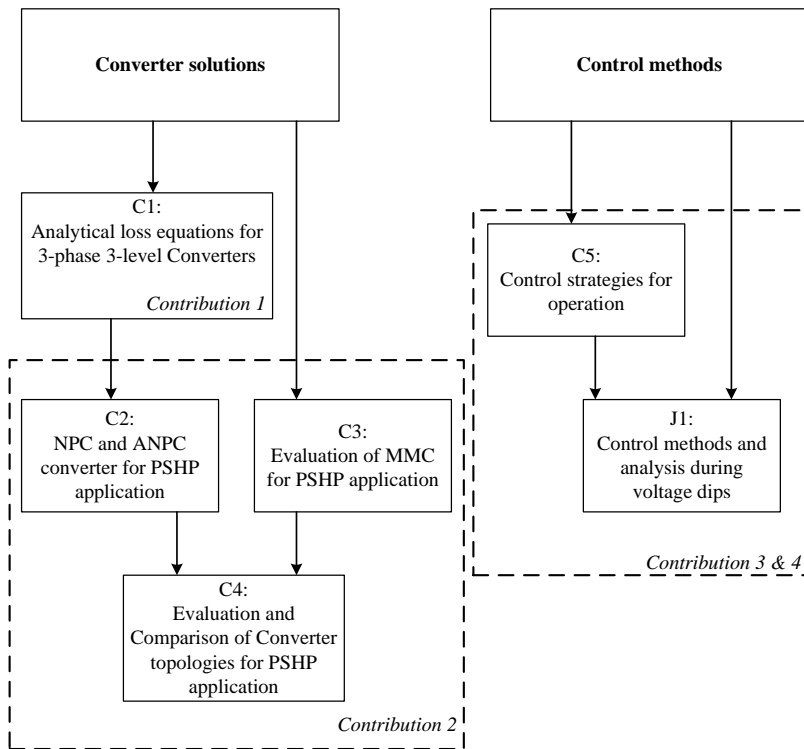
Figure 1.2: An overview of the publications and their correlation with the contributions of this PhD research.

Chapter 2

State-of-the-Art

2.1 Introduction

Pumped storage plants are normally realized in two ways. The first type is where the synchronous machine is connected to two different hydraulic machines: a Francis or Pelton turbine and a pump, also known as the ternary set of machines. In this case, the electrical machine always rotates in the same direction and the power is produced when connected to the turbine. The power is consumed from the grid when connected to the pump and the water is pumped from the lower reservoir to the upper reservoir of the power plant. The second type is where the synchronous machine is connected to a reversible pump turbine (RPT). In this case, the power is produced when the RPT rotates in one direction (when the water flows from the upper to the lower reservoir) whereas power is consumed, and the water is pumped when the RPT is rotated in opposite direction. The direction of rotation is changed by altering the phase sequence of the stator terminals of the electrical machine. Normally, this is done using disconnecting switches either at low voltage switchboard or at high voltage switchyard. In both types of pumped storage plants, the set of machines run at a fixed speed, and the power in pump mode cannot be regulated. In addition, switching from pump mode to generation mode or vice versa is not instantaneous. It takes several minutes to start up in pump mode as the turbine casing needs to be dewatered and the machine set needs to be accelerated close to synchronous speed using an auxiliary arrangement (pony motor or auxiliary turbine or coupling with the other machine in the same power plant).

However, it is a well-known theory that the speed of the hydraulic machines (pump or turbine or RPT) needs to be varied as the water flow and the net head vary to achieve the best efficiency point of operation. Moreover, the variable speed
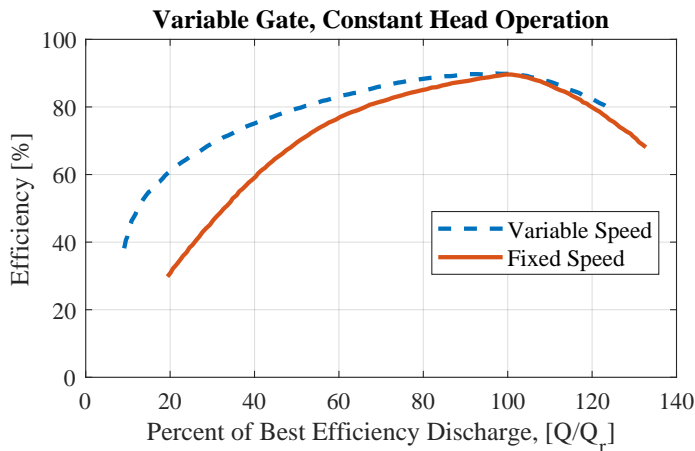
Figure 2.1: Efficiency characteristics of variable-speed and fixed-speed turbines (reproduced from [2]).

operation increases the efficiency in the longer range of power variation as shown in Fig. 2.1 [2]. In the '90s, variable speed operation of pumped storage plants was introduced using doubly fed induction machine (DFIM) technology. In DFIM technology, the stator of the induction machine is directly connected to the grid, and the rotor winding is supplied by a frequency converter of approximately 20-30 % power rating of the machine [1, 3]. The speed of the rotor is controlled by regulating the slip frequency of the rotor supply, also known as slip power recovery. This technology was introduced to control the power in pump mode while keeping the base load plants, which were nuclear power plants, at relatively constant power generation. There exist variable speed pumped storage plants with DFIM technology ranging from a few megawatts to a single unit of 400 MW. A list of large-scale plants with DFIM technology is presented in [4].

Cycloconverters, which are based on thyristors as semiconductor devices, are primarily used as the rotor power converter in DFIM technology. Due to the natural commutation characteristics of the thyristors, the maximum output frequency is typically one-third of the input frequency. Therefore, it cannot accelerate the machine close to the synchronous machine, and it cannot be used as a startup converter. An auxiliary arrangement as in the case of the fixed-speed pumped storage plant is required to start the system in pump mode. With the development of IGBT, there are a few new power plants where two-level three-phase back-to-back converter topology is also employed. This type of rotor converter can be used to start the machine in pump mode from a standstill by short-circuiting the stator winding. The water from the turbine housing needs to the dewatered as the converter is not large enough to overcome the frictional torque produced by the rotation of the

turbine in the water.

In the last decade, the development of renewable energy sources like wind and solar has remarkably increased. The motive for the operation of the pumped storage plant at variable speed has shifted from balancing the load to balancing the intermittent generation. As the world is moving toward clean energy, the target is always to avoid curtailment of production from these renewable energy sources. Therefore, it demands pumped storage power plants and other energy storage systems to store and produce the power depending upon the status of these intermittently varying sources. This may require a fast start-up of the pumped storage plants and, in some cases, a fast transition from generation to pump mode and vice versa. As described earlier, DFIM technology is unable to carry out fast start-up and mode transitions. A full-size converter to the stator winding of the machine as in the case of industrial drives is the solution to this problem if the required size of the converter can be achieved. Considering the retrofit of the already existing fixed-speed pumped storage plant, this solution is even more cost-effective as it does not require the machine to be converted to DFIM by replacing it with a new type of rotor and having a smaller converter. Even though DFIM can become a competitive solution in terms of cost, it cannot provide dynamic features like a fast start-up and fast transition of the operational modes.

Semiconductor devices and industrial drive technologies are still advancing toward high-power converters. The commercially available size of industrial drives is approaching 50 MW. The thyristor-based LCI converters in the range of 100 MW already exist with some known issues of lower order harmonics torque ripple and high harmonics current on the grid side as well. Therefore, this has not been considered a proper solution for hydropower applications. In [5], it is claimed that a full-size converter is justifiable for pumped storage power plants with a single unit of up to 100 MW for those with today's technology. Beyond that capacity, the space occupied by the converter and the cost associated with it encourages the use of DFIM technology where a smaller converter is required. Therefore, pumped storage hydropower plants with machines in the range of hundreds of MW have DFIM to achieve variable speed operation. As semiconductor device technology is rapidly developing, this limit could increase in the future when devices with higher current ratings are available. Referring to the high-power semiconductor devices available, 100 MVA size has been taken as a reference for this research and the possible solutions have been proposed and compared. A survey of the synchronous machines in hydropower around the world shows that the synchronous machines with a 100 MVA rating have a stator voltage of around 13–15 kV. The application also demands that the retrofit of the fixed-speed plants to variable speed should be carried out with minimum equipment. The additional transformers to match the

stator voltage and the generator transformer voltage should preferably be avoided. This leads to the fact that the converter must achieve an output voltage equal to the rated voltage of the stator to deliver a transformerless solution. Transformerless connection is important for a retrofit project because the space in an underground power plant is well optimized during construction and it becomes very difficult to accommodate additional transformers between the stator and the machine-side converter and between the grid-side converter and the grid transformer.

The medium voltage industrial drives usually employ three-level neutral point clamped (NPC) or active neutral point clamped (ANPC) converters for voltages in the range of 3–6 kV. The two–level three-phase converters for medium voltage drives application are not considered because of high harmonics and high voltage steps at the output terminals. A matrix converter can produce an output voltage up to 86% of its input voltage [6, 7], and hence, cannot provide a transformerless connection in an existing setup. In [8], a comparison between NPC and ANPC converters has been carried out for the pumped storage power plants and shows that ANPC can yield approximately double the torque NPC can provide around zero speed, i.e., during startup in pump mode. Modular multilevel converters had been very popular for high-voltage DC transmission systems but during the last decade, several studies have been carried out on employing them for the drives application. Since the modular structure of MMC makes it easy to achieve any voltage level, it is an attractive solution provided the challenge of capacitor voltage swing in the low-frequency regions is addressed [9, 10, 11]. Due to the aforementioned reasons, NPC, ANPC, and MMC topologies have been considered as the possible alternatives for the transformerless retrofit of the fixed speed PSHP to enable variable speed operation.

The cycle efficiency of a pumped storage plant has been experienced to be in the range of 70%–85% [12]. The cycle efficiency of the Linthal pumped storage plant is claimed to be more than 80% [13]. The start-up time is 120 seconds (not mentioned whether gen mode or pump mode) and 240 seconds to switch from pump mode to generating mode.

One of the advantages of variable speed operation is that the range of operation of the turbine increases significantly. In a fixed-speed turbine, the power cannot be changed to lower than about 40% of rated capacity due to cavitation [3]. The operation of the Goldisthal power plant with variable speed using DFIM technology demonstrates that the units with a variable speed system can be regulated from 40 MW to 265 MW, whereas the units with synchronous machines can be regulated only from 100 MW to 265 MW [14].

2.2   History of variable speed operation of pumped storage plants

The first pumped storage plant was built in Switzerland in 1907 [15]. At that time, the plant was realized using a ternary set of machines: a pump, a turbine, and an electrical machine. After the introduction of reversible pump-turbine by Voith in 1937, the size of the plant machinery became robust [16]. PSHPs became popular for bulk energy storage even though the energy density is significantly low. Based on the potential energy stored ($\rho g h$ = density of water x acceleration due to gravity x head) in the water at the upper reservoir with a typical gross head of 500 m, the energy density is about 1.36 kWh/m^3 compared to the 250-670 kWh/m^3 of Li-ion batteries [17]. Despite having very low energy density, PSHP is cost-effective because the storage pond is naturally available.

The first commercial power generation from a nuclear reactor came in 1954 at Obninsk Nuclear Power Plant of 6 MW [18] and continued to grow as base power plants in several countries around the world. As the power ramp-up and ramp-down time for nuclear power plants are very long and inefficient, pumped storage power plants were considered for operation at variable speeds to produce and consume variable power, especially in pump mode, to maintain the power balance in the grid and a steady grid frequency. In that context, the first commercial unit with variable speed capability using a Doubly Fed Induction Machine (DFIM) was commissioned at the Yagisawa Pumped storage power plant in Japan in 1990 [19]. Since then, many large units of up to 460 MW have been installed around the globe.

Due to the complicated and slow starting process of DFIM technology, full-size CFSM technology is now being discussed extensively for fast integration of pollution-free renewable energy sources like wind and solar. One of the four units of 100 MW in Grimsel-2 pumped storage plant in Switzerland has already adopted this technology in 2013 to take advantage of the flexibility provided by it [20, 21]. In addition, a direct MMC ac/ac full-size converter of 80 MW has recently been installed at Malta Upper Stage Project in Austria to enable the variable speed operation of the existing fixed speed infrastructure [22].

2.3   Historical overview of power electronics in drive applications

The variable speed operation of the electrical machines in applications like passenger lifts in mines and railway locomotives was first solved by tandem machines. One of the most popular methods introduced by Harry Ward Leonard in 1891 was named the Ward Leonard method. The invention of mercury arc vacuum tubes in 1902 paved the way for the power electronics era. These vacuum tubes made

possible the development of AC-DC rectifiers (1910), DC-AC inverters (1920), and variable-frequency drives (around 1920) [23, 24]. The grid-controlled vacuum tubes (equivalent to gate-controlled thyristors) also led to the connection of variable frequency sources.

The major revolution in power electronics took place in the 1950s with the invention of the thyristor at Bell labs and its commercialization by General Electric (GE). Thyristors replaced most of the vacuum tube-based converter topologies in the following years [25, 26, 27].

Thyristors were used in the already existing cycloconverter topology for ac-ac conversion without an intermediate link. Due to only natural commutation being possible in thyristors, the output frequency of the cycloconverter was limited to one-third of the input frequency. Still, it proved to be useful for several applications like railways and propulsion systems [24]. Later in the 1990s, pumped storage power plants needed to be controlled in pump mode, and high-power converters were required to feed the rotor winding of very large wound rotor induction machines. As the slip frequency of the induction machine is very low, cycloconverters proved to be the best solution at that time.

The Gate turn-off (GTO) thyristor was introduced by GE in the mid-1980s and it simplified the implementation of field-oriented control and ac drives became the dominating technology in high-power industrial applications. The further modified version of GTO with an integrated gate circuit called an Integrated Gate Commuted Thyristor (IGCT) was developed by ABB and Mitsubishi in the 1990s with improved performance. This semiconductor device is still preferred for high power converter topologies [25, 26, 28, 29]. The applications of MOSFETs and BJTs were limited to smaller drives and electronics.

The Insulated Gate Bipolar Transistor (IGBT) was introduced in the 1980s, and its fast switching capability led to the development of highly efficient low-voltage and medium-voltage drives. With the availability of IGBT for high-power applications, various multilevel converter topologies were also introduced at different times: Matrix converter (1980), Neutral point clamped converter (1981), ANPC converter (2001), and Modular multilevel converter (2003) [25, 30, 31].

With the availability of high-power semiconductor devices and converter topologies, it became possible to achieve converter size for pumped storage power plants. Since a small converter is required to enable variable speed in a doubly fed induction machine, it was introduced in this type of unit.

2.4   Doubly fed induction machines (DFIM) technology

In a pumped storage plant with DFIM technology, the stator winding is connected to the grid via a circuit breaker and a phase reversal arrangement, and the rotor winding is fed via a converter as shown in Fig. 2.2. The type of converter can be a cycloconverter, back-to-back two-level, multilevel, or any other type depending on the voltage and power rating. The phase sequence of the stator connection is altered while changing the mode of operation from the turbine to the pump or vice versa. In DFIM, the speed normally varies in the range of $\pm 10\%$, and the power varies approximately by 30 % with this speed variation. The upper and lower limit of the speed is limited by the suction and pressure side cavitation in the turbine. The size of the converter required for such rotor side converters is typically 10-30 % of the stator rating for a $\pm 10\%$ variation in speed [32].

The Ohkawachi power plant installed in 1993 has one unit of 400 MVA Doubly fed induction machines with speed variation from 330 rpm to 390 rpm and the rotor is fed by a 72 MVA cycloconverter [33]. The Goldisthal pump storage plant has two units of 300 MW (340 MVA) operating as doubly fed induction machine units for variable speed operation and has cycloconverters of 100 MVA for each unit to supply the rotor winding. The cycloconverter drives the machine from -10% to +4 % of the rated speed of 333 rpm. In addition, a 66 MVAr harmonics wideband power filter is also installed at the point of common coupling to reduce the impact of harmonics due to cycloconverters [34].
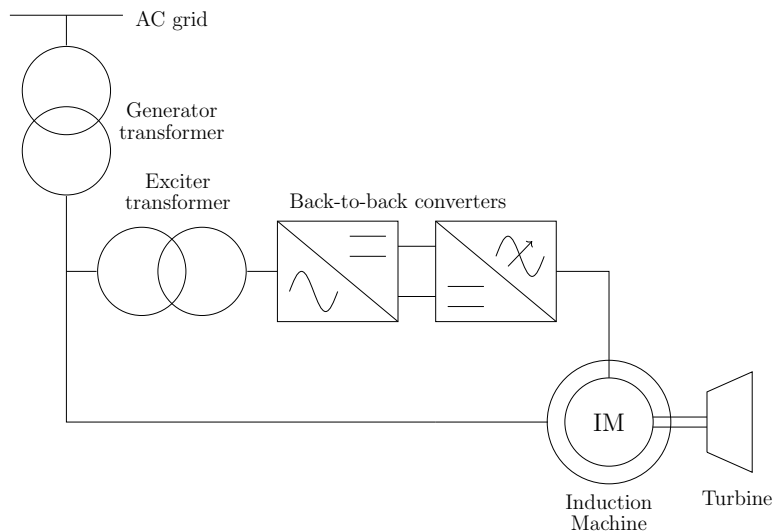
Figure 2.2: Schematic of Doubly Fed Induction Machine Technology. The three-phase winding on the rotor is fed by a cycloconverter or back-to-back voltage source converters.

At Linthal Pumped Storage Plant, two units of 250 MW are of DFIM type and the rotor winding is fed by a three-level NPC converter. The same type of converter is used in 255 MW DFIM machines at Tehri pumped storage plant in India [35]. In Tehri PSHP, the speed variation is 230.8 rpm $\pm 7.5\%$ and the converter for the rotor circuit is a five-channel three-level NPC converter of 25 MVA (5 MVA per channel) [36]. The Frades II hydropower has also deployed a two-level back-to-back converter for supplying the rotor winding of a 433 MVA machine. The size of the rotor-side converter is 45 MVA and that of the grid-side converter is 62 MVA. The speed variation is -6.67% to +1.67% around its synchronous speed of 375 rpm which provides a power variation of 25-100% in generation mode and 78-100% in pump mode [37].

The power plants that are incorporated with Cycloconverters for DFIM arrangement still need a separate converter or soft starter while starting in pump mode as the Cycloconverter cannot produce an output frequency close to the rated frequency to accelerate the machine to the synchronous speed.

2.5   Converter fed synchronous machines (CFSM) technology

The CFSM technology requires a full-size converter for the stator winding in addition to the excitation converter as presented in Fig. 2.3. The load-commutated inverter (LCI) topology was initially used for the control of CFSM and is still in use for a few particular applications. The typical applications are compressors and extruders in oil & gas industries, blast furnace blowers, wire rod mills in metal industries, and starters for gas turbines and hydro turbines in pumped storage hydropower plants [38].

One of the alternatives to enable variable speed operation in fixed-speed pumped storage plants with a synchronous machine is to change the salient pole rotor of the machine to the three-phase wound rotor and convert the machine to a DFIM. The rotor can then be fed by a relatively smaller variable frequency drive as was demonstrated by ABB as a pilot project in one unit of 10 MW, 13.8 kV at Compuerto Hydropower Plant in Spain [39].

The full-size converter-fed synchronous machine provides several operational flexibilities like a fast startup in pump mode, a fast transition from the turbine to pump mode, and vice versa. These features lead to integrating renewable energy sources more effectively and efficiently. Such technology is foreseen as the future of pumped storage plants. Grimsel-2 in Switzerland has one of its 100 MW units running in pump mode with a 2×50 MW full-size back-to-back connected ANPC converters [20] whereas Malta Upper Stage Project in Austria has incorporated 80 MW direct MMC for the same purpose [22].
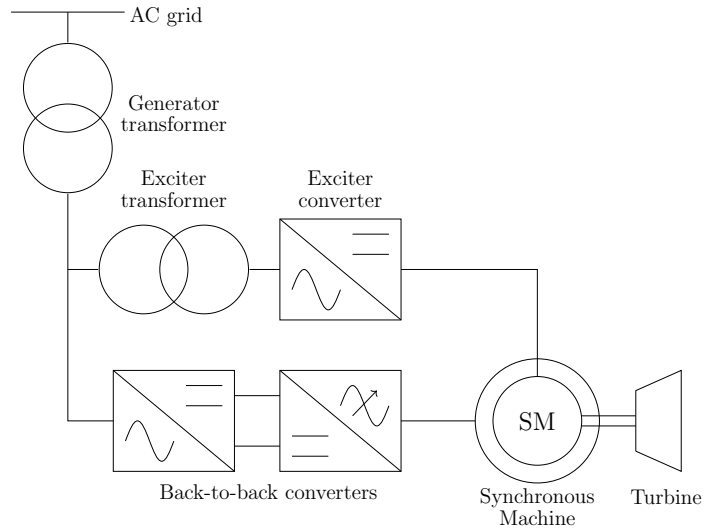
Figure 2.3: Schematic of Converter Fed Synchronous Machine Technology. The stator winding is fed by a large converter of at least the same power capacity as the stator. The field winding is fed by a dc supply directly from a converter as shown here in the case of the static excitation system. In many cases, the field winding is supplied by a rotating exciter and a rotating rectifier system mounted on the same shaft, known as a brushless excitation system.

One of the major benefits of variable speed operation is that it can regulate the power in both pump and generation mode whereas the conventional one can only regulate in generation mode. The downside of variable-speed operation is that it needs a large converter, which is challenging for an existing plant to accommodate in the powerhouse cavern.

2.6 Advantages and disadvantages of CFSM over DFIM

2.6.1 Advantages

Besides the fact that CFSM requires a very large converter compared to that required in a DFIM configuration, CFSM exhibits several advantages over DFIM.

In a DFIM machine, the rotor carries a very high current and the expansion in the rotor bars complicates the design of the machine. The monitoring of the expansion and the handling arrangement requires special attention [40].

In the DFIM configuration, the phase sequence of the stator connection is altered to rotate the machine in the opposite direction while changing the mode of operation from pump to turbine and vice versa. This is normally done in a high-voltage switchyard, and the process delays the transition of mode from one to the other.

For retrofit projects with fixed-speed pumped storage plants, only a full-size converter is required for CFSM configuration, whereas a new rotor, phase sequence changer, and relatively small converter are required for DFIM configuration. Still, the latter does not exhibit a fast transition of the operational modes.

In the case of a fixed-speed synchronous machine, the machine needs to be rotated when used as a synchronous condenser. With a CFSM configuration, the grid-side converter alone can be operated as a static compensator (STATCOM) to supply reactive power to the grid.

Unlike DFIM, there is no need for a start-up converter or auxiliary turbine machinery for CFSM.

The CFSM technology provides freedom in the design of the synchronous machine. The machine can be designed with higher synchronous reactance than in conventional. This decreases the size of the machine and hence the cost [41, 42]. In addition, the machine can be designed for a unity power factor, and hence the conductor size can be reduced as the reactive power can be supplied by the grid-side converter.

Running the machine at synchronous speed is the best operating point for a full-size converter in CFSM, whereas the same speed is the worst operating point for the rotor-side converter in DFIM as it needs to drive dc current at this speed. This leads to a very high imbalance in losses among the semiconductor devices in an NPC or ANPC converter. Therefore, a dead band is created around synchronous speed in the case of DFIM to avoid continuous dc operation of the rotor-side converter. In the case of Linthal PSHP, it is $\pm$ 0.2 Hz [40]. The maximum loss in the converter occurs at rated speed in the case of DFIM, whereas the same occurs during startup in the case of CFSM, which lasts only for a short time.

The CFSM technology also adds advantages at the system level, e.g., it contributes to the system stability in pumping mode by dynamically varying the load based on a change in the grid frequency.

2.6.2   Disadvantages

The most critical disadvantage of the CFSM technology is that it requires a converter of at least the same size as the rating of the synchronous machine. Considering the virtual inertial contribution, the size would be even larger than the rating of the machine. The cost of the large converters in the range of 100 MVA would be quite high compared to the smaller converter required in the DFIM technology. In addition, such large converters are not yet commercialized for industrial drive applications.

The losses in the full-size converters with the available semiconductor technology may become higher than the gain in efficiency from the reversible pump-turbine by enabling variable speed operation. The wide band-gap devices SiC MOSFETs and SiC IGBTs are now available with voltage ratings as high as 10–15 kV, but with low current ratings [43]. High power converters using these devices have the possibility to achieve efficiency above 99% in the near future [44, 45]. Therefore, the installation of CFSM technology requires to be justified from the benefits gained on the grid integration level. The detailed study in this direction is not part of this research.

2.7   Requirements of the application

The individual unit of the pumped storage power plant installed around the world ranges from a few MW to 400 MW. A full-size converter for large machines in the range of 400 MW would not be beneficial with commercially available semiconductor devices due to high losses in the converter. The cut-off point at the moment is considered 100 MVA [5]; therefore, this size has been decided as the requirement for the sizing of the converters.

Due to the high penetration of renewable energy sources, fixed-pumped storage plants are the most attractive and viable energy storage units to better utilize these sources. However, the existing power plants impose some requirements due to several constraints associated with them. Therefore, the full-size converter is required to fulfill the following features:

- high starting torque in pump mode.
- dynamic variation of load in pump mode to support the grid frequency.
- seamless transition of the mode of operation from the turbine to pump and vice versa.
- boosting the grid performance in generating mode; turbine and machine inertia can be used to temporarily allow further drop in speed on the machine side until the power from the water comes. This feature is implemented in the grid-side converter and is also called virtual inertia or synthetic inertia.
- since the converter will be connected between the stator of the machine and the generator transformer, it should match the output voltage on both ends. In other words, it should provide a transformerless connection to the existing electrical machines.

From the torque speed characteristics of a typical reversible pump turbine as shown in Fig. 2.4, the starting torque, i.e., torque at zero speed, is about 13%. This value
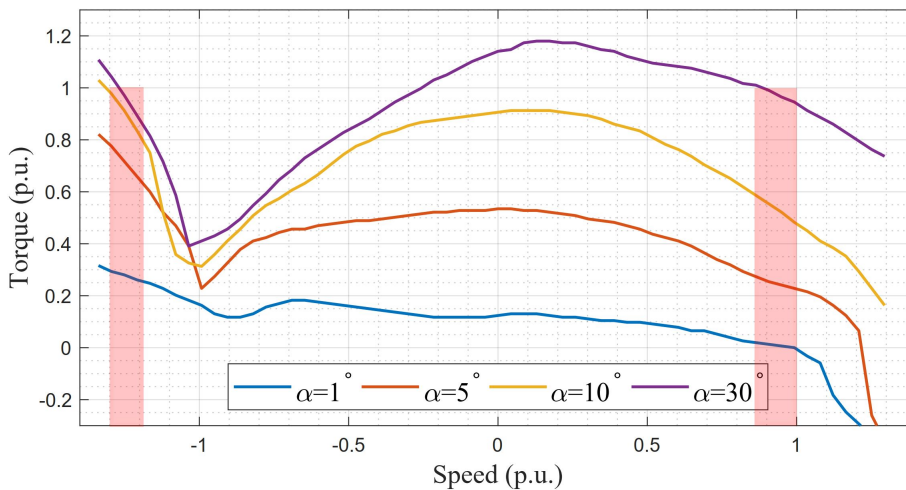
Figure 2.4: Torque speed characteristics of a typical reversible pump turbine at different guide vane openings (α). The speed is positive in generating mode and negative in pumping mode. The shaded region shows the rated operating region. Courtesy: Water Power Laboratory, NTNU, Trondheim.

differs widely in the literature. The higher the torque output from the converter in the low-speed region, the faster the mode transition can be executed.

In the existing pumped storage power plants, the water from the turbine housing is blown away by an air compressor to ease the start-up such that only an additional small-size machine is required to start the machine in pump mode. In this case, starting torque required to drive the pump–turbine system is 3–6% of the torque at rated synchronous speed. For a fast startup, it is required to run the system with water in the casing. In such a situation, the load torque produced at rated speed is between 25–60% of the nominal torque with guide vanes (wicket gate) closed [46]. In [47], the same is mentioned to be around 22% of the nominal torque with the turbine flooded into water. From [48, 49], the torque requirement for a reversible pump-turbine at zero speed can be derived as 50–125% of the nominal torque at a rated speed depending upon the opening of guide vanes.

2.8 Summary

This chapter has presented the state-of-the-art of variable speed operation technology for pumped storage power plants. The DFIM technology is still favorable for very large machine units of several hundreds of MVA because of the feasible size of the converter using commercially available semiconductor devices. The CFSM technology is emerging as a better solution as it enables the more optimal

utilization of pollution-free renewable energy sources. The future wide band-gap SiC devices can make this technology attractive with a more compact and highly efficient converter topology.

Additionally, the prerequisites for implementing CFSM technology, including a torque requirement of approximately 13% of the rated torque when the RPT is submerged in water are outlined.

Chapter 3

Hydraulic System

*In this chapter, an analysis of how a full-size converter-fed synchronous machine can contribute to the grid transients is performed. Since the machine is decoupled from the grid, the speed of the synchronous machine can be allowed to deviate from the synchronous speed during dynamic conditions. The governor parameters are adjusted to study its effect on the oscillation in the waterway and surge tank. The size of the converter depends on the maximum current that the converter carries during dynamic conditions. Hence, how much inertial contribution the converter can provide during dynamics is presented at different loading conditions, which addresses the **Research question 2**. A model of the reversible pump turbine is also presented which is used in the simulation to study the dynamic behavior. The same model is used in the laboratory prototype to emulate the reversible pump-turbine using a converter-controlled induction machine.*

3.1   Introduction

The pumped storage power plants usually consist of either fixed-speed synchronous machines or variable-speed DFIM technology. In both cases, the stator winding of the electrical machines is directly connected to the grid. Therefore, the transients due to disturbances in the grid reflect directly on the machine and hence to the hydraulic turbine and the waterway systems. In addition, the inertia of the machines in both cases is directly coupled to the grid. In the case of a full-size converter-fed synchronous machine, the machine is isolated from the grid with a back-to-back converter inserted between the stator of the machine and the grid. However, the inertia of the machine is still coupled and the disturbances due to the grid reflect the same way on the machine and the water system if there is no additional energy storage system connected to the converter system. As the ma-

chine is not directly linked to the grid frequency, it can, however, run at a different speed than the grid frequency. Even during transient, it has the freedom to let the speed increase/decrease to contribute with the inertial energy stored in the rotor of the machine and the turbine. Yet, how much energy can be delivered to the grid depends on the size of the instantaneous load on the machine and the size of the installed converter.

This chapter presents how the steady state and dynamic operation regime influence the selection of full-size converters for pumped storage plants. A simulation analysis is carried out with step change in load on the grid side and the consequences on the waterway and turbine are analyzed. The waterway and reversible pump turbine are modeled based on their characteristic equations. An equivalent electrical model exhibiting the pump and turbine actions is also presented.

3.2   Modeling of waterway and reversible pump turbine

A simple schematic of a pumped storage plant is shown in Fig. 3.1 with the relevant parameters of each section denoted as length (L), the cross-section of the tunnel (A), and the discharge through the tunnel (Q). The modeling of the reversible pump-turbine and waterway then follows the following mathematical relations based on [50]. The schematic of a typical hydropower plant is presented in Fig. 3.1.

The water flow in the headrace tunnel is mathematically correlated to the other hydraulic parameters as follows:

$$\frac{L_1}{gA_1}\frac{dQ_1}{dt} = H_u - Z_1 - K_1Q_1\,|Q_1| \tag{3.1}$$
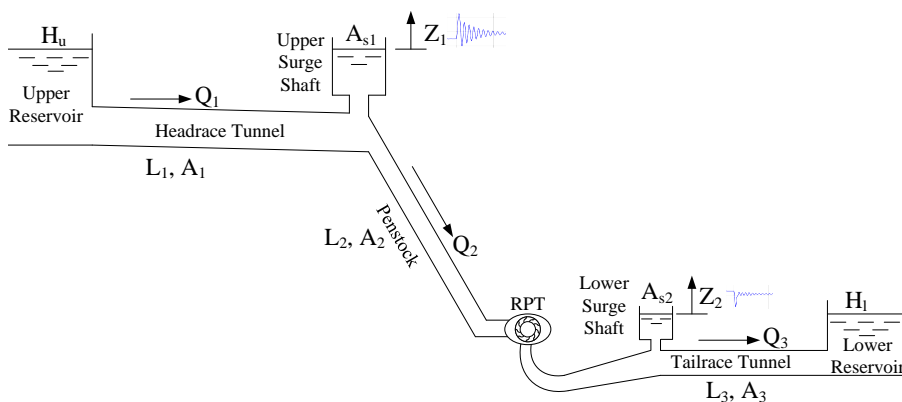
Figure 3.1: Schematic of a typical pumped storage power plant.

where,

$$K_1 = \frac{H_{loss,1}}{Q_R^2} \tag{3.2}$$

K_1 is the head-loss coefficient of the headrace tunnel and $H_{loss,1}$ $[m]$ is the head-loss in the headrace tunnel at a rated flow of Q_R $[m^3/s]$.

Similarly, the water flow through a Francis turbine and penstock can be expressed as:

$$\frac{L_2}{gA_2}\frac{dQ_2}{dt} = Z_1 - Z_2 - K_2 Q_2 |Q_2| - H_{turbine} \tag{3.3}$$

Here, $H_{turbine}$ is the water head utilized for energy conversion and is expressed as:

$$H_{turbine} = H_R \left(\frac{Q_2}{\kappa Q_R}\right)^2 - \frac{1}{g}s\left(\Omega^2 - \Omega_R^2\right) \tag{3.4}$$

where, s is the turbine parameter dependent on its geometry. The dependency on the geometry is expressed as:

$$s = \frac{1}{8}\left(D_1^2 - D_2^2\right) \tag{3.5}$$

where, D_1 and D_2 are the inlet and outlet diameters of the RPT considering the generating mode of operation.

Further, the water flow in the tailrace tunnel is also correlated to the hydraulic parameters in a similar way as for the headrace tunnel. The relation can be expressed as:

$$\frac{L_3}{gA_3}\frac{dQ_3}{dt} = H_l - Z_2 - K_3 Q_3 |Q_3| \tag{3.6}$$

where, K_1, K_2 and K_3 are the frictional coefficients of the headrace tunnel, penstock, and turbine measured in $m/[m^3/s]^2$, respectively.

The dynamics of the water level in the upper surge shaft is expressed as:

$$\frac{dZ_1}{dt} = \frac{1}{A_{s1}}\left(Q_1 - Q_2\right) \tag{3.7}$$

Similarly, the water level in the lower surge shaft is expressed as:

$$\frac{dZ_2}{dt} = \frac{1}{A_{s2}}\left(Q_2 - Q_3\right) \tag{3.8}$$

The dimensionless expressions of the dynamic equations from (3.1) to (3.8) can be obtained using: discharge or water flow, $q = Q/Q_R$; head, $h = H/H_R$; and angular speed, $n = \Omega/\Omega_R$.

$$T_{w1}\frac{dq_1}{dt} = h_u - z_1 - k_1 \left| q_1 \right| q_1 \tag{3.9}$$

where,

$$T_{w1} = \frac{Q_R}{gH_R} \cdot \frac{L_1}{A_1} \tag{3.10}$$

$$T_{w2}\frac{dq_2}{dt} = z_1 - z_2 - k_2 \left| q_2 \right| q_2 - h_{turbine} \tag{3.11}$$

$$T_{w3}\frac{dq_3}{dt} = z_2 - h_l - k_3 \left| q_3 \right| q_3 \tag{3.12}$$

$$\frac{dz_1}{dt} = \frac{Q_R}{H_R A_{s1}} (q_1 - q_2) \tag{3.13}$$

$$\frac{dz_2}{dt} = \frac{Q_R}{H_R A_{s2}} (q_2 - q_3) \tag{3.14}$$

The period of the oscillation of water in the surge shaft ($T_{osc,surgeshaft}$) depends upon the length and cross-section area of the headrace tunnel and its own cross-section area as:

$$T_{osc,surgeshaft} = 2\pi \sqrt{\frac{L_1}{g} \frac{A_{s1}}{A_1}} \tag{3.15}$$

From the equations above, it is noticeable that either (3.3) or (3.11) is the main equation governing the water flow through the turbine.

The opening of the guide vanes (κ) determines the flow of water through the turbine which is described by the valve equation as:

$$\kappa = \frac{Q/\sqrt{2gH}}{Q_R/\sqrt{2gH_R}} \tag{3.16}$$

The same can be expressed as the ratio of the instantaneous inlet guide vane angle (α_1) to the rated inlet guide vane angle (α_{1R}):

$$\kappa = \frac{\sin \alpha_1}{\sin \alpha_{1R}} \tag{3.17}$$

The value of opening of the guide vanes (κ) is equal to 1 at the designed point of operation.

The modified dynamic equations for water flow and the torque output including the pump operation of an RPT, according to [49], are:

$$T_w \frac{dq}{dt} = h - \frac{q\,|q|}{\kappa^2} - \sigma\left(|n\,|n|\,-1|\right) - \sigma n^2 + r_q n\,|q| \tag{3.18}$$

where,

$$T_w = \frac{Q_R}{gH_R}\frac{L}{A} \tag{3.19}$$

$$T_a \frac{d\omega}{dt} = |q|\left(|q|\,m_s - \psi n + \sigma n - r_q\,|q|\right) - r_m n\,|n| - \tau_g \tag{3.20}$$

where, T_a is the mechanical time constant of the rotating mass and r_m is the disk friction coefficient.

The torque equation (3.20) can be rewritten as:

$$T_a \frac{d\omega}{dt} = \tau_{RPT} - \tau_g \tag{3.21}$$

Comparing (3.20) and (3.21), the torque from an RPT can be expressed as:

$$\tau_{RPT} = |q|\left(|q|\,m_s - \psi n + \sigma n - r_q\,|q|\right) - r_m n\,|n| \tag{3.22}$$

where,

$$m_s = \frac{\xi}{\kappa}\left(\cos\alpha_1 + \tan\alpha_{1R}\sin\alpha_1\right) \tag{3.23}$$

The dimensionless parameters ψ, ξ, σ, and r_q are constants depending upon the geometry of a particular turbine and are defined at its best efficiency point (BEP) of operation.

3.3 Steady state operation

Most of the pumped storage plants employ reversible pump turbines (RPT) as a runner. In steady-state operation, they are run either in pump mode or turbine mode. With the full-size converter, it can switch the mode from pump to turbine or vice versa seamlessly as well. The power plants with variable speed arrangements vary the speed of rotation of the RPT to achieve the best efficiency and to regulate the pumping power while running in pump mode.

The Francis turbine and the RPT are characterized for their efficiency at different speeds and discharges as shown in Fig. 3.2. For the variable speed operation of RPT, the Hill chart is followed so it can operate at the maximum possible efficiency for a given water flow.
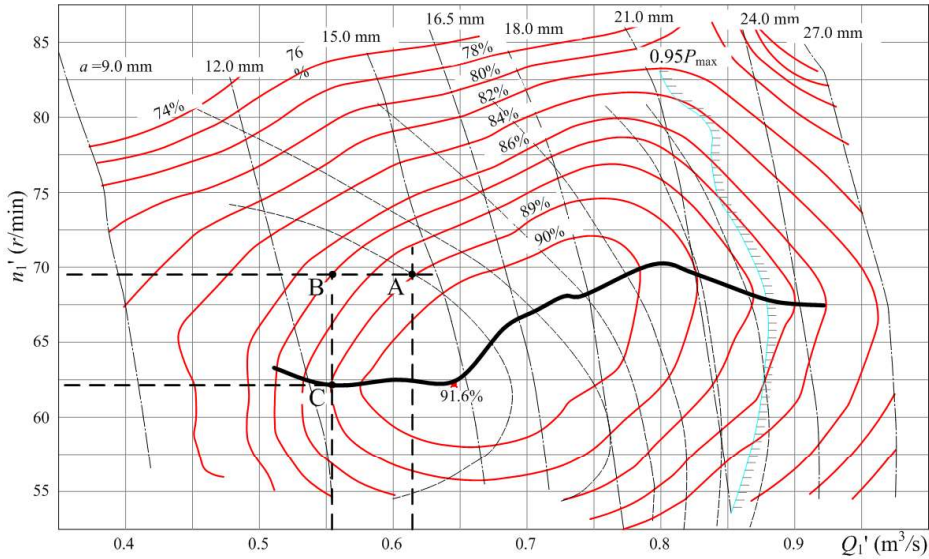
Figure 3.2: Normalized Hill chart for a typical Francis turbine from: [51].

As presented in Fig. 3.2, the turbine running at point "A" has a flow of 0.61 m^3/s and a speed of 69 rpm, and the efficiency of the turbine at this point of operation is 89%. When the water flow is decreased to 0.56 m^3/s to operate at point "B", the efficiency of the turbine falls to 87%. To regain the maximum possible efficiency at this decreased value of water flow, the speed must also be adjusted according to the Hill chart characteristics, which suggest the new operating point "C" where the speed is 64 rpm.

The Hill chart characteristics of an RPT can be listed as a lookup table in the plant operation profile and the speed reference can be generated based on the steady-state water flow and the static head.

3.4   Transient operation

In a full-size converter-fed synchronous machine setup, any transient on the grid side will still reflect on the turbine because there is no energy storage in the system elsewhere. A drop in frequency will give an equivalent power step load on the grid side converter, which will be translated as electrical torque loading on the turbine. The step loading on the turbine will lead to a fall in speed, and consequently, the governor will react by opening the guide vanes and increasing the water flow to maintain the speed to the reference value. Any fast change in the flow to the turbine (q_2) will excite the headrace and tailrace tunnel and will lead to oscillation of water flow, also known as mass oscillation. A previous study shows that the lesser the oscillation in the tunnel, the longer the life span [52]. However, the

oscillation can only be damped by a slow response from the governor to slowly increase the flow through the turbine. Typically, the mechanical time constant of the turbine-generator set (T_m) is designed to be at least six times higher than the water starting time (T_w) such that the inertial energy maintains the speed during transients before the hydraulic energy takes into effect. Slowing the governor is equivalent to slowing the water starting time, i.e., increasing the time to reach the water to the turbine. This will again lead to a sharp decline in speed, and the system will not be able to recover the speed.

To gain any significant advantage to damp the oscillation in the tunnels, the ramping of the water flow through the turbine should be in the range of the oscillation time constant of the water in the surge tank given by (3.15), which is normally in the range of minutes.

3.4.1   Long transient on grid side

In a grid-connected system, any change in grid frequency can be regarded as a step power load on the synchronous machine directly connected to the grid. In a back-to-back converter-fed synchronous machine, the power step will be applied on the grid-side converter. The effect ultimately translates to a power step on the machine as there is no energy storage on the dc-link.

The response of the turbine governor with different control parameters is presented in Fig. 3.3. The gain of the PI controller has been set in such a way that the response is less oscillatory and is stable for sustained power step load on the grid side. The results show that the longer the integrator time constant, i.e., the lower the integral gain (K_p/T_i), the slower the recovery of the speed.

The water flow in the headrace tunnel (q_1) is as shown in Fig. 3.4 for the same set of governor parameters used to attain the speed response of Fig. 3.3. The results indicate that there is no significant difference in the behavior of water flow in the tunnel caused by changing the governor parameters.

3.4.2   Short transient on grid side

Normally in a large system, the fall in frequency due to disturbance is temporary. The period ranges from a few milliseconds to ten seconds. The nature of the disturbance can be approximated as:

i) Arrest period - steady decrease in frequency when all the connected power sources participate to arrest this decrement using the inertial energy of the rotor.

ii) Rebound period - the governor activates and the frequency stabilizes at a new point based on droop.
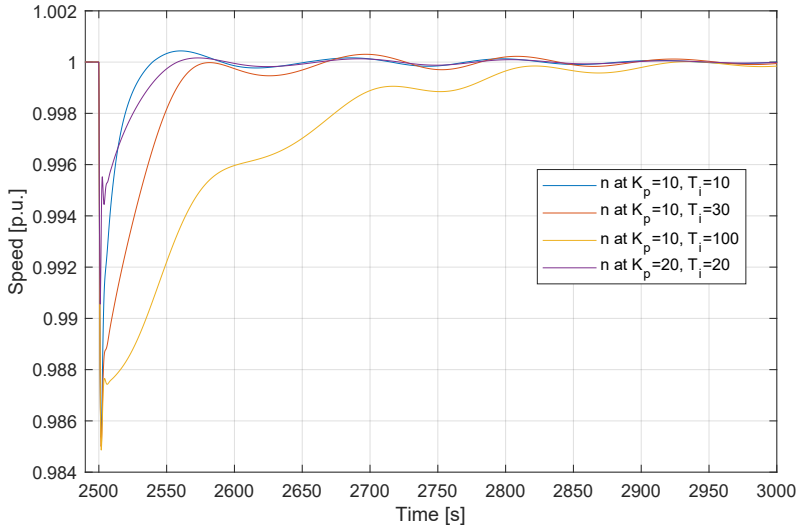
Figure 3.3: Response of turbine speed with various controller parameters of Governor when a step load is applied on the grid side.
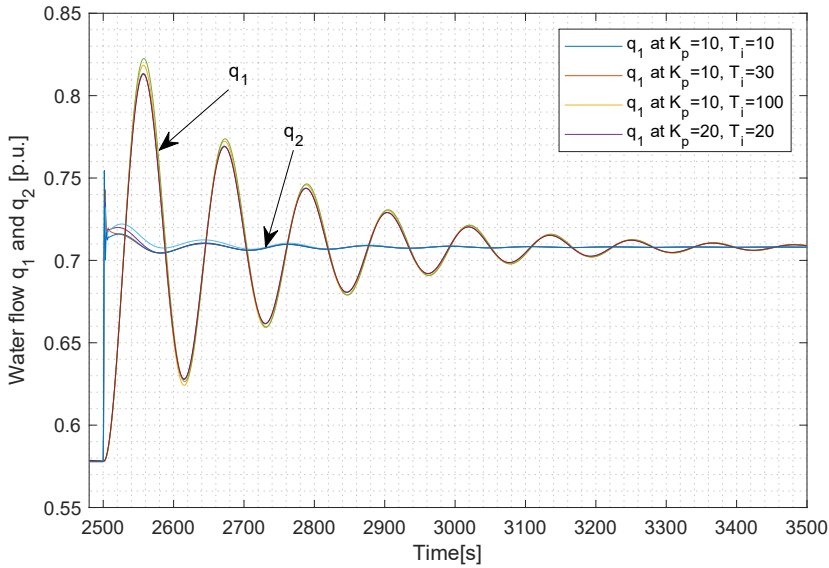
Figure 3.4: Water flow through headrace tunnel (q_1) and through turbine (q_2) at different values of Governor controller. The parameters of the governor or the speed response do not significantly affect the flow q_1. The time constant of the oscillation is very high (in the range of minutes) compared to the difference in the speed of the turbine due to changes in governor parameters.

iii) Recovery period - the secondary controller or the TSO initiates a steady increase in frequency when all the connected power sources again participate to catch the nominal frequency.

The steady increase or decrease in frequency yields a constant df/dt which is equivalent to a power step on the grid side converter in this case. The duration of the power step can be assumed for 10 seconds considering the worst-case scenario. Figure 3.5 and 3.6 show the behavior of the turbine system with different gain and time constants of the governor PI controller. Evidently, the lower gain in the governor utilizes the shaft inertia to the maximum and allows a significant fall in speed, which would have been unacceptable in a grid-connected system. The lower speed for a constant power step translates to higher torque output from the machine which at constant flux, in the machine would lead to higher stator current and hence higher current into the machine-side converter. In this case, the converter needs to be rated for the highest allowable current. For example, to allow a fall of 20% in speed during transient, the machine-side converter must be rated for 125% of the nominal current rating of the synchronous machine.

A comparison between various control parameters of the governor is carried out
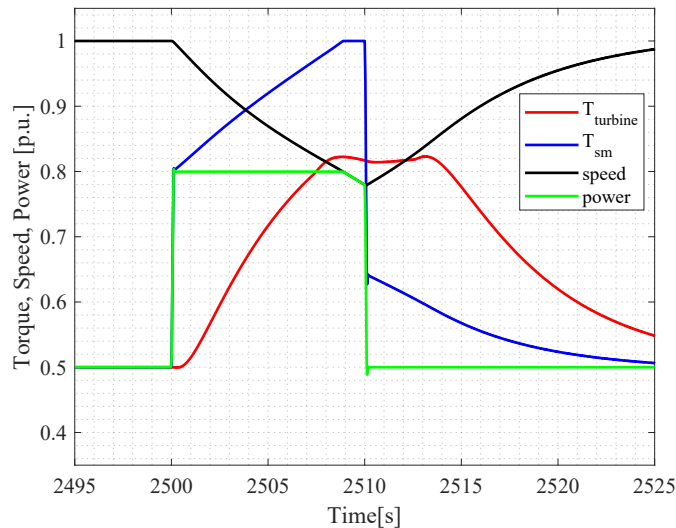
Figure 3.5: Step load with constant power on grid side for 10 seconds. Torque and speed with governor $K_p = 2$ and $T_i = 100s$. Due to the lower gain of the governor PI controller, the rate of torque produced from the turbine is slower. This leads to a steady fall in speed and a rise in electrical torque loading on the machine to balance the power step. At $t = 2509s$, the electrical torque is limited to 1 pu, and the power contribution from the machine decreases. A prolonged power step would lead to a further decrease in speed which could not be restored because the output torque of the turbine decreases at a lower speed.
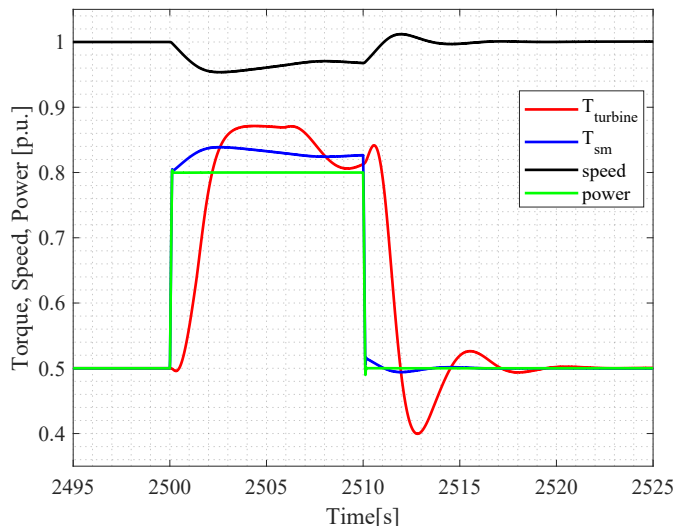
Figure 3.6: Step load with constant power on grid side for 10 seconds. Torque and speed with governor $K_p = 10$ and $T_i = 100s$. The higher gain of the governor PI makes the turbine produce torque at a faster rate and balance the electrical load torque. This leads to faster stabilization of speed.

to study the impact of these parameters on the oscillation of the water flow in the headrace tunnel. The results in Figure 3.7 show that this does not provide any significant advantage to mitigate the pressure oscillation in the tunnel. This is because the mechanical time constant of the turbine-generator shaft is very low (around 10 seconds) compared to the oscillation period of the pressure in the tunnels (in the range of minutes).

3.5   Dimensioning of machine-side converter

The continuous current rating of the machine side converter depends upon how much inertial energy of the rotating mass of the machine will be utilized during transients. For example, if the lower speed limit during transient is 80% of the nominal speed, the torque required to deliver a constant power step would be 125% of the nominal torque. As the stator flux is controlled by the exciter converter, a constant flux of 1 p.u. can be maintained all the time, hence the current injected into the machine side converter will be 125%. It can also be observed that the faster the governor, the lower the current rating.

Although this analysis gives the peak current rating of the converter, the nominal rating can only be decided by detail loss analysis in different operating conditions. The operation at and around zero speed is crucial for deciding the converter rating.
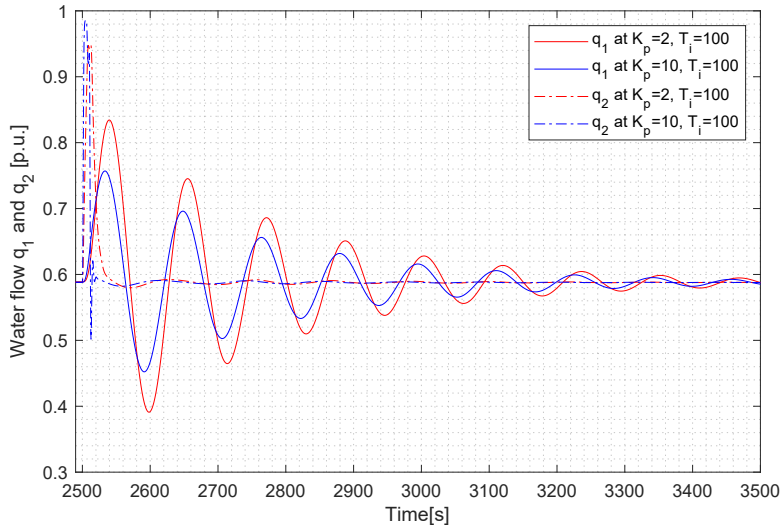
Figure 3.7: Step load with constant power on grid side for 10 seconds. The discharge through the headrace tunnel (q_1) and the turbine (q_2) at different values of the Governor controller are presented. The parameters of the governor or the speed response do not affect the flow q_1 significantly. The time constant of the oscillation is very high (in the range of minutes) compared to the difference in the speed of the turbine due to changes in governor parameters.

3.6 Conclusion

The analysis shows that since there is no energy storage in the dc-link of the back-to-back converter system, any transient on the grid side will directly be transferred to the machine/turbine.

Slowing down the governor can help only at part load as there is a margin in the current rating of the converter, i.e., higher virtual inertia contribution when the machine is running at a low load and very low virtual inertia contribution if the machine is already running at full load.

Slowing down the governor does not help the oscillation in the tunnel and surge shaft significantly because the time constants of the surge shaft oscillation are very high (in the range of minutes) compared to the governor's response. If the governor response is made slow in that range, the speed of the turbine will fall sharply due to the load step and collapse if the load step is for a longer duration.

Oscillation in the tunnel or surge shaft remains at low load rather than at full load for a relatively long period because the damping is flow dependent, i.e., the higher the flow, the higher the damping, and vice versa. Therefore, when the turbine is suddenly stopped, the oscillation remains for a very long period because there is

almost no damping when the amplitude of the oscillation is low.

Both the virtual inertia and lower oscillation cannot be achieved with a slow governor. The slow governor can only help if the power step on the grid side is for a short duration of about 10 seconds. However, the speed will collapse if the step remains for a minute or longer as presented in this chapter with a model turbine.

Chapter 4

Modeling and Control of Synchronous Machine

Fixed speed pumped storage power plants normally operate with wound rotor synchronous machines. Therefore, this chapter discusses the mathematical modeling of the synchronous machine and its control for the case when the same machine will be connected to the grid via a full-size converter. The innermost control loops of the converters include the stator current control and exciter current control. Hence, stator current and exciter current equations are derived with independent state variables such that the standard Modulus Optimum tuning method can be employed to tune these current controllers. A control method for a dc-dc converter for excitation current control is also presented. The tuning of these controllers is essential for the stable functioning of the secondary controller, which is presented in Chapter 7.

4.1 Introduction

In a pumped storage power plant with a full-size back-to-back converter, the machine-side converter will be controlled differently in the pump and turbine mode of operation. In turbine mode, the source of power is the turbine, and therefore, the machine-side converter will control the dc-link voltage. The grid-side converter will control the ac voltage and frequency to connect to the grid. In pump mode, the source of power is the grid, and therefore, the grid side converter will control the dc-link voltage, and the machine side converter will control the flux and the torque output of the machine. In both cases, the output of the dc-link voltage controller or the torque controller will be to produce the current references to achieve the set point values. Hence, the current controllers become the primary control

unit of the machine-side converter in any mode of operation. The inner current controllers must be stable and tuned appropriately for the proper functioning of the outer controllers like speed controller and dc-link voltage controller.

In this chapter, the synchronous machine is modeled with d-and q- axes stator currents as state variables. Hence, Modulus Optimum can be used to tune these controllers. A similar approach is adopted for designing the controller for the excitation current controller.

4.2   Synchronous machine model

A wound rotor synchronous machine consists of three armature windings on the stator, and excitation winding and damper windings on the rotor, as depicted in Fig. 4.1. The damper winding is usually solid bars placed uniformly around the rotor circumference and short-circuited at both ends. Assuming the excitation winding is placed along the d-axis, there are damper windings along both d- and q-axes. The equations for the voltage induced in these windings can be expressed as in (4.1) – (4.3):
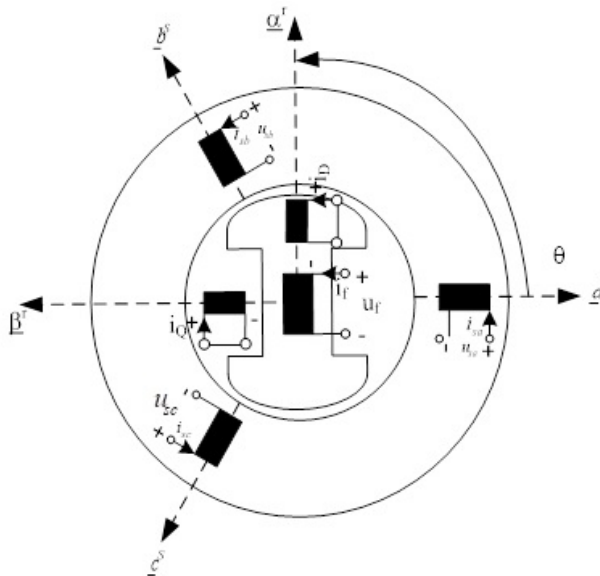
Figure 4.1: Typical layout of 3-phase wound rotor synchronous machine.

$$U_{sa} = R_s I_{sa} + \frac{d\Psi_{sa}}{dt}$$

$$U_{sb} = R_s I_{sb} + \frac{d\Psi_{sb}}{dt} \tag{4.1}$$

$$U_{sc} = R_s I_{sc} + \frac{d\Psi_{sc}}{dt}$$

$$U_f = R_f I_f + \frac{d\Psi_f}{dt} \tag{4.2}$$

$$U_D = R_D I_D + \frac{d\Psi_D}{dt}$$

$$U_Q = R_Q I_Q + \frac{d\Psi_Q}{dt} \tag{4.3}$$

where U_{sa}, U_{sb} and U_{sc} are the voltages of phases a, b, and c of stator winding. U_f is the voltage across excitation winding, and U_D and U_Q are voltages across the damper windings along the d- and q- axes, respectively. The voltages U_D and U_Q are equated to zero because the damper winding in the machine is short-circuited at both ends.

The equations (4.1) – (4.3) can be per unitized using the peak voltage of the respective windings. These equations can be rearranged in a synchronously rotating reference frame, i.e., d-q coordinates, and can be expressed as:

$$u_d = r_s i_d + \frac{1}{\omega_n}\frac{d\psi_d}{dt} - n\psi_q \tag{4.4}$$

$$u_q = r_s i_q + \frac{1}{\omega_n}\frac{d\psi_q}{dt} + n\psi_d \tag{4.5}$$

$$u_f = r_f i_f + \frac{1}{\omega_n}\frac{d\psi_f}{dt} \tag{4.6}$$

$$0 = r_D i_D + \frac{1}{\omega_n}\frac{d\psi_D}{dt} \tag{4.7}$$

$$0 = r_Q i_Q + \frac{1}{\omega_n}\frac{d\psi_Q}{dt} \tag{4.8}$$

The flux linkages in the above equations can further be expressed in terms of the flux linkages produced by the windings themselves and the other windings along

the same axis as follows:

$$\psi_d = x_d i_d + x_{md}(i_D + i_f) \tag{4.9}$$
$$\psi_q = x_q i_q + x_{mq} i_Q \tag{4.10}$$
$$\psi_f = x_f i_f + x_{md}(i_d + i_D) \tag{4.11}$$
$$\psi_D = x_D i_D + x_{md}(i_d + i_f) \tag{4.12}$$
$$\psi_Q = x_Q i_Q + x_{mq} i_q \tag{4.13}$$

The relation between self-inductances and mutual inductances can be expressed by defining leakage factors (σ) as follows:

$$x_d = x_{md}(1 + \sigma_d) \tag{4.14}$$
$$x_q = x_{mq}(1 + \sigma_q) \tag{4.15}$$
$$x_f = x_{md}(1 + \sigma_f) \tag{4.16}$$
$$x_D = x_{md}(1 + \sigma_D) \tag{4.17}$$
$$x_Q = x_{mq}(1 + \sigma_Q) \tag{4.18}$$

The combination of equations from (4.4) to (4.18) can be rearranged such that the equation can be presented with currents as state variables. The detailed derivation is presented in Appendix A. The voltage equations can be rearranged as follows:

$$u_d = r'_d i_d + \frac{\sigma_{dD} x_d}{\omega_n} \frac{di_d}{dt} + \frac{r_D}{(1 + \sigma_D)^2}(i_f + \sigma_D T_D \frac{di_f}{dt}) - \frac{\psi_D}{\omega_n T_D(1 + \sigma_D)} - n\psi_q \tag{4.19}$$

$$u_q = r'_q i_q + \frac{\sigma_{qQ} x_q}{\omega_n} \frac{di_q}{dt} - \frac{\psi_Q}{(1 + \sigma_Q)\omega_n T_Q} + n\psi_d \tag{4.20}$$

$$u_f = r'_f i_f + \frac{\sigma_{fD} x_f}{\omega_n} \frac{di_f}{dt} + \frac{r_D}{(1 + \sigma_D)^2}(i_d + \sigma_D T_D \frac{di_d}{dt}) - \frac{\psi_D}{\omega_n T_D(1 + \sigma_D)} \tag{4.21}$$

A further rearrangement of the equations simplifies the voltage equations as follows [53]:

$$u_d = r_d'' i_d + \frac{x_d''}{\omega_n}\frac{di_d}{dt} - \frac{r_{Rd}'}{x_{Md}}\psi_{Rd} + r_{Rd}' i_f + k_{fD}\left(u_f - r_f i_f\right) - n\psi_q \quad (4.22)$$

$$u_q = r_q'' i_q + \frac{x_q''}{\omega_n}\frac{di_q}{dt} - \frac{r_{Rq}}{x_{Mq}}\psi_{Rq} + n\psi_d \quad (4.23)$$

$$u_f = r_f'' i_f + \frac{x_f''}{\omega_n}\frac{di_f}{dt} - \frac{r_{Rd}''}{x_{Md}}\psi_{Rd} + r_{Rd}'' i_d + k_{dD}\left(u_d - r_s i_d + n\psi_q\right) \quad (4.24)$$

$$T_D\frac{d\psi_{Rd}}{dt} = -\psi_{Rd} + x_{Md}\left(i_d + i_f\right) \quad (4.25)$$

$$T_Q\frac{d\psi_{Rq}}{dt} = -\psi_{Rq} + x_{Mq}i_q \quad (4.26)$$

The simplified voltage equations from (4.22) to (4.26) are first order differential equations with i_d, i_q, i_f, ψ_{Rd}, and ψ_{Rq} as state variables. The constituent parameters of the equations are defined in Appendix A.

4.3   Torque control

The synchronous machine will run in dc-link control mode and speed control mode while the RPT will run in turbine mode and pump mode, respectively. In either mode, the output of these controllers is the torque reference. Therefore, the response of the torque controller must be as fast as possible. The torque reference is converted to d- and q- axes current and field current references using control strategies. These current references are executed by the respective current controllers. Here, two main control strategies–unity power factor control and maximum torque per ampere control–are described, which will be used in this application.

4.3.1   Unity power factor control

The unity power factor control yields the given torque with the minimum possible current through the stator winding of the machine. Hence, it gives rise to the least loss in the machine, which in turn leads to the smallest machine for the same power. The unity power factor control ($\cos\varphi = 1$) is presented in [54]. A detailed explanation is provided in Appendix C.1. The control principle is depicted in Fig. 4.2. The basic principle is to align the current vector perpendicular to the stator flux, i.e., in phase with the stator voltage. The position of the stator flux vector is determined based on the torque reference. Plus, the de-magnetizing effect of the d-axis current in either mode of operation is compensated by the excitation current such that the stator flux is constant.
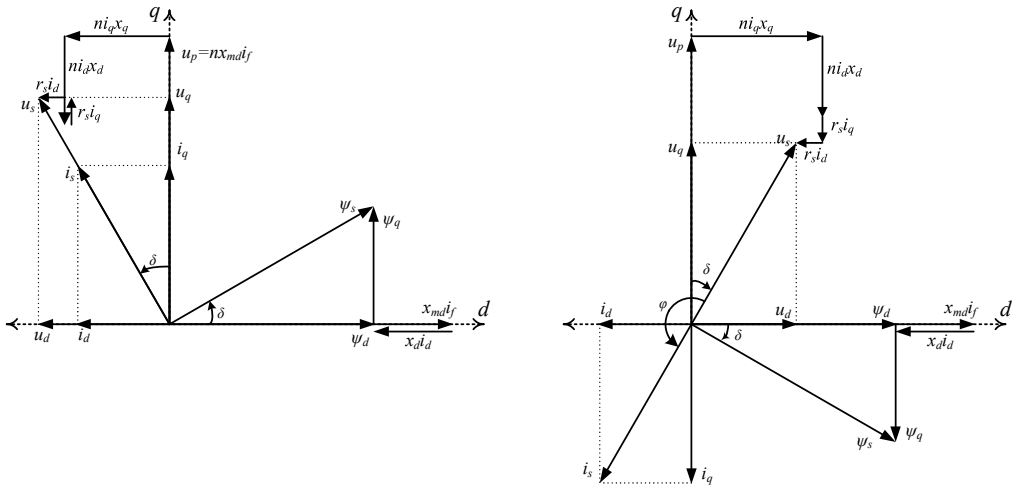
Figure 4.2: Phasor diagram of unity power factor control of a synchronous machine. Left: motor operation (pump mode); right: generator operation (turbine mode).

4.3.2   Maximum torque per ampere control

The synchronous reactance along the d-axis is larger than that along the q-axis in salient pole synchronous machines, i.e., $x_d > x_q$. Therefore, the stator current vector can be controlled such that the reluctance torque due to saliency can be utilized optimally.

The derivation of the expressions (see Appendix C) to determine the position of the current vector w.r.t. q-axis shows that this strategy is the same as the $\cos \varphi = 1$ control strategy. This is possible because the excitation current can also be independently controlled to maintain 1 pu of flux in the stator. The excitation current reference ($i_{f,ref}$) to achieve this is as:

$$i_{f,ref} = \frac{\psi_{s,ref}^2 + x_d x_q i_{s,ref}^2}{x_{md}\sqrt{\psi_{s,ref}^2 + x_q^2 i_{s,ref}^2}} \tag{4.27}$$

Hence, the wound rotor synchronous machine is a special type of ac machine that can achieve both unity power factor and maximum torque per ampere (MTPA) at the same time when the stator is also supplied by a variable speed drive. The unity power factor leads to a smaller converter, whereas the MTPA control strategy yields a smaller machine. When the synchronous machine is connected to the grid via a back-to-back converter, the grid-side converter can supply the reactive power to the grid as per the grid code, and the machine can be designed for a unity power factor.

4.4 Stator current control

The innermost control loop of the synchronous machine control is the stator current controllers. The three-phase ac currents are transformed into a synchronously rotating d-q frame of reference such that these quantities become dc in a steady state and a conventional PI controller can be used.

A schematic of the control of the d-axis current is shown in Fig. 4.3. The time delay in the inverter (T_{delay}), the filter time constant (T_f), and the time delay in the processor can be lumped into a time constant of a first-order filter with a time constant, T_{sum}. The dc-link voltage (u_{dc}) is controlled by the other converter on the same dc-link and can be assumed to be equal to 1 pu while designing the current controllers. The output of the controller is divided by the dc-link voltage (u_{dc}) so that the effective gain of the PI controller is adaptive. The open loop transfer function for the d- and q-axis current controllers can then be expressed as:

$$h_{o,id} = K_{p,d} \frac{1 + T_{i,d}s}{T_{i,d}s} \frac{1}{(1 + T_{sum}s)} \frac{u_{dc}}{r_d'' \left(1 + T_d'' s\right)}$$
$$h_{o,iq} = K_{p,q} \frac{1 + T_{i,q}s}{T_{i,q}s} \frac{1}{(1 + T_{sum}s)} \frac{u_{dc}}{r_q'' \left(1 + T_q'' s\right)}$$

$$(4.28)$$

where,

$$T_d'' = \frac{x_d''}{\omega_n r_d''}$$

$$T_q'' = \frac{x_q''}{\omega_n r_q''}$$

$$T_{sum} = T_{delay} + T_{fd}$$

$$T_{fd} = T_{fq}$$

$$(4.29)$$
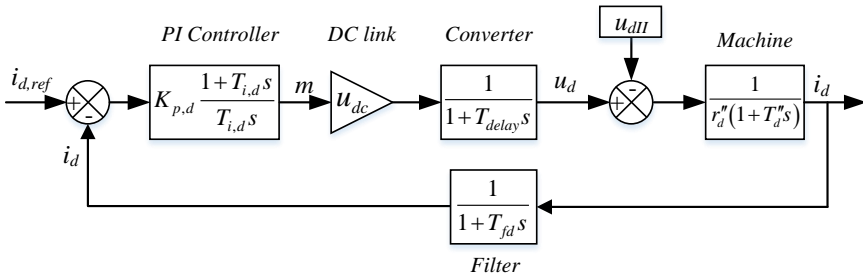
Figure 4.3: Control schematic of d-axis current controller.

and,

$$u_{dII} = -\frac{r'_{Rd}}{x_{Md}}\psi_{Rd} + r'_{Rd}i_f + k_{fD}\left(u_f - r_f i_f\right) - n\psi_q$$
$$u_{qII} = -\frac{r_{Rq}}{x_{Mq}}\psi_{Rq} + n\psi_d \tag{4.30}$$

The flux linkages in the decoupling terms of (4.30) are estimated using a voltage or current model. These terms can be considered disturbances in the output voltage while designing the controllers for d- and q-axis currents. For a digital controller with asymmetrical modulation, the sampling time is half of the time period of the triangular PWM career wave, i.e., ($T_{samp} = T_{tri}/2$ and $T_{tri} = 1/f_{sw}$). Comparing the open loop transfer function of (4.28) with the standard transfer function where Modulus Optimum (Appendix A) can be used, the gain and time constant for the PI controllers can be obtained as:

$$K_{p,d} = \frac{T''_d - \frac{T_{samp}}{2}}{2 \cdot \frac{1}{r''_d} \cdot \left(T_{sum} + \frac{T_{samp}}{2}\right)} \approx \frac{x''_d}{2 \cdot \omega_n \cdot \left(\frac{5}{4} \cdot T_{tri}\right)} = \frac{x''_d}{5 \cdot \omega_n \cdot T_{samp}}$$

$$T_{i,d} = \frac{x''_d}{\omega_n \cdot r''_d} \tag{4.31}$$

$$K_{p,q} = \frac{x''_q}{\frac{5}{2} \cdot \omega_n \cdot T_{tri}} = \frac{x''_q}{5 \cdot \omega_n \cdot T_{samp}}$$

$$T_{i,q} = \frac{x''_q}{\omega_n \cdot r''_q}$$

4.4.1 Tuning of stator current controllers

The stator current controller of the synchronous machine presented in Appendix F was tuned in the laboratory arrangement established for this research. The controller parameters were adjusted around the theoretical value until the step response was determined to be satisfactory. The response of the d- and q- axes current controllers obtained are as presented in Fig. 4.4 and 4.5. Evidently, the current controllers achieve the step change in the reference within four sampling intervals.

The practically tuned values of the controller parameters and the same based on (4.31) are presented in Table 4.1. The control parameters with the Modulus Optimum method give an overshoot of 4.7%, but here it is tuned to achieve a faster response to the step change in the current controller. Therefore, the proportional gain is higher and the integral time constant is lower than the theoretically calcu-
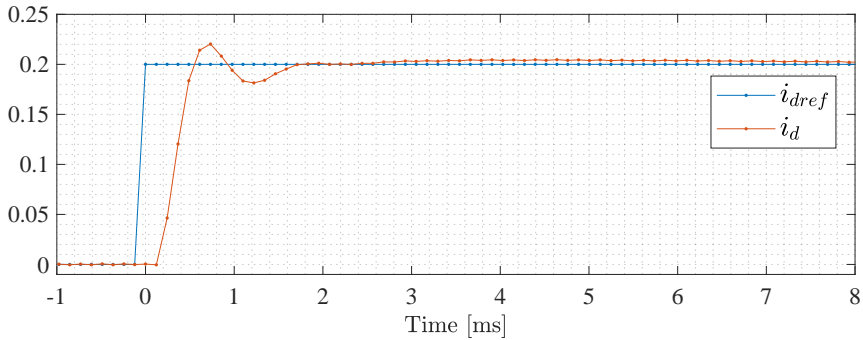
Figure 4.4: Step response of d-axis current controller of the 100 kVA synchronous machine.
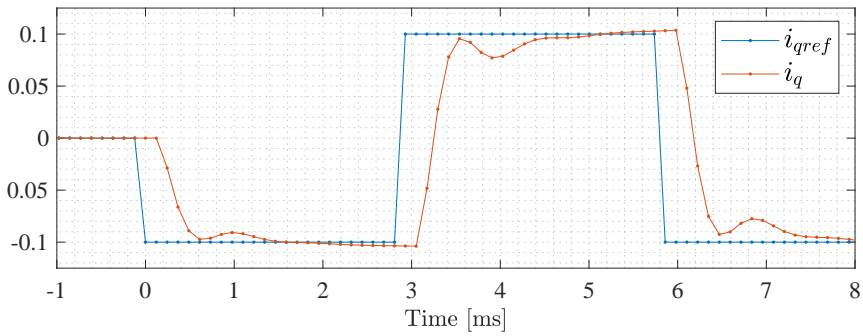
Figure 4.5: Step response of q-axis current controller of the 100 kVA synchronous machine. Only two quick pulses have been applied along the q-axis while tuning such that the rotor will not move to a new position.

Table 4.1: Theoretically calculated and experimentally tuned values of current controllers for the synchronous machine.

Parameters	Theoretical	Experimental
$K_{p,d}$	1.71	1.75
$T_{i,d}$	4.6 ms	3.125 ms
$K_{p,q}$	1.617	2.2
$T_{i,q}$	4.27 ms	1.56 ms

The parameters used in (4.31) are $x_d^{''} = 0.336 \ pu$, $x_q^{''} = 0.317 \ pu$, and $T_{samp} = 0.125 \ ms$ (see Appendix F).

lated values. The tuned values produce the step change in reference current within four sampling periods.

4.5   Excitation current control

Similar to the stator current controller, the excitation current controller can also be designed using a decoupling term and Modulus Optimum based on the voltage equation in (4.24). The time delay in the inverter, the filter time constant, and the time delay in the processor are lumped into a time constant of a first-order filter as T_{sum}. Since the control loop of the excitation current controller is similar to the one for the stator current controller as presented in Fig. 4.3, the open loop transfer function would also be similar, expressed as:

$$h_{o,if} = K_{p,f} \frac{1 + T_{i,f}s}{T_{i,f}s} \frac{1}{(1 + T_{sum}s)} \frac{u_{dc,f}}{r_f'' \left(1 + T_f'' s\right)} \tag{4.32}$$

where,

$$T_f'' = \frac{x_f''}{\omega_n r_f''} \tag{4.33}$$

$$T_{sum} = T_{delay} + T_{f,f}$$

The decoupling term from (4.24) is chosen as:

$$u_{fII} = -\frac{r_{Rd}''}{x_{Md}} \psi_{Rd} + r_{Rd}'' i_d + k_{dD} \left(u_d - r_s i_d + n\psi_q\right) \tag{4.34}$$

Using Modulus Optimum, the gain and time constant of the PI controller are obtained as:

$$K_{p,f} = \frac{\frac{x_f''}{\omega_n r_f''} - \frac{T_{samp}}{2}}{2 \frac{1}{r_f''} \left(T_{sum} + \frac{T_{samp}}{2}\right)} \approx \frac{x_f''}{2\omega_n \left(\frac{5}{4}T_{tri}\right)} = \frac{x_f''}{5\omega_n T_{samp}} \tag{4.35}$$

$$T_{i,f} = T_f'' = \frac{x_f''}{\omega_n r_f''}$$

The dc-link voltage of the excitation converter can dynamically vary. Therefore, the output of the PI controller is divided by $u_{dc,f}$, which effectively makes the controller adaptive to the variation. The excitation converter in the laboratory arrangement was not in the scope of this research, and therefore, the practical response

could not be verified. The main controller for the synchronous machine calculates the excitation current reference to achieve a unity power factor and is sent to the excitation current controller over the CAN bus communication network.

4.6   Stator flux amplitude control

The torque output from a synchronous machine can be expressed in terms of stator flux (ψ_s) and stator current (i_s) as:

$$\tau_e = \pm \psi_s i_s \tag{4.36}$$

The stator flux is controlled such that the synchronous machine always runs at unity power factor in the steady state. The excitation current required to achieve this is as given by:

$$i_{f,ref} = \frac{\psi_{s,ref}^2 + x_d x_q i_{s,ref}^2}{x_{md}\sqrt{\psi_{s,ref}^2 + x_q^2 i_{s,ref}^2}} \tag{4.37}$$

However, the mathematical calculation of excitation current to achieve the set point for stator flux is an open loop control because the actual stator flux is not considered. To improve the control of the stator flux amplitude, a closed-loop control can be implemented. The calculated excitation current reference given by (4.37) can be used as a feed-forward term in the controller as presented in Fig. 4.6. The actual flux in the machine can be estimated using the classical voltage model combined with a current model for low-speed operation. Since sensorless control is not the main focus of this research, it can be assumed that the flux can be measured. The approach is to use i_f for controlling the stator flux amplitude. This current, however, is mainly controlling the d-component of the stator flux only. This design of the controller is based on (4.38):

Figure 4.6: Control schematic of stator flux and exciter current controller.

$$\psi_d = \psi_{Rd} + \sigma_{dD} \cdot x_d \cdot i_d + \sigma_D \cdot x_{Md} \cdot i_f$$

$$T_D \frac{d\psi_{Rd}}{dt} = -\psi_{Rd} + x_{Md} (i_d + i_f)$$

(4.38)

The response of the closed-loop field current control can be modeled as a first-order transfer function with the time constant $T_{eq,f}$. The open-loop transfer function can then be expressed as:

$$h_{o,\psi} = K_{p,\psi} \frac{1 + T_{i,\psi}s}{T_{i,\psi}s} \frac{1}{(1 + T_{sum}s)} \frac{x_{Md}}{(1 + T_D s)}$$

$$T_{sum} = T_{eq,f} + T_{f,f} = 2T_{sum,f} + T_{f,f}$$

(4.39)

Since the open-loop transfer function has two poles, a similar approach as in the case of stator current control and excitation current control can be used. Hence, using the Modulus Optimum, the gain and the time constant of the PI controller are obtained as:

$$K_{p,\psi} = \frac{\frac{x_{Md}}{\omega_n \cdot r_{Rd}} - \frac{T_{samp}}{2}}{2 \cdot x_{Md} \cdot \left(T_{sum} + \frac{T_{samp}}{2} \right)} \approx \frac{1}{2 \cdot r_{Rd} \cdot \omega_n \cdot \left(T_{sum} + \frac{T_{tri}}{4} \right)}$$

$$T_{i,\psi} = T_D = \frac{x_{Md}}{\omega_n \cdot r_{Rd}}$$

(4.40)

4.7   Speed control

The machine-side converter runs in speed control in pump mode and adjusts the speed to control the flow of water according to the power available from the grid. The adjustment of speed also enables the RPT to run at optimal efficiency based on instantaneous flow and the water head. The output of the speed controller is the torque reference to the inner controller loop. The torque reference is translated into current references based on the unity power factor control strategy as shown in Fig. 4.7. The current controllers act as described in Section 4.4. While designing the speed controller, the inner closed loop current controller can be approximated as a low pass filter with a time constant, $T_{eq,i}$ as presented in Fig. 4.8.

The open-loop transfer function of the speed control loop with a PI controller can be expressed as in (4.41):

$$h_{o,n} (s) = K_{p,n} \frac{1 + T_{i,n}s}{T_{i,n}s} \frac{\tau_{e,ref}}{(1 + T_{eq,i}s)(1 + T_{f,n}s)} \frac{1}{T_m s}$$

(4.41)

Figure 4.7: Schematic of the speed controller with inner current control loop (only d-axis current control loop is shown for simplicity).

Figure 4.8: Schematic of the speed controller with the inner current control loop lumped as a low pass filter.

$$h_{o,n}\left(s\right) = K_{p,n}\frac{1+T_{i,n}s}{T_{i,n}s}\frac{\tau_{e,ref}}{\left(1+T_{sum,n}s\right)}\frac{1}{T_m s} \tag{4.42}$$

$$
\begin{aligned}
T_{sum,n} &= T_{eq,i} + T_{f,n} \\
T_{eq,i} &= 2\left(T_{delay} + T_{f,id}\right)
\end{aligned}
\tag{4.43}
$$

Since the open-loop transfer function in (4.42) consists of two poles at the origin, Symmetrical Optimum is used for determining the controller parameters as explained in Appendix B. Hence, using the Symmetrical Optimum, the gain and time constant of the speed controller are obtained as:

$$
\begin{aligned}
K_{p,n} &= \frac{T_m}{\sqrt{\beta}T_{sum,n}} \\
T_{i,n} &= \beta T_{sum,n} \\
\omega_{c,n} &= \frac{1}{\sqrt{\beta}T_{sum,n}}
\end{aligned}
\tag{4.44}
$$

The value of β is selected such that it achieves enough phase margin. A value of $\beta = 4$ gives rise to a high overshoot to step change in speed reference. But, the speed of the machine never needs to be increased or decreased in step. Therefore, the overshoot can be eliminated by introducing a low pass filter with a time con-

stant of $T_{sum,n}$ to the speed reference. The most important aspect of the design of the controller is that the speed does not fall sharply due to a step load.

4.7.1   Tuning of speed controller

The speed controller of the synchronous machine was tuned with the available laboratory setup and the obtained response is as presented in Fig. 4.9. The mechanical time constant (T_m) of the rotating mass of the synchronous machine and the induction machine set is 1 second.

The practically tuned values of the controller parameters and the same based on (4.44) are presented in Table 4.2. The practically tuned values differ significantly from the theoretical values. This is because the symmetrical optimum used to tune the speed controller gives a very fast response with approximately 40% of overshoot with $\beta = 4$. However, in this application, the speed controller is used in pump mode and such a rapid acceleration or deceleration in speed is not required. Therefore, a higher value of β is chosen while applying symmetrical optimum to tune the speed controller, which gives a higher phase margin and a relatively smaller gain and higher time constant. The proportional gain of the practically tuned values from the laboratory arrangement is chosen to be lower than the theoretical value to maintain the overshoot of the step response within 10%.
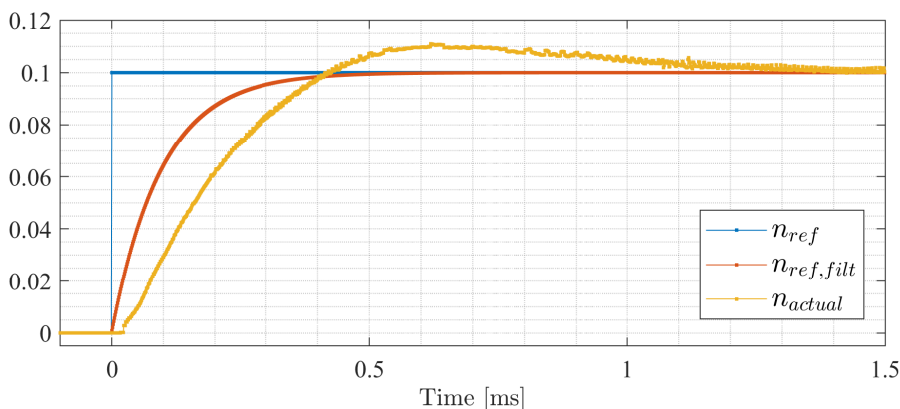
Figure 4.9: Step response of speed controller of the 100 kVA synchronous machine. The reference is filtered by a first-order low pass filter with a time constant of 100ms.

Table 4.2: Theoretically calculated and experimentally tuned values of speed controller of the synchronous machine.

Parameters	Theoretical ($\beta = 4$)	Theoretical ($\beta = 120$)	Experimental
$K_{p,n}$	149.9	27.4	20
$T_{i,n}$	0.013 s	0.4 s	0.4 s

The approximated delay of current controller from Fig. 4.4 can be observed as $T_{eq,i} = 0.35ms$. The mechanical time constant of the setup is $T_m = 1s$.

4.8 DC-link voltage control

The machine-side converter controls the dc-link voltage when the power plant runs in turbine mode. The schematic of a synchronous machine connected to the grid via a full-size back-to-back converter setup is shown in Fig. 4.10. Since the current sensors are connected at the output ac terminals, the outgoing current from the bridge-legs is denoted as positive current.

The voltage across the dc-link capacitor is related to the current through it as:

$$u_{dc} = \frac{1}{C_{dc}} \int i_{cap} dt \tag{4.45}$$

The voltage equation in (4.45) can be rewritten in standard state-space form as:

$$C_{dc} \frac{du_{dc}}{dt} = i_{cap} = -i_{dc1} - i_{dc2} \tag{4.46}$$
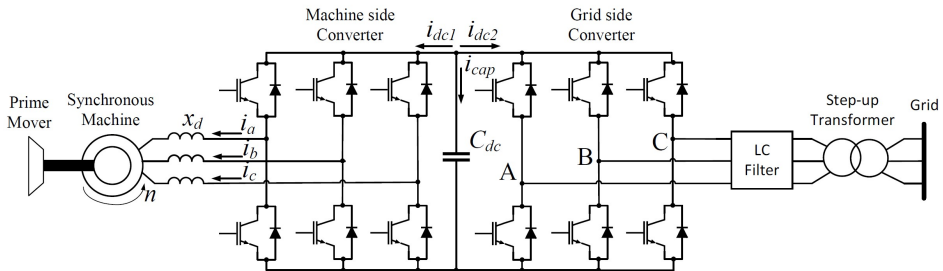
Figure 4.10: Schematic of the synchronous machine connected to the grid via a back-to-back two-level three-phase converter. Currents out of the converter bridge-legs have been assigned positive signs.

The dc-link voltage equation in (4.46) can be per unitized as presented in Appendix E. A dc-link time constant T_{dc} can be introduced as in the case of the angular speed of a motor:

$$T_{dc}\frac{du_{dc,pu}}{dt} = i_{cap,pu} = -i_{dc1,pu} - i_{dc2,pu} \qquad (4.47)$$

From ac and dc side power balance, the expression for per unit power can be written as:

$$p = u_{dc} \cdot i_{dc} = n \cdot \tau_e \qquad (4.48)$$

Since the machine-side converter is controlling the dc-link voltage, the dc current on the grid-side converter ($i_{dc2,pu}$) can be regarded as a disturbance and can be excluded while designing the controller. Hence, from (4.47) and (4.48):

$$T_{dc}\frac{du_{dc}}{dt} = -i_{dc1} = -\frac{n}{u_{dc}}\tau_e \qquad (4.49)$$

Since the closed-loop current control is very fast compared to the outer control loop for dc-link voltage, it can be lumped together as a low fast filter with a time constant, $T_{eq,i}$, as in the case of the design of speed controller. The modified relation can be presented as:

$$T_{dc} \cdot s \cdot u_{dc}(s) = -\frac{n}{u_{dc}}\frac{1}{1+T_{eq,i}s}\tau_{e,ref} = -\frac{n}{u_{dc}}\psi_s\frac{1}{1+T_{eq,i}s}i_{s,ref} \qquad (4.50)$$

The schematic of the control flow of the dc-link voltage controller is as presented in Fig. 4.10. From the block diagram, the open loop transfer function for the dc-link voltage can be established as:

$$u_{dc}(s) = \frac{1}{T_{dc}s} \cdot \frac{n}{u_{dc}} \cdot \frac{1}{1+T_{eq,i}s} \cdot K_{p,udc}\frac{1+T_{i,udc}s}{T_{i,udc}s}(u_{dc,ref} - u_{dc}) \qquad (4.51)$$

The negative sign from (4.50) is eliminated in (4.51) because the current reference produced by the dc-link voltage current controller is negative. The current flowing out of the bridge-legs of the converter is assumed as positive.

$$h_o(s) = \frac{u_{dc}}{u_{dc,ref}} = K_{p,udc}\frac{1+T_{i,udc}s}{T_{i,udc}s}\frac{n}{u_{dc}}\frac{1}{1+T_{eq,i}s}\frac{1}{T_{dc}s} \qquad (4.52)$$
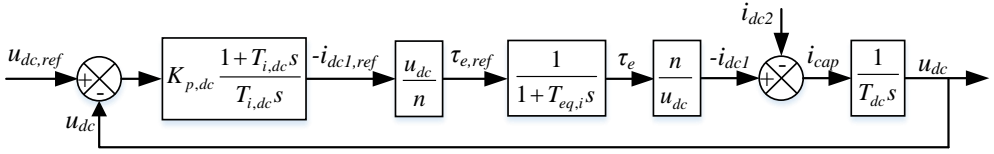
Figure 4.11: Schematic of the control flow of the dc-link voltage controller.

Similar to the case of the design of the speed controller, the open loop transfer function has two integrators; therefore, a symmetric optimum can be used. Comparing (4.52) with the Symmetric Optimum transfer function as presented in Appendix B, the gain and time constant of the PI controller can be obtained as:

$$
\begin{aligned}
T_{i,udc} &= \beta\, T_{sum} \\
K_{p,udc} &= \frac{u_{dc}}{n} \frac{T_{dc}}{\sqrt{\beta} T_{sum}} \\
T_{sum} &= T_{eq,i} + T_f, \text{ here }, \ T_f = 0
\end{aligned}
\tag{4.53}
$$

The gain $K_{p,udc}$ is dependent on speed and dc-link voltage, which varies dynamically. Therefore, with an additional adaptive gain of u_{dc}/n at the output of the controller as shown in Fig. 4.11, $K_{p,udc}$ is simplified as:

$$
K_p = \frac{T_{dc}}{\sqrt{\beta} T_{sum}}
\tag{4.54}
$$

The value of β is again selected the same way as in the case of the design of the speed controller. The dc-link voltage reference ($u_{dc,ref}$) normally remains constant; therefore, it is tuned with the consideration that the voltage remains within the acceptable limit of $\pm 5\%$ during step load on the grid side converter.

4.8.1   Tuning of dc-link voltage controller

The converter for the synchronous machine controls the dc-link voltage in the turbine mode of operation. The parameters for the dc-link controller were tuned in the laboratory setup and the response recorded was as presented in Fig. 4.12.

The practically tuned values of the controller parameters and the theoretically calculated values based on (4.54) are presented in Table 4.3.

While tuning the dc-link voltage controller using symmetrical optimum, higher β is chosen than the conventional Symmetrical Optimum rule of $\beta = 4$. This is because a lower β gives a higher gain, which amplifies any noise in the dc-link
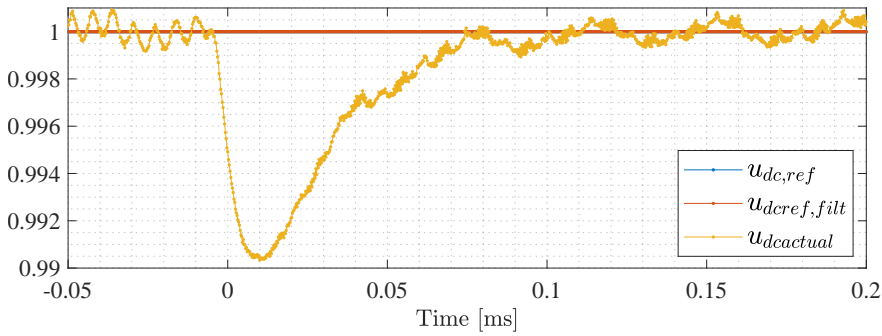
Figure 4.12: Response of dc-link voltage controller of the machine side converter controlling the dc-link voltage. A load step of 80 A (0.55pu) is applied on the dc-link using the grid-side converter at $t = 0s$.

Table 4.3: Theoretically calculated and experimentally tuned values of dc-link voltage controller of the machine side converter.

Parameters	Theoretical ($\beta = 4$)	Theoretical ($\beta = 20$)	Experimental
$K_{p,udc}$	18.3	8.18	10
$T_{i,udc}$	1 ms	7 ms	8 ms

Here, $T_{dc} = C_{dc} \cdot \frac{8}{3} Z_{base}= 3mF \cdot \frac{8}{3} \cdot 1.6\Omega = 12.8 \; ms$. From Fig. 4.4, $T_{sum} = T_{eq,i} = 0.35ms$

voltage measurement. Therefore, a higher value $\beta = 20$ is chosen, which gives a relatively lower gain, and the response of the dc-link voltage controller with a load step of 0.55 pu inflicts a drop of only 1% in dc-link voltage.

4.9   Conclusion

The stator current controllers and the excitation current controllers are the basic building blocks of the control of the synchronous machine in both the pump and turbine modes of operation. These controllers are tuned to achieve the best possible response (fast rise time and minimal overshoot). In addition, the speed controller and the dc-link voltage controller are also tuned to obtain the minimum possible deviation from the reference value in response to a step load. Theoretically calculated values are always the best starting point for tuning these controllers. The values in the laboratory have differed due to several unknown parameters, for example, the exact value of transient and subtransient reactances and time constants.

Chapter 5

Selection of Converter Topology

*The basic requirements for retrofitting a fixed speed pumped storage plant with a full-size converter to enable the variable speed operation are transformerless connection, high starting torque, and smallest possible sine filter or dv/dt filter at the converter output. There are various converter topologies that can meet these requirements. This chapter evaluates the multilevel converter topologies that can meet these specifications and recommends the selection criteria of the full-size converter for a synchronous machine unit of around 100 MVA, which addresses the **Research question 1**.*

5.1 Introduction

There exist several power electronics converter topologies for the application of the drive. The most popular converter topology in the low voltage application has been the two-level three-phase converters. Yet, as the required output voltage increases, the voltage steps also increase. This leads to higher dv/dt which is not acceptable for retrofit purposes where the machines are designed to operate at almost sinusoidal voltages. In addition, the number of semiconductor devices to be connected in series increases due to the available voltage rating of these devices.

The converter topologies known for high-power applications using power thyristors are load-commutated inverters (LCI) and cycloconverters. These types of converters are still used for some special applications; for example, an LCI converter of 101 MW was installed at the NASA wind tunnel in 1995 [55, 56]. The major drawback of the LCI converter is the low-order harmonic current on the source and load side. Therefore, it requires a significantly large size of passive filtering components compared to its power rating. Cycloconverters of 100 MVA have recently

been installed at Goldisthal Pumped Storage Plant to feed the rotor winding of a 340 MVA doubly fed induction machine [34, 14]. Since the output frequency of a Cycloconverter is limited to one-third of the input frequency, it is better suited for slip power recovery converters or other low-frequency applications.

The matrix converter converts the input voltage to the required output voltage without any intermediate dc-link or any energy storage. However, it has a maximum output-to-input voltage transfer ratio of 86% [57]. Therefore, it is not preferred as an appropriate solution for transformerless connection in an existing power plant with a synchronous machine.

The three-level neutral point clamped (NPC) and active NPC converter topologies are the most popular for medium voltage drive applications. These converters have been in use for more than two decades for marine, wind power, and other industrial applications. The output voltage level of these converters can be increased by connecting multiple semiconductor devices in series. The weighted total harmonic distortion (WTHD) of the output voltage of such converters improves to 1.7% compared to 4.1% for a two-level converter [58]. Therefore, these topologies are considered for further evaluation for the application in question. The other higher-order multilevel converters, e.g., five-level or seven-level converters are not considered because these converters constitute a relatively larger number of active components (switches and diodes) and passive components (dc-link capacitors) compared to three-level converters but the total harmonic distortion (THD) and WTHD of the output voltage does not improve with the same ratio [58, 59].

Modular multilevel converter (MMC) topology is one of the possible solutions as it synthesizes the output voltage using several modules in series. The control-related challenges at the low-speed operation of MMC have been studied for more than a decade. The study suggests that the MMC topology has the potential to meet the given requirements of the pumped storage plants. It comes with individual modules with half-bridge or full-bridge cells. A direct ac/ac MMC with full-bridge cells is also available and can provide full torque in the low-speed region as well. Such an MMC of 85 MVA has recently been installed at a pumped storage plant in Austria [22].

With today's technology, around 100 MW is the cut-off point for CFSM, i.e., for applications above 100 MW, DFIM is favorable due to the size of the converter [5]. The rapid development in the field of semiconductor devices shows the prospect of 10–25 kV SiC MOSFET and IGBT coming into the market in the near future. Such devices with high current ratings would pave the way to achieve high power and high-efficiency converters. With this increased rating of semiconductor devices, converters up to 500 MVA could be possible with MMC configurations [60].

Table 5.1: Commercially available medium voltage drives [61, 62, 63].

Manufacturer	Type	Power	Voltage (kV)	Topology	Semi-conductor	Control
ABB	ACS 1000	$0.3 - 5\, MVA$	2.3; 3.3; 4.0; 4.16	3L-NPC-VSC	IGCT	DTC
	ACS 5000	$1.7 - 24\, MVA$	6.0; 6.6; 6.9	5L-NPC-HB-VSC	IGCT	DTC
	ACS 6000	$3 - 36\, MVA$	2.3; 3.0; 3.3	3L-NPC-VSC	IGCT	DTC
	PCS 8000	$50\, MVA$	6.6	3L-ANPC	IGCT	—
	SFC Light	$40 - 300\, MVA$	$10 - 20$	Direct MMC	IGCT	—
GE	MV7B37-5L	$30 - 38\, MVA$	11	5 Level NPC	IGBT	—
	MV7D45-5L	$38 - 48\, MVA$	13.8	5 Level NPC	IGBT	—
SIEMENS	SINAMICS PERFECT HARMONY GH150	$4 - 35\, MVA$	$4.16 - 13.8$	MMC	IGBT	Vector Control
	SINAMICS PERFECT HARMONY GH180	$upto\ 34\, MVA$	$4.0 - 11.0$	MMC	IGBT	Vector Control

Note: PCS 8000 and SFC Light from ABB are installed at Grimsel-2 for a 100 MW unit and at the Malta project for an 80 MW unit respectively.

One of the requirements for the converters of a retrofit project to enable a fixed-speed pumped storage plant to variable speed is the transformerless connection of the synchronous machine to the generator transformer. For example, the converter output voltage toward the grid side and machine side for a machine around 100 MVA is in the range of 13–15 kV and then it is stepped up by the generator transformer. Converters with an output voltage in this range are not widely available even with medium voltage drives in industrial applications. The current status of the medium voltage converters available in the market for high-power applications is as presented in Table 5.1. The converter topologies that are considered suitable for the PSHP application have been further analyzed in a later section.

5.2   Converter topology

The most popular and mature converter topology in medium voltage industrial drives is the three-level neutral point clamped converter topology in MW (up to 30 MVA) power rating. An active NPC converter is also employed whenever high starting torque is required. In a pumped storage plant with a reversible pump turbine, the starting torque requirement is approximately 15% of the rated full load torque. This is primarily because of the combined inertia of the machine shaft and turbine and the friction due to water in the runner casing. Thus, a higher starting torque is necessary to accelerate the machine quickly to the rated speed. An acceleration time of 30–60 seconds in pump mode can be regarded as a very fast startup compared to the present-day solution with DFIM technology.

The modular multilevel converter is already widely used in HVDC applications and is now being introduced for commercial medium voltage drive applications. There have been several studies [9, 10, 11] carried out to address the operating challenges of MMC in low-frequency regions for drive applications.

Considering the suitability of these converters according to the application-associated requirements, the following three converter topologies have been further discussed:

- Three-level neutral point clamped (NPC) converter

- Three-level active neutral point clamped (ANPC) converter

- Modular multilevel converter (MMC)

These converters have been analyzed in detail in the following sections based on analytical equations. While analyzing the components of these converter topologies for the power output range of 100 MVA, the following figure of merits are considered as the basic parameters to be fulfilled [64]:

- Power losses

- Thermal impedance

- Maximum junction temperature of the device

- Maximum current that can be switched by the device

5.3   Three-level NPC converter

The three-level NPC converter has been the major workhorse in the medium–voltage drive applications [9]. Many power drives with a voltage rating of up to 6.6 kV are widely used in industries employing NPC converter topology. The schematic of the topology is shown in Fig. 5.1. The converter topology is analyzed for its power rating based on the worst-case losses in the semiconductor devices at rated frequency operation and at standstill. The conduction and switching losses in the semiconductor devices at each position in one of the bridge-leg are analyzed using analytical loss equations. The equations are outlined in the following section.

5.3.1   Analytical loss equations for rated operation

In a sinusoidal PWM modulated NPC converter, the current through the semiconductor devices is quite discontinuous as shown in Fig. 5.2. In this analysis, the
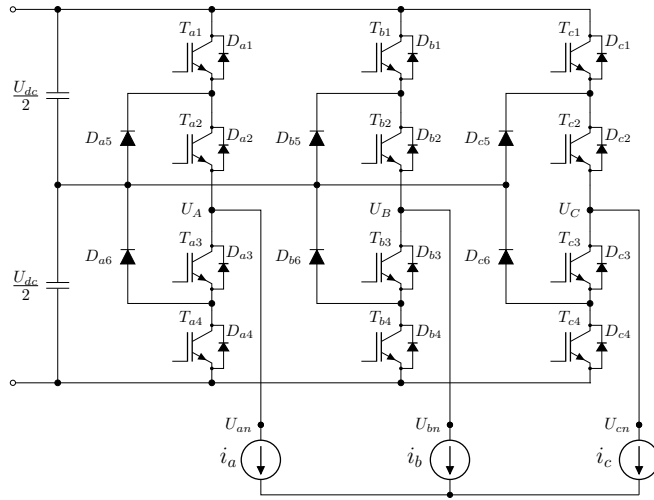
Figure 5.1: Schematic of a three-level three-phase Neutral Point Clamped (NPC) Converter. The load current has been assumed as pure sinusoidal for loss analysis.

Level Shifted PWM strategy is used to control the switching devices. The width of the microscopic pulses depends upon the carrier frequency (f_{sw}) and the amplitude of the sinusoidal modulation index (m_a). The number of pulses over one cycle depends on the frequency modulation ratio (m_f) as in (5.1):

$$m_f = \frac{f_{sw}}{f_n} \tag{5.1}$$

where, f_{sw} is the switching frequency or the frequency of the carrier waves (c_1 and c_2) shown in Fig. 5.2 and f_n is the frequency of the fundamental component of the output voltage or current.

The current through all switches and diodes of bridge leg "A" is presented in Fig. 5.2. Examining the symmetry of the position of the devices and the current through them, it is apparent that the losses in the upper devices T_1, D_1, T_2, D_2, and D_5 of a bridge-leg are the same as that in the lower devices.

The averaging method samples the discontinuous current signals through the devices within a switching interval and transforms it into a continuous microscopic mean or RMS signal. Therefore, the higher the switching frequency, the larger the number of microscopic mean values, resulting in higher accuracy. Mathematically, this method integrates the multiplication of m_a and the output current (e.g., i_a for phase A); it takes the average of it over a cycle. The method to calculate the average and rms of these microscopic currents over a fundamental cycle in a
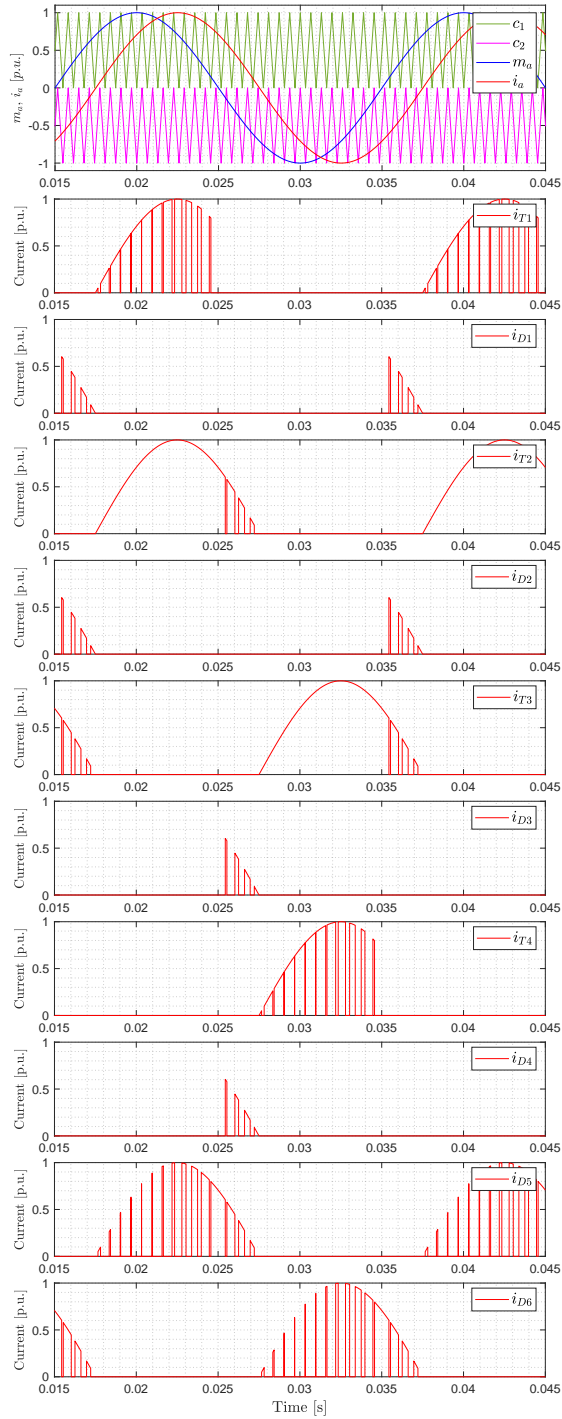
Figure 5.2: Currents through devices of Leg "A" of NPC converter at $f_n = 50\ Hz$, $f_{sw} = 1500\ Hz$, and $\varphi = -\pi/4$.

two-level three-phase converter is as presented in Fig. 5.3 [65]. The same method has been employed in prior studies to derive the analytical equations to calculate the average and rms currents in a neutral point clamped converter in [66, 67].
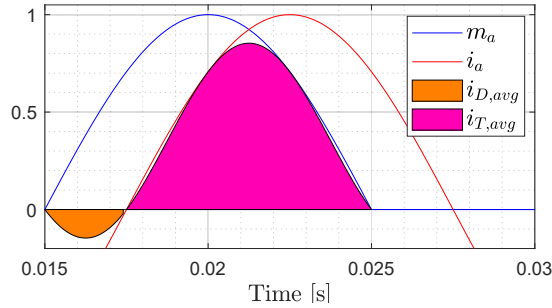
Figure 5.3: Averaging method of PWM pulsed current through semiconductor devices in converter applications. The legends used are the modulation index (m_a), the converter output current (i_a), the area corresponding to average current through switch T_{a1} ($i_{T,avg}$), and the similar area through diode D_{a1} ($i_{D,avg}$). The current i_a is lagging the m_a by power factor angle $\varphi = -\pi/4$.

The analytical equations to calculate the average currents are carried out with the sinusoidal PWM modulation technique. The modulation signals–m_a, m_b, and m_c– are as:

$$
\begin{aligned}
m_a &= M\cos(\omega t) \\
m_b &= M\cos(\omega t - 2\pi/3) \\
m_c &= M\cos(\omega t + 2\pi/3)
\end{aligned}
\tag{5.2}
$$

The load is modeled as a pure sinusoidal current source for approximate analysis and the phase angle (φ) is controlled w.r.t. the phase of the modulation signal m_a for the phase "a" as:

$$
\begin{aligned}
i_a &= \hat{I}_o\cos\left(\omega t + \varphi\right) \\
i_b &= \hat{I}_o\cos\left(\omega t + \varphi - 2\pi/3\right) \\
i_c &= \hat{I}_o\cos\left(\omega t + \varphi + 2\pi/3\right)
\end{aligned}
\tag{5.3}
$$

where, i_a, i_b, and i_c are the instantaneous output currents and $\hat{I}_o$ is the peak of the these currents.

5.3.1.1   Conduction loss

The voltage drop across a semiconductor device during the conduction period can be approximated as a forward voltage (U_{CE0}) and an Ohmic drop ($R_{CE,on}$) in series with that voltage. It can be expressed mathematically as:

$$u_{CE} = U_{CE0} + R_{CE,on} \cdot i \tag{5.4}$$

The conduction loss is the product of the instantaneous current through the semiconductor device and the voltage drop across it. The average conduction loss over one fundamental period, T_p, can be expressed as:

$$P_{con,loss} = \frac{1}{T_p} \int (u_{CE} \cdot i) \, dt \tag{5.5}$$

Inserting (5.4) into (5.5) yields:

$$P_{con,loss} = U_{CE0} \cdot I_{avg} + R_{CE,on} \cdot I_{rms}^2 \tag{5.6}$$

where,

$$I_{avg} = \frac{1}{T_p} \int_0^{T_p} i \, dt \tag{5.7}$$

$$I_{rms}^2 = \frac{1}{T_p} \int_0^{T_p} i^2 \, dt \tag{5.8}$$

According to (5.6), the conduction loss can be calculated using the average and rms value of the discontinuous current through the semiconductor devices. The average and rms value of current through the devices T_1 and D_1 can be calculated using the averaging method presented in Fig. 5.3. The integration is taken from $3\pi/2$ to $5\pi/2$ as the cosine wave has a positive half-cycle between these intervals.

$$
\begin{aligned}
I_{T1,avg} &= \frac{1}{2\pi} \int_{3\pi/2+\varphi}^{5\pi/2} m_a i_a d\omega t \\
&= \frac{M\hat{I}_o}{4} \cos\varphi + \frac{M\hat{I}_o}{4\pi} \left(\sin|\varphi| - |\varphi| \cos\varphi \right)
\end{aligned}
\tag{5.9}
$$

$$I_{T1,rms}^2 = \frac{1}{2\pi} \int_{3\pi/2+\varphi}^{5\pi/2} m_a i_a^2 d\omega t \tag{5.10}$$

$$= \frac{M\hat{I}_o^2}{6\pi}(1 + \cos\varphi)^2$$

$$I_{D1,avg} = \frac{1}{2\pi} \int_{3\pi/2}^{3\pi/2+\varphi} (-m_a i_a)\, d\omega t \tag{5.11}$$

$$= \frac{M\hat{I}_o}{4\pi}[\sin|\varphi| - |\varphi|\cos\varphi]$$

$$I_{D1,rms}^2 = \frac{1}{2\pi} \int_{3\pi/2}^{3\pi/2+\varphi} m_a i_a^2 d\omega t \tag{5.12}$$

$$= \frac{M\hat{I}_o^2}{6\pi}(1 - \cos\varphi)^2$$

The current through the switch T_1 and diode D_1 in the NPC and ANPC converter topologies are the same; therefore, the average and rms currents, and hence, the conduction loss in these devices, would be the same in both cases.

Similar expressions for the average and rms currents through the switch T_2 and diodes D_2 and D_5 can be derived as presented in Appendix D. The average and rms current expressions are as:

$$I_{T2,avg,npc} = \frac{\hat{I}_o}{\pi}\left[1 - \frac{M}{4}\left(\sin|\varphi| - |\varphi|\cos\varphi\right)\right] \tag{5.13}$$

In the NPC converter, the diode D_1 and D_2 conduct simultaneously and have the same average and rms current flowing through them.

$$I_{D5,avg,npc} = \frac{\hat{I}_o}{\pi}\left[1 - \frac{M}{2}\left(\sin|\varphi| + \left(\frac{\pi}{2} - |\varphi|\right)\cos\varphi\right)\right] \tag{5.14}$$

$$I_{T2,rms,npc}^2 = \frac{\hat{I}_o^2}{4}\left[1 - \frac{2M}{3\pi}(1 - \cos\varphi)^2\right] \tag{5.15}$$

$$I_{D5,rms,npc}^2 = \frac{\hat{I}_o^2}{4}\left[1 - \frac{4M}{3\pi}\left(1 + \cos^2\varphi\right)\right] \tag{5.16}$$

5.3.1.2   Switching loss

The switching loss in the semiconductor devices of a three-level NPC converter does not depend on the modulation index as it does not influence the number of switching over one cycle, however, the load power factor ($\cos \varphi$) does. The power factor other than unity makes the load current lead/lag the modulation index, and the current is shared between the switches and the anti-parallel diodes across them.

The switching loss characteristics from an experimental result can be approximated as the function of current, $e_{sw}(i)$, as:

$$e_{sw}(i) = k_{1,T} \cdot i + k_{2,T} \cdot i^2 \tag{5.17}$$

where $k_{1,T}$ and $k_{2,T}$ are the curve fitting coefficients at the rated blocking voltage (U_{dc}^*) determined using the experimental results or from the manufacturer's datasheet. The corresponding coefficients for diodes are $k_{1,D}$ and $k_{2,D}$.

Using these coefficients, the expressions for calculating the switching loss in each device can be formulated. The intervals at which the devices T_1 and D_1 switch are the same as in the calculation of average and rms current. The analytical equations for switching loss in the devices are:

$$
\begin{aligned}
P_{T1,sw} &= \frac{U_{dc}}{2U_{dc}^*} \frac{1}{2\pi} f_{sw} \int_{3\pi/2 + \varphi}^{5\pi/2} \left(k_{1,T} i + k_{2,T} i^2 \right) d\omega t \\
&= \frac{U_{dc}}{2U_{dc}^*} \frac{\hat{I}_o}{2\pi} f_{sw} \left[k_{1,T} \left(1 + \cos \varphi \right) + \frac{\hat{I}_o}{2} k_{2,T} \left(\pi - |\varphi| + \frac{1}{2} \sin 2 |\varphi| \right) \right]
\end{aligned}
\tag{5.18}
$$

where U_{dc} is the dc-link voltage as shown in Fig. 5.1 and U_{dc}^* is the rated blocking voltage of the semiconductor device provided by the manufacturers in the datasheet.

$$
\begin{aligned}
P_{D1,sw} &= \frac{U_{dc}}{2U_{dc}^*} \frac{1}{2\pi} f_{sw} \int_{3\pi/2}^{3\pi/2 + \varphi} \left(k_{1,D} i + k_{2,D} i^2 \right) d\omega t \\
&= \frac{U_{dc}}{2U_{dc}^*} \frac{\hat{I}_o}{2\pi} f_{sw} \left[k_{1,D} \left(1 - \cos \varphi \right) + \frac{\hat{I}_o}{2} k_{2,D} \left(|\varphi| - \frac{1}{2} \sin 2 |\varphi| \right) \right]
\end{aligned}
\tag{5.19}
$$

In the level shifted sinusoidal PWM modulation, the switch T_2 is continuously "ON" during the interval $3\pi/2$ to $5\pi/2$ ($t = 0.015s$ to $0.035s$ in Fig. 5.2). Therefore, the switch T_2 incurs the switching loss only if the load power factor is other

than unity, i.e., outside the aforementioned interval when the load current is leading or lagging the modulation index, m_a.

$$
\begin{aligned}
P_{T2,sw} &= \frac{U_{dc}}{2U_{dc}^*} \frac{1}{2\pi} f_{sw} \int_{5\pi/2}^{5\pi/2+\varphi} \left(k_{1,T} i + k_{2,T} i^2 \right) d\omega t \\
&= \frac{U_{dc}}{2U_{dc}^*} \cdot \frac{\hat{I}_o}{2\pi} f_{sw} \left[k_{1,T} \left(1 - \cos\varphi \right) + \frac{\hat{I}_o}{2} k_{2,T} \left(|\varphi| - \frac{1}{2} \sin 2 |\varphi| \right) \right]
\end{aligned}
$$

$$(5.20)$$

$$
\begin{aligned}
P_{D5,sw} &= \frac{U_{dc}}{2U_{dc}^*} \frac{1}{2\pi} f_{sw} \int_{3\pi/2+\varphi}^{5\pi/2} \left(k_{1,D} i + k_{2,D} i^2 \right) d\omega t \\
&= \frac{U_{dc}}{2U_{dc}^*} \frac{\hat{I}_o}{2\pi} f_{sw} \left[k_{1,D} \left(1 + \cos\varphi \right) + \frac{\hat{I}_o}{2} k_{2,D} \left(\pi - |\varphi| + \frac{1}{2} \sin 2 |\varphi| \right) \right]
\end{aligned}
$$

$$(5.21)$$

The diodes D_2 and D_3 have no switching loss in an NPC converter. These two diodes switch with no voltage across them, and therefore, there is no switching loss even in braking mode.

5.3.2   Loss equations for dc operation - NPC converter

As the fundamental frequency of the output voltage of the converter decreases, the thermal cycling period increases. This leads to a large swing in the junction temperature of the semiconductor devices switching during that period. Hence, the maximum loss in a switching device occurs at and around zero frequency, i.e., at dc operation. Therefore, it is important to analyze the losses in the semiconductor devices at dc operation, which defines the output current capability of the converter when the electrical machine connected to it is at a standstill.

The modulation index at dc operation is in the range of $M = 0.02 - 0.05$ to balance the voltage drop across the stator resistance of the machine and the losses in the converter. The current waveforms through the current carrying devices at dc operation are presented in Fig. 5.4. The switching of the devices depends on the direction of the current flow through the bridge leg.

5.3.2.1   Conduction loss at dc operation

The conduction loss in a semiconductor device when the output current is dc is calculated in the same way as for ac output current by using (5.6). However, the average and rms current values differ at dc operation as the current is not cyclic. Table 5.2 presents the average and rms current through the devices when the output current is positive and negative. These expressions can be used to calculate the conduction loss.
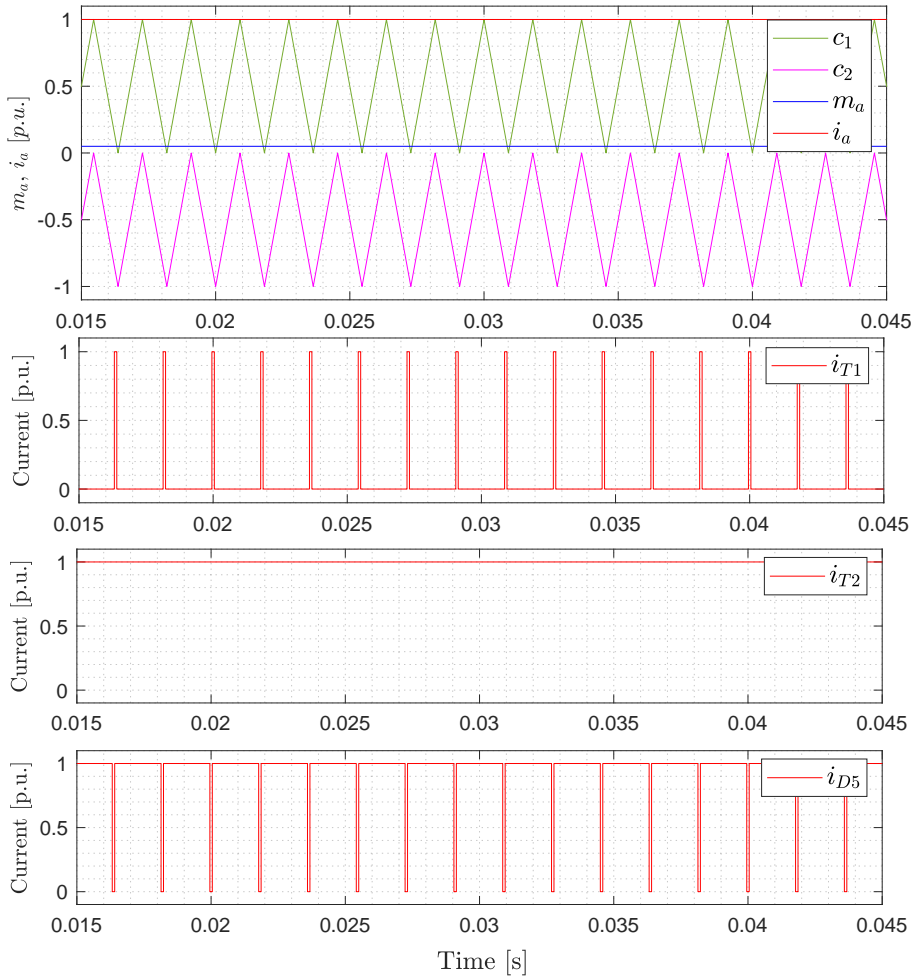
Figure 5.4: Currents through devices of Leg "A" of NPC converter at dc operation with $M = 0.05$, $f_{sw} = 500\,Hz$, $\varphi = 0$.

Table 5.2: Average and RMS current through devices of NPC converter at dc operation.

Current	$\hat{I}_o \geq 0$	$\hat{I}_o < 0$
$I_{T1,avg}$	$M \cdot \hat{I}_o$	0
$I_{D1,avg}$	0	$M \cdot \hat{I}_o$
$I_{T2,avg}$	$\hat{I}_o$	0
$I_{D2,avg}$	0	$M \cdot \hat{I}_o$
$I_{D5,avg}$	$(1 - M) \cdot \hat{I}_o$	0
$I_{T1,rms}^2$	$M \cdot \hat{I}_o^2$	0
$I_{D1,rms}^2$	0	$M \cdot \hat{I}_o^2$
$I_{T2,rms}^2$	$\hat{I}_o^2$	0
$I_{D2,rms}^2$	0	$M \cdot \hat{I}_o^2$
$I_{D5,rms}^2$	$(1 - M) \cdot \hat{I}_o^2$	0

5.3.2.2   Switching loss at dc operation

As the amplitude of the current at each switching instance is the same, the switching loss is maximum at dc operation. When the dc output current is positive, the current flows through the switches T_1 and T_2, and the diode D_5. The switching loss in these devices can be calculated using the following expressions:

$$P_{T1,sw@f=0} = \frac{U_{dc}}{2U_{dc}^*} f_{sw} \left(k_{1,T} \hat{I}_o + k_{2,T} \hat{I}_o^2 \right) \tag{5.22}$$

$$P_{T2,sw@f=0} = 0 \tag{5.23}$$

$$P_{D5,sw@f=0} = \frac{U_{dc}}{2U_{dc}^*} f_{sw} \left(k_{1,D} \hat{I}_o + k_{2,D} \hat{I}_o^2 \right) \tag{5.24}$$

The switch T_2 conducts continuously, and therefore, it does not incur any switching loss. The expressions (5.22)–(5.24) are valid for the switches T_4 and T_3, and the diode D_6, respectively, when $\hat{I}_o < 0$.
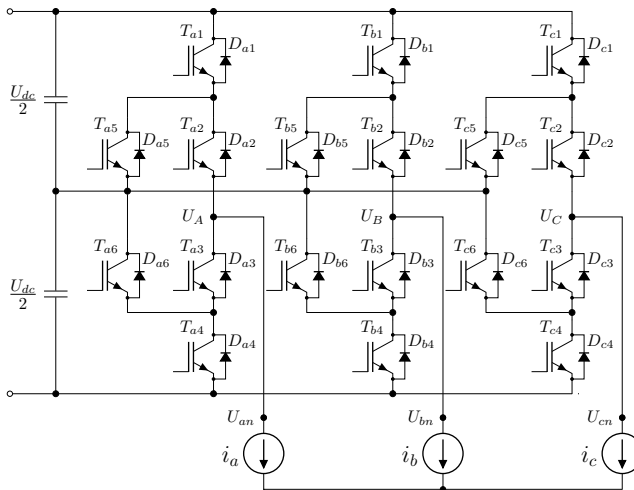
Figure 5.5: Schematic of a three-phase three-level Active Neutral Point Clamped (ANPC) Converter configuration.

5.4   Three-level ANPC converter

The ANPC converter is a preferred solution over the NPC converter where a single converter is required to achieve higher starting torque [68, 69]. The schematic of the topology is presented in Fig. 5.5. The two additional switches T_5 and T_6 across the clamping diodes D_5 and D_6 in each bridge leg share the current flow and hence distribute the losses more evenly compared to that in the NPC converter.

5.4.1   Analytical loss analysis of three-level ANPC converters

The current through each semiconductor device of bridge leg "A" of an ANPC converter is presented in Fig. 5.6. The Level Shifted Sinusoidal PWM Modulation strategy is used to control the switching devices. Similar to the case of the NPC converter, the position of the semiconductor devices in the upper half and the lower half in a bridge leg is symmetrical. Therefore, the losses in the upper devices T_1, D_1, T_2, D_2, T_5, and D_5 of the bridge-leg are the same as in the corresponding lower devices.

5.4.1.1   Conduction loss

The conduction loss in the semiconductor devices of an ANPC converter can be calculated in the same way as for the NPC converter using (5.6). The current through the outer devices (T_1, D_1, T_4, and D_4) of a bridge-leg are the same in both NPC and ANPC converters. Therefore, the average and rms current through these devices are calculated using (5.9)–(5.12).
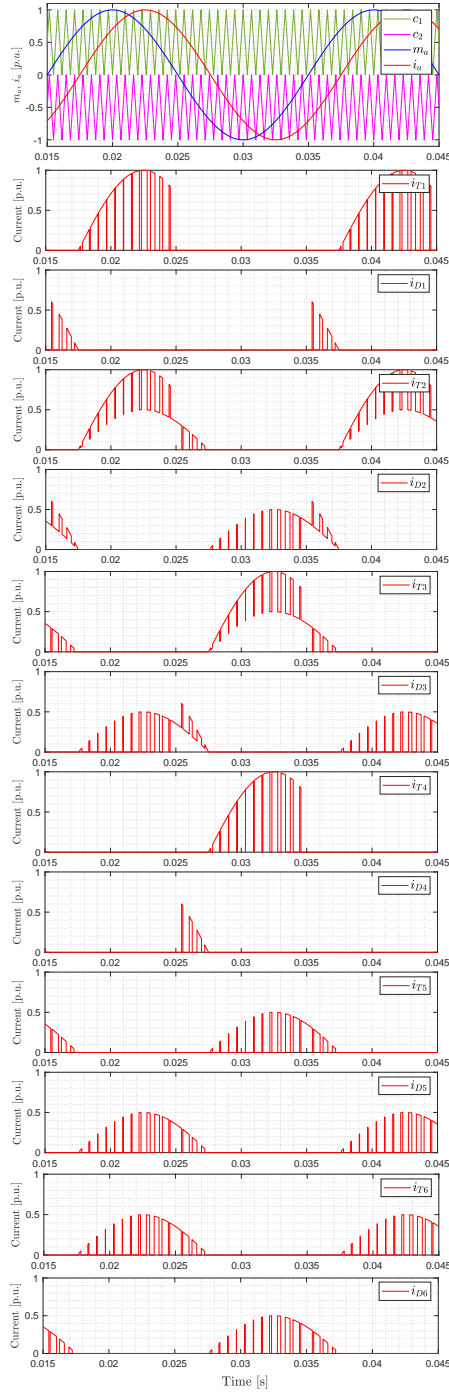
Figure 5.6: Current through the semiconductor devices of bridge-leg "A" of an ANPC converter at $f_n = 50\ Hz$, $f_{sw} = 1500\ Hz$, and $\varphi = -\pi/4$.

The equations to calculate the average and rms current through the inner switches T_2 and T_5, and diodes D_2 and D_5 are as:

$$
\begin{aligned}
I_{T5,avg} &= \frac{1}{2\pi} \int_{3\pi/2+\varphi}^{5\pi/2+\varphi} \frac{1}{2} i_a \, d\omega t - \frac{1}{2} I_{T1,avg} - \frac{1}{2} I_{D1,avg} \\
&= \frac{\hat{I}_o}{2\pi} \left[1 - \frac{M}{2} \left(\sin|\varphi| + \left(\frac{\pi}{2} - |\varphi| \right) \cos\varphi \right) \right]
\end{aligned}
\tag{5.25}
$$

$$
\begin{aligned}
I_{T5,rms}^2 &= \frac{1}{2\pi} \int_{3\pi/2+\varphi}^{5\pi/2+\varphi} \frac{1}{4} i_a^2 \, d\omega t - \frac{1}{4} I_{T1,rms}^2 - \frac{1}{4} I_{D1,rms}^2 \\
&= \frac{\hat{I}_o^2}{16} \left[1 - \frac{4M}{3\pi} \left(1 + \cos^2\varphi \right) \right]
\end{aligned}
\tag{5.26}
$$

$$
\begin{aligned}
I_{D5,avg} &= \frac{1}{2\pi} \int_{3\pi/2+\varphi}^{5\pi/2+\varphi} \frac{1}{2} i_a \, d\omega t - \frac{1}{2} I_{T1,avg} - \frac{1}{2} I_{D1,avg} \\
&= \frac{\hat{I}_o}{2\pi} \left[1 - \frac{M}{2} \left(\sin|\varphi| + \left(\frac{\pi}{2} - |\varphi| \right) \cos\varphi \right) \right]
\end{aligned}
\tag{5.27}
$$

$$
\begin{aligned}
I_{D5,rms}^2 &= \frac{1}{2\pi} \int_{3\pi/2+\varphi}^{5\pi/2+\varphi} \frac{1}{4} i_a^2 \, d\omega t - \frac{1}{4} I_{T1,rms}^2 - \frac{1}{4} I_{D1,rms}^2 \\
&= \frac{\hat{I}_o^2}{16} \left[1 - \frac{4M}{3\pi} \left(1 + \cos^2\varphi \right) \right]
\end{aligned}
\tag{5.28}
$$

$$
\begin{aligned}
I_{T2,avg} &= I_{T1,avg} + I_{D5,avg} \\
&= \frac{\hat{I}_o}{2\pi} + \frac{M\hat{I}_o}{8} \cos\varphi
\end{aligned}
\tag{5.29}
$$

$$
\begin{aligned}
I_{T2,rms}^2 &= I_{T1,rms}^2 + I_{D5,rms}^2 \\
&= \frac{\hat{I}_o^2}{4} \left[\frac{1}{4} + \frac{M}{3\pi} \left(1 + \cos^2\varphi + 4\cos\varphi \right) \right]
\end{aligned}
\tag{5.30}
$$

$$
\begin{aligned}
I_{D2,avg} &= I_{T5,avg} + I_{D1,avg} \\
&= \frac{\hat{I}_o}{2\pi} - \frac{M\hat{I}_o}{8} \cos\varphi
\end{aligned}
\tag{5.31}
$$

$$I_{D2,rms}^2 = I_{T5,rms}^2 + I_{D1,rms}^2$$
$$= \frac{\hat{I}_o^2}{4} \left[\frac{1}{4} + \frac{M}{3\pi} \left(1 + \cos^2\varphi - 4\cos\varphi \right) \right] \tag{5.32}$$

These average and rms current expressions can be used in (5.6) to calculate the conduction loss in the switches and diodes.

5.4.1.2 Switching loss

The switching loss in the outer switches T_1 and T_4, and diodes D_1 and D_4 of an ANPC converter have the same switching loss as for an NPC converter and is calculated using (5.18)–(5.19). The inner semiconductor devices have different losses as the amplitude of the current through these devices is different compared to that of the NPC converter.

In sinusoidal PWM modulation, the switch T_2 is continuously "ON" during the interval $3\pi/2$ to $5\pi/2$ ($t = 0.015s$ to $0.035s$ in Fig. 5.6). Therefore, T_2 will have switching loss only if the output current is leading or lagging the output voltage (or the modulation signal, m_a), i.e., outside the aforementioned interval. The analytical equations to calculate the switching loss in the switch T_2 and diode D_5 are derived as in (5.33) and (5.34):

$$P_{T2,sw} = \frac{U_{dc}}{2U_{dc}^*} \frac{1}{2\pi} f_{sw} \int_{5\pi/2}^{5\pi/2+\varphi} \left(k_{1,T} i + k_{2,T} i^2 \right) d\omega t$$
$$= \frac{U_{dc}}{2U_{dc}^*} \cdot \frac{\hat{I}_o}{4\pi} f_{sw} \left[k_{1,T} \left(1 - \cos\varphi \right) + \frac{\hat{I}_o}{4} k_{2,T} \left(|\varphi| - \frac{1}{2}\sin 2|\varphi| \right) \right] \tag{5.33}$$

$$P_{D5,sw} = \frac{U_{dc}}{2U_{dc}^*} \frac{1}{2\pi} f_{sw} \int_{3\pi/2 +\varphi}^{5\pi/2} \left(k_{1,D} i + k_{2,D} i^2 \right) d\omega t$$
$$= \frac{U_{dc}}{2U_{dc}^*} \frac{\hat{I}_o}{4\pi} f_{sw} \left[k_{1,D} \left(1 + \cos\varphi \right) + \frac{\hat{I}_o}{4} k_{2,D} \left(\pi - |\varphi| + \frac{1}{2}\sin 2|\varphi| \right) \right] \tag{5.34}$$

The diodes D_2 and D_5 have the same switching pattern but in different half cycles, and therefore, the switching loss over a cycle in these diodes is equal. The same applies to the switches T_2 and T_5.

5.4.2 Loss equations for dc operation - ANPC converter

At dc operation, only three devices—T_1, T_2, and D_5—conduct a positive output current in the case of the NPC converter whereas two additional devices, T_6 and

D_3 also conduct in the case of the ANPC converter as presented in Fig. 5.7. Since the current in the inner devices is shared, these individual devices incur less loss compared to the case of the NPC converter.

5.4.2.1   Conduction loss at dc operation

The current through the switch T_2 commutates from $\hat{I}_o/2$ to $\hat{I}_o$ for an interval determined by the modulation index. Similarly, the current through switch T_6 commutates from $\hat{I}_o/2$ to zero for the same interval. The devices D_5, T_6, and D_3 carry the same amount of current. Since the output current is dc, the average and rms current through the devices depend only on the modulation index (M) and the amplitude of output current ($\hat{I}_o$) as presented in Table 5.3.

Table 5.3: Average and RMS current through the devices of ANPC converter at dc operation ($f_n = 0$).

Current	$\hat{I}_o \geq 0$	$\hat{I}_o < 0$
$I_{T1,avg}$	$M \cdot \hat{I}_o$	0
$I_{D1,avg}$	0	$M \cdot \hat{I}_o$
$I_{T2,avg}$	$(1 + M) \cdot \frac{\hat{I}_o}{2}$	0
$I_{D2,avg}$	0	$(1 + M) \cdot \frac{\hat{I}_o}{2}$
$I_{T5,avg}$	0	$(1 - M) \cdot \frac{\hat{I}_o}{2}$
$I_{D5,avg}$	$(1 - M) \cdot \frac{\hat{I}_o}{2}$	0
$I_{T1,rms}^2$	$M \cdot \hat{I}_o^2$	0
$I_{D1,rms}^2$	0	$M \cdot \hat{I}_o^2$
$I_{T2,rms}^2$	$(1 + 3M) \cdot \frac{\hat{I}_o^2}{4}$	0
$I_{D2,rms}^2$	0	$(1 + 3M) \cdot \frac{\hat{I}_o^2}{4}$
$I_{T5,rms}^2$	0	$(1 - M) \cdot \frac{\hat{I}_o^2}{4}$
$I_{D5,rms}^2$	$(1 - M) \cdot \frac{\hat{I}_o^2}{4}$	0

 Note: The modulation index (M) is in the range of 0.02–0.05 at dc operation.

The conduction loss at dc current is calculated by inserting the average and rms current expressions from Table 5.3 in (5.6).
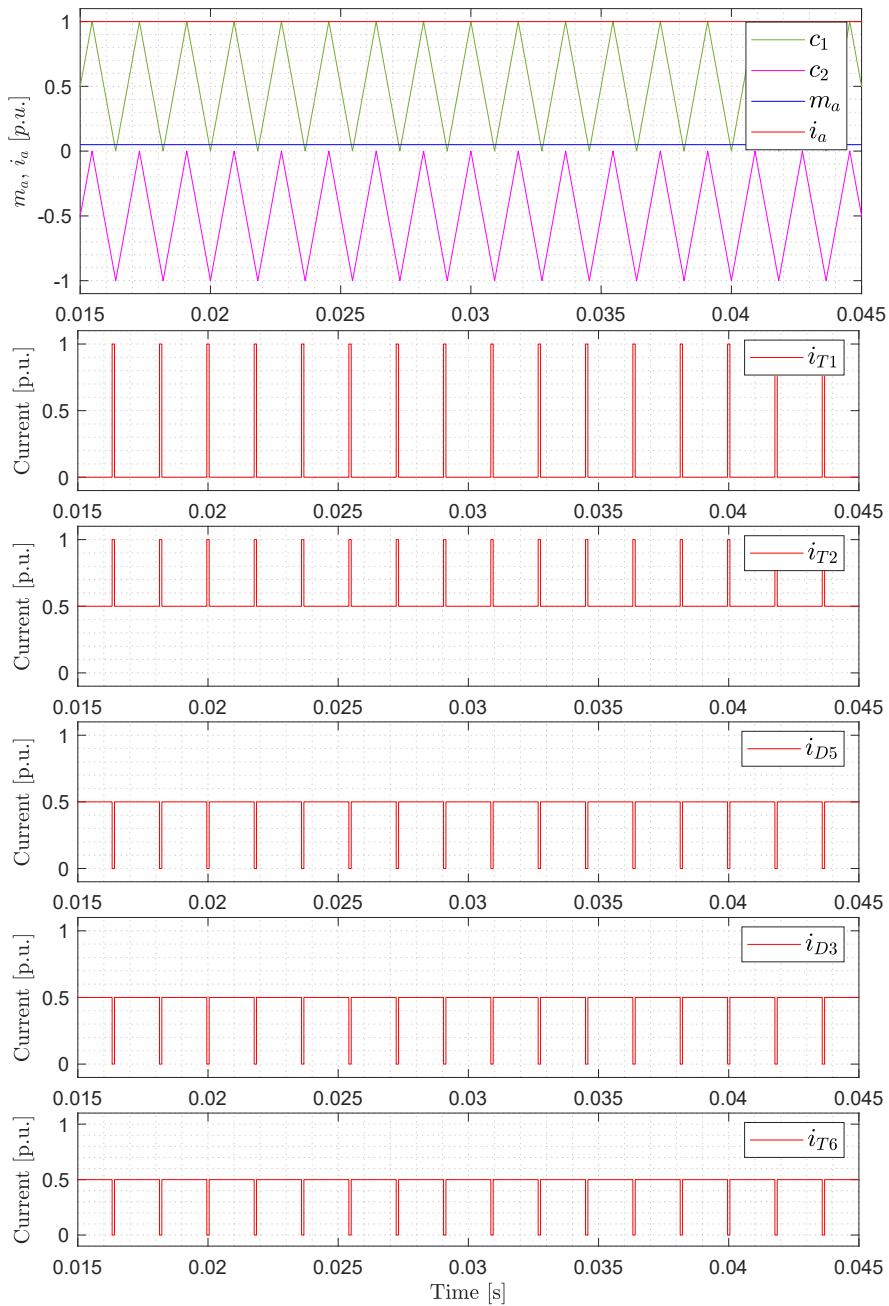
Figure 5.7: Current through devices of Leg "A" of ANPC converter at dc operation with $M = 0.05$, $f_{sw} = 500\,Hz$, $\varphi = 0$.

Table 5.4: Average and RMS current through the devices of NPC and ANPC converters at dc operation ($f_n = 0$).

Current	NPC		ANPC	
	$\hat{I}_o \geq 0$	$\hat{I}_o < 0$	$\hat{I}_o \geq 0$	$\hat{I}_o < 0$
$I_{T1,avg}$	$M \cdot \hat{I}_o$	0	$M \cdot \hat{I}_o$	0
$I_{D1,avg}$	0	$M \cdot \hat{I}_o$	0	$M \cdot \hat{I}_o$
$I_{T2,avg}$	$\hat{I}_o$	0	$(1+M) \cdot \frac{\hat{I}_o}{2}$	0
$I_{D2,avg}$	0	$M \cdot I_o$	0	$(1+M) \cdot \frac{\hat{I}_o}{2}$
$I_{T5,avg}$	$--$	$--$	0	$(1-M) \cdot \frac{\hat{I}_o}{2}$
$I_{D5,avg}$	$(1-M) \cdot \hat{I}_o$	0	$(1-M) \cdot \frac{\hat{I}_o}{2}$	0
$I_{T1,rms}^2$	$M \cdot \hat{I}_o^2$	0	$M \cdot \hat{I}_o^2$	0
$I_{D1,rms}^2$	0	$M \cdot \hat{I}_o^2$	0	$M \cdot \hat{I}_o^2$
$I_{T2,rms}^2$	$\hat{I}_o^2$	0	$(1+3M) \cdot \frac{\hat{I}_o^2}{4}$	0
$I_{D2,rms}^2$	0	$M \cdot \hat{I}_o^2$	0	$(1+3M) \cdot \frac{\hat{I}_o^2}{4}$
$I_{T5,rms}^2$	$--$	$--$	0	$(1-M) \cdot \frac{\hat{I}_o^2}{4}$
$I_{D5,rms}^2$	$(1-M) \cdot \hat{I}_o^2$	0	$(1-M) \cdot \frac{\hat{I}_o^2}{4}$	0

Note: The modulation index (M) is in the range of 0.02–0.05 at dc operation.

5.4.2.2   Switching loss at dc operation

For bridge leg "A", the switches T_1, T_2, and T_6 and diodes D_3 and D_5 conduct the positive output current but only the devices T_1, D_3, and D_5 incur the switching loss. There is no switching loss in switches T_2 and T_6 because these devices are continuously "ON".

As the output current is constant, the switching loss in device T_1 is calculated by substituting the instantaneous current (i) in (5.17) with the output current ($\hat{I}_o$).

$$P_{T1,sw@f=0} = \frac{U_{dc}}{2U_{dc}^*} f_{sw} \left(k_{1,T} \hat{I}_o + k_{2,T} \hat{I}_o^2 \right) \tag{5.35}$$

$$P_{T2,T5,sw@f=0} = 0 \tag{5.36}$$

$$P_{D3,D5,sw@f=0} = \frac{U_{dc}}{2U_{dc}^*} f_{sw} \left(k_{1,D} \frac{\hat{I}_o}{2} + k_{2,D} \frac{\hat{I}_o^2}{4} \right) \tag{5.37}$$

The accuracy of these analytical equations has been verified using simulations in MATLAB Simulink. These equations are used to calculate the switching loss in the individual switches and diodes of the ANPC converter. The sum of the conduction and switching loss gives the total loss in the particular switching device.

5.4.3   Selection of switching frequency

The analytical expressions can be used to calculate the conduction loss and switching loss in each switching device of the NPC and ANPC converters, and the critical devices can be determined while designing the converter. The DC operation is the most important for any type of converter as the conduction and switching losses are maximum at the same time for devices like D_5. An ANPC converter has parallel devices to deal with such issues and is, therefore, a better alternative for applications with high starting torque. However, this advantage can only be exploited if the switching loss in the device T_1 is lower than one-third of the total loss in this device.

This statement can be verified using the ratio of switching loss at dc operation as in (5.38) and the worst-case loss at rated frequency operation with $\cos \varphi = 1$ as in (5.18).

$$\frac{P_{T1,sw@f=0}}{P_{T1,sw@f=f_n}} = \pi \cdot \frac{k_{1,T} + k_{2,T} \cdot \hat{I}_o}{k_{1,T} + \frac{\pi}{4} k_{2,T} \cdot \hat{I}_o} \tag{5.38}$$

The coefficient $k_{2,T}$ is relatively very small compared to $k_{1,T}$ and can be neglected for approximate analysis. The ratio of the losses then becomes π. At dc operation, even though there is a very small conduction loss in T_1, the switching loss will increase by π times. Therefore, to keep the total loss at dc operation less than or equal to the total loss at rated frequency operation, the switching loss must be less than $1/\pi$ times the total loss, i.e., around 32% of total loss. This ratio is crucial in deciding the switching frequency of the converter.

5.4.4   Summary of average and RMS currents for NPC and ANPC

Table 5.5: Average and RMS current through the devices of NPC and ANPC converter.

Current	NPC	ANPC
$I_{T1,avg}$	$\frac{M\hat{I}_o}{4}\cos\varphi + \frac{M\hat{I}_o}{4\pi}\left(\sin|\varphi| - |\varphi|\cos\varphi\right)$	same as for NPC
$I_{D1,avg}$	$\frac{M\hat{I}_o}{4\pi}\left(\sin|\varphi| - |\varphi|\cos\varphi\right)$	same as for NPC
$I_{T2,avg}$	$\frac{\hat{I}_o}{\pi}\left[1 - \frac{M}{4}\left(\sin|\varphi| - |\varphi|\cos\varphi\right)\right]$	$\frac{\hat{I}_o}{2\pi}\left[1 + \frac{\pi}{4}M\cos\varphi\right]$
$I_{D2,avg}$	same as D_1	$\frac{\hat{I}_o}{2\pi}\left[1 - \frac{\pi}{4}M\cos\varphi\right]$
$I_{T5,avg}$	N/A	$\frac{\hat{I}_o}{2\pi}\left[1 - \frac{M}{2}\left(\sin|\varphi| + \left(\frac{\pi}{2} - |\varphi|\right)\cos\varphi\right)\right]$
$I_{D5,avg}$	$\frac{\hat{I}_o}{\pi}\left[1 - \frac{M}{2}\left(\sin|\varphi| + \left(\frac{\pi}{2} - |\varphi|\right)\cos\varphi\right)\right]$	same as T_5
$I^2_{T1,rms}$	$\frac{M\hat{I}_o^2}{6\pi}\left(1 + \cos\varphi\right)^2$	same as for NPC
$I^2_{D1,rms}$	$\frac{M\hat{I}_o^2}{6\pi}\left(1 - \cos\varphi\right)^2$	same as for NPC
$I^2_{T2,rms}$	$\frac{\hat{I}_o^2}{4}\left[1 - \frac{2M}{3\pi}\left(1 - \cos\varphi\right)^2\right]$	$\frac{\hat{I}_o^2}{4}\left[\frac{1}{4} + \frac{M}{3\pi}\left(1 + \cos^2\varphi + 4\cos\varphi\right)\right]$
$I^2_{D2,rms}$	same as D_1	$\frac{\hat{I}_o^2}{4}\left[\frac{1}{4} + \frac{M}{3\pi}\left(1 + \cos^2\varphi - 4\cos\varphi\right)\right]$
$I^2_{T5,rms}$	N/A	$\frac{\hat{I}_o^2}{16}\left[1 - \frac{4M}{3\pi}\left(1 + \cos^2\varphi\right)\right]$
$I^2_{D5,rms}$	$\frac{\hat{I}_o^2}{4}\left[1 - \frac{4M}{3\pi}\left(1 + \cos^2\varphi\right)\right]$	same as T_5

5.4.5　Summary of switching loss for NPC and ANPC

Table 5.6: Switching Loss expressions for devices of NPC and ANPC converters.

Device	NPC	ANPC
T_1	$\frac{U_{dc}}{2U_{dc}^*}\frac{\hat{I}_o}{2\pi}f_{sw}\left[k_{1,T}\left(1+\cos\varphi\right)+\frac{\hat{I}_o}{2}k_{2,T}\left(\pi-\lvert\varphi\rvert+\frac{1}{2}\sin 2\lvert\varphi\rvert\right)\right]$	$same\ as\ for\ NPC$
D_1	$\frac{U_{dc}}{2U_{dc}^*}\frac{\hat{I}_o}{2\pi}f_{sw}\left[k_{1,D}\left(1-\cos\varphi\right)+\frac{\hat{I}_o}{2}k_{2,D}\left(\lvert\varphi\rvert-\frac{1}{2}\sin 2\lvert\varphi\rvert\right)\right]$	$same\ as\ for\ NPC$
T_2	$\frac{U_{dc}}{2U_{dc}^*}\cdot\frac{\hat{I}_o}{2\pi}f_{sw}\left[k_{1,T}\left(1-\cos\varphi\right)+\frac{\hat{I}_o}{2}k_{2,T}\left(\lvert\varphi\rvert-\frac{1}{2}\sin 2\lvert\varphi\rvert\right)\right]$	$\hat{I}_o\ replaced\ by\ \frac{\hat{I}_o}{2}$
D_2	0	$same\ as\ for\ D_5$
T_5	N/A	$same\ as\ for\ T_2$
D_5	$\frac{U_{dc}}{2U_{dc}^*}\frac{\hat{I}_o}{2\pi}f_{sw}\left[k_{1,D}\left(1+\cos\varphi\right)+\frac{\hat{I}_o}{2}k_{2,D}\left(\pi-\lvert\varphi\rvert+\frac{1}{2}\sin 2\lvert\varphi\rvert\right)\right]$	$\hat{I}_o\ replaced\ by\ \frac{\hat{I}_o}{2}$

5.4.5.1   Switching loss for NPC and ANPC at zero speed

Table 5.7: Switching Loss expressions for devices of NPC and ANPC converters at zero speed ($i_o \geq 0, M > 0$ and $f_n = 0$).

Device	NPC	$ANPC$
T_1	$\frac{U_{dc}}{2U_{dc}^*} f_{sw} \left(k_{1,T} \hat{I}_o + k_{2,T} \hat{I}_o^2 \right)$	$same\ as\ for\ NPC$
D_1	0	0
T_2	0	0
D_2	0	0
T_5	$--$	0
D_5	$\frac{U_{dc}}{2U_{dc}^*} f_{sw} \left(k_{1,D} \hat{I}_o + k_{2,D} \hat{I}_o^2 \right)$	$\frac{U_{dc}}{2U_{dc}^*} f_{sw} \left(k_{1,D} \frac{\hat{I}_o}{2} + k_{2,D} \frac{\hat{I}_o^2}{4} \right)$

At dc operation, when the current out of phase "A" is positive, it returns through phases "B" and "C", i.e., the current in these two phases is negative. In this case, the switches in the lower half of the bridge legs "B" and "C" switch, i.e., the current returns through devices T_3 and D_6; and T_4. The switching loss in the case of NPC and ANPC for negative output current can be tabulated as outlined in Table 5.8:

Table 5.8: Switching Loss expressions for devices of NPC and ANPC converters at zero speed ($i_o < 0, M > 0$ and $f_n = 0$).

Device	NPC	$ANPC$
T_3	0	0
D_3	0	0
T_4	$\frac{U_{dc}}{2U_{dc}^*} f_{sw} \left(k_{1,T} \hat{I}_o + k_{2,T} \hat{I}_o^2 \right)$	$same\ as\ for\ NPC$
D_4	0	0
T_6	$--$	0
D_6	$\frac{U_{dc}}{2U_{dc}^*} f_{sw} \left(k_{1,D} \hat{I}_o + k_{2,D} \hat{I}_o^2 \right)$	$\frac{U_{dc}}{2U_{dc}^*} f_{sw} \left(k_{1,D} \frac{\hat{I}_o}{2} + k_{2,D} \frac{\hat{I}_o^2}{4} \right)$

5.5 Modular multilevel converter

The Modular Multilevel Converter (MMC) was first introduced in 2003 [70, 71] for the HVDC application, but since then, there has been extensive research on employing it in drives application. The large ripple in submodule capacitor voltage at lower frequency operation or continuous charging and discharging of the capacitor at dc operation have also been addressed in [9] and later in [10]. The schematic of an MMC is shown in Fig.5.8.

The relation between the arm currents ($i_{u,l}$), the output current (i_o), and the dc-link current (i_{dc}) at steady state operation are as:

$$i_u = \frac{1}{2}i_o + I_{z,dc} + i_{z,ac} \tag{5.39}$$

$$i_l = -\frac{1}{2}i_o + I_{z,dc} + i_{z,ac} \tag{5.40}$$
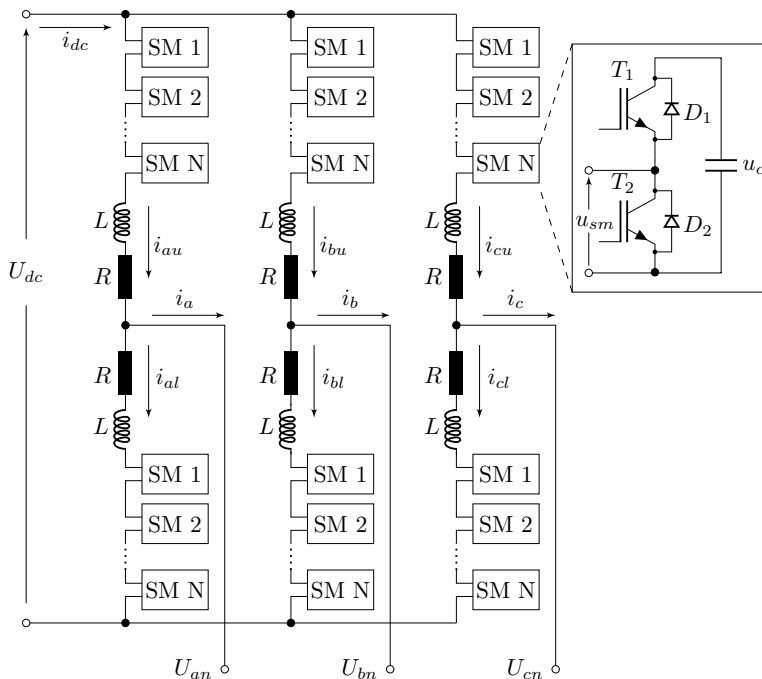
Figure 5.8: Schematic of a Modular Multilevel Converter with half-bridge sub-module configuration. A typical dc link voltage is 22 kV and the ac output voltage is 13 kV (rms). In the figure, "SM" stands for "sub-module" of the MMC, which constitutes semiconductor devices and a capacitor as shown in the inset.

where,

$$i_o = i_a = i_u - i_l = \hat{I}_o \sin(\omega t + \varphi) \qquad (5.41)$$

$$i_{circ} = \frac{1}{2}(i_u + i_l) = I_{z,dc} + i_{z,ac} \qquad (5.42)$$

$$I_{z,dc} = \frac{M\hat{I}_o}{4}\cos\varphi \qquad (5.43)$$

Here, $\hat{I}_o$ is the peak of output current, M is the peak of modulation index, and $\cos\varphi$ is the power factor. The circulating current (i_{circ}) consists of the dc component ($I_{z,dc}$) and the ac harmonics component ($i_{z,ac}$), which predominantly consists of 2nd harmonics of the output current in an open loop phase shifted PWM modulated MMC [72] given by:

$$i_2 = \mathrm{Re}\left\{ \frac{-j\left(\frac{3M}{8\omega}\hat{I}_o \cdot e^{j\varphi_{a1}} - \frac{M^2}{6\omega}i_{dc}\right)}{\frac{4C}{N}(R + j2\omega L) - j\frac{6+4M^2}{12\omega}} e^{j2\omega t} \right\} \qquad (5.44)$$

There exist several control methods to eliminate the ac current harmonics, known as circulating current suppression (CCS) control [73, 74, 75, 76, 77], such that only the dc-component of the circulating current flows through the arms. Then, the equations (5.39) and (5.40) become:

$$i_{u,l} = \pm\frac{\hat{I}_o}{2}\sin(\omega t + \varphi) + I_{z,dc} \qquad (5.45)$$

The CCS control remains active in normal operation to eliminate the additional losses in the semiconductor devices and passive elements caused by the higher harmonics current through the arms.

Unlike in the voltage source converters (VSCs), the load current itself flows through the submodule capacitors in an MMC. Hence, the amplitude and frequency of the output current have a direct impact on the voltage ripple in these capacitors. The expression for the ripple in submodule capacitor voltage ($\tilde{u}_{c,u}$) has been approximated in [78] as:

$$\tilde{u}_{c,u} = \frac{\hat{I}_o}{8\pi f_o C}\left[\frac{M^2\cos\varphi}{2}\cos\omega t - \cos(\omega t - \varphi) + \frac{M}{4}\sin(2\omega t - \varphi)\right] \qquad (5.46)$$

From (5.46), it is apparent that the capacitor voltage ripple increases as the output current ($\hat{I}_o$) increases or the output frequency (f_o) decreases, which is the case in drives application.

5.5.1   Analytical loss calculation

In all MMC applications, the ac part of the circulating current is suppressed using a circulating current suppression controller. In such a case, the arm currents expressions in (5.39) and (5.40) can be rewritten as follows:

$$i_u = \frac{\hat{I}_o}{2} \cos\left(\omega t + \varphi\right) + \frac{M\hat{I}_o}{4} \cos\varphi \tag{5.47}$$

$$i_l = -\frac{\hat{I}_o}{2} \cos\left(\omega t + \varphi\right) + \frac{M\hat{I}_o}{4} \cos\varphi \tag{5.48}$$

In the case of the upper arm current, the positive part of the current flows through the diode D_1 and into the capacitor when the submodule is inserted, whereas it flows through the switch T_2 when the submodule is bypassed. Similarly, the negative current flows through the devices T_1 and D_2. Hence, it is important to find the zero crossings of the arm currents to estimate the average and rms current through the semiconductor devices of a submodule.

Equating (5.47) to zero for ωt gives the zero crossings as follows:

$$\omega t = -\varphi + \sin^{-1}\left(\frac{-M\cos\varphi}{2}\right), \ \pi - \varphi - \sin^{-1}\left(\frac{-M\cos\varphi}{2}\right),$$
$$2\pi + \varphi - \sin^{-1}\left(\frac{-M\cos\varphi}{2}\right) \tag{5.49}$$

In simplified form, the zero crossings can be denoted as z_1, z_2, and z_3:

$$\begin{aligned} z_1 &= -\varphi + \theta_z, \\ z_2 &= \pi - \varphi - \theta_z, \\ z_3 &= 2\pi - \varphi + \theta_z = z_1 + 2\pi \end{aligned} \tag{5.50}$$

where,

$$\theta_z = \sin^{-1}\left(\frac{-M\cos\varphi}{2}\right) \tag{5.51}$$

These zero crossings can be observed in the arm current, i_{au}, in Fig. 5.9.

5.5.1.1   Conduction loss

The conduction loss in a semiconductor device of an MMC can be calculated in the same way as in an NPC or ANPC converter using (5.6).
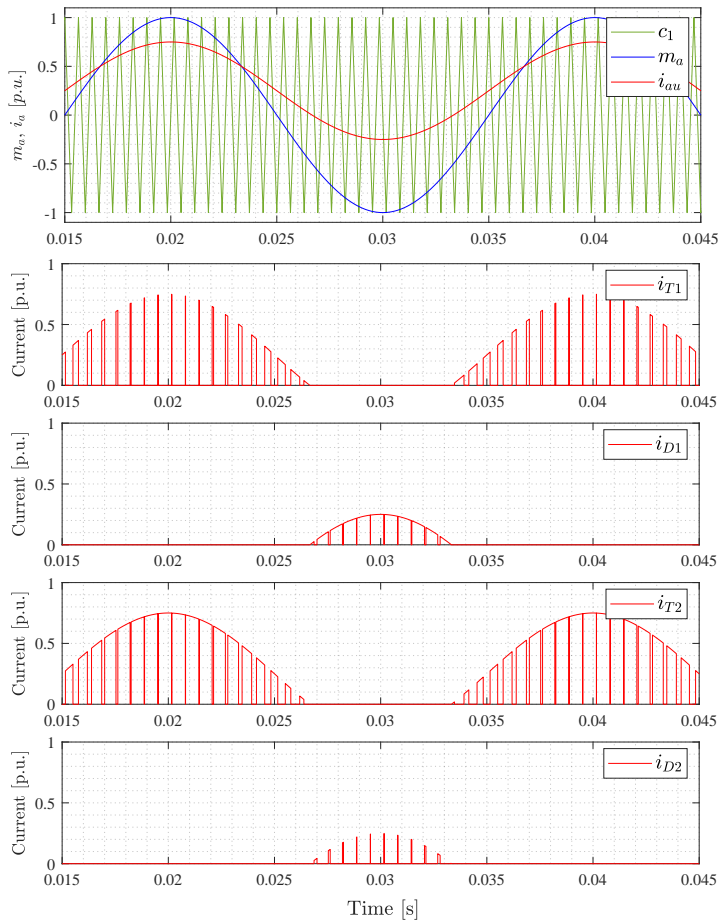
Figure 5.9: Current through devices of one submodule of the upper arm of an MMC with $M = 1$, $f_{sw} = 500\,Hz$, $f_n = 50\,Hz$, and $\varphi = 0$.

The constituents of conduction loss, I_{avg}, and I_{rms}, are calculated using the averaging method described in Section 5.3.1. The upper arm (i_u) and lower arm (i_l) currents normally have three zero-crossings over a cycle as the fundamental component of the load current does, as shown in Fig. 5.9. The positive upper arm current flows through devices D_1 and T_2, whereas the negative arm current flows through devices T_1 and D_2. The integral of the area between the first and second zero-crossings of Fig. 5.9 w.r.t. the modulation index gives the average and rms current for devices D_1 and T_2 and the same between the second and third zero-crossings gives the average and rms current for devices T_1 and D_2.

The average currents through each switch and diode of a sub-module can be expressed as follows:

$$I_{T1,avg} = \frac{1}{2\pi} \int_{z_{2,i_{au}}}^{z_{3,i_{au}}} \left[\frac{(1 - m_{a1})}{2} i_{au} \right] d\omega t \tag{5.52}$$

$$I_{D1,avg} = \frac{1}{2\pi} \int_{z_{1,i_{au}}}^{z_{2,i_{au}}} \left[\frac{(1 - m_{a1})}{2} i_{au} \right] d\omega t \tag{5.53}$$

$$I_{T2,avg} = \frac{1}{2\pi} \int_{z_{1,i_{au}}}^{z_{2,i_{au}}} \left[\frac{(1 + m_{a1})}{2} i_{au} \right] d\omega t \tag{5.54}$$

$$I_{D2,avg} = \frac{1}{2\pi} \int_{z_{2,i_{au}}}^{z_{3,i_{au}}} \left[\frac{(1 + m_{a1})}{2} i_{au} \right] d\omega t \tag{5.55}$$

Using the equations (5.52)–(5.55), the expressions for average current through the devices in a submodule are obtained as:

$$I_{T1,avg} = \frac{-\hat{I}_o}{16\pi} \left[\left(4 - 2M^2\cos^2\varphi \right) \cos\theta_z - M\cos\varphi \sin 2\theta_z \right] \tag{5.56}$$

$$I_{D1,avg} = \frac{\hat{I}_o}{16\pi} \left[\left(4 - 2M^2\cos^2\varphi \right) \cos\theta_z - M\cos\varphi \sin 2\theta_z \right] \tag{5.57}$$

$$I_{T2,avg} = \frac{\hat{I}_o}{16\pi} \left[\left(4 + 2M^2\cos^2\varphi \right) \cos\theta_z + M\cos\varphi \sin 2\theta_z \right. \\ \left. + 2M \left(\pi - 2\theta_z \right) \cos\varphi \right] \tag{5.58}$$

$$I_{D2,avg} == \frac{-\hat{I}_o}{16\pi} \left[\left(4 + 2M^2\cos^2\varphi \right) \cos\theta_z + M\cos\varphi \sin 2\theta_z \right. \\ \left. - 2M \left(\pi + 2\theta_z \right) \cos\varphi \right] \tag{5.59}$$

The average current through the devices T_1 and D_1 are the same in steady state operation such that the net average current through the capacitor is zero over one fundamental cycle. This keeps the average value of capacitor voltage constant over a cycle.

The square of rms currents through each semiconductor device of a sub-module can be presented as follows:

$$I_{T1,rms}^2 = \frac{1}{2\pi} \int\limits_{z_{2,i_{au}}}^{z_{3,i_{au}}} \left[\frac{(1-m_{a1})}{2} i_{au}^2 \right] d\omega t \tag{5.60}$$

$$I_{D1,rms}^2 = \frac{1}{2\pi} \int\limits_{z_{1,i_{au}}}^{z_{2,i_{au}}} \left[\frac{(1-m_{a1})}{2} i_{au}^2 \right] d\omega t \tag{5.61}$$

$$I_{T2,rms}^2 = \frac{1}{2\pi} \int\limits_{z_{1,i_{au}}}^{z_{2,i_{au}}} \left[\frac{(1+m_{a1})}{2} i_{au}^2 \right] d\omega t \tag{5.62}$$

$$I_{D2,rms}^2 = \frac{1}{2\pi} \int\limits_{z_{2,i_{au}}}^{z_{3,i_{au}}} \left[\frac{(1+m_{a1})}{2} i_{au}^2 \right] d\omega t \tag{5.63}$$

Using the equations (5.60)–(5.63), the expressions for the square of rms current through the submodule device are derived as follows:

$$\begin{aligned} I_{T1,rms}^2 = \frac{I_o^2}{128\pi} (&M^3 \cos 3\varphi \cos \theta_z - \frac{4M}{3} \cos \varphi \cos 3\theta_z + M \left(3M^2 - 4 \right) \cos \varphi \cos \theta_z \\ &+ 4 \left(M^2 \cos^2 \varphi - 1 \right) \sin (2\theta_z) - 2 \left(\pi + 2\theta_z \right) \left(M^2 \cos^2 \varphi - 2 \right)) \end{aligned} \tag{5.64}$$

$$\begin{aligned} I_{D1,rms}^2 = -\frac{I_o^2}{128\pi} (&M^3 \cos 3\varphi \cos \theta_z - \frac{4M}{3} \cos \varphi \cos 3\theta_z + M \left(3M^2 - 4 \right) \cos \varphi \cos \theta_z \\ &+ 4 \left(M^2 \cos^2 \varphi - 1 \right) \sin 2\theta_z + 2 \left(\pi - 2\theta_z \right) \left(M^2 \cos^2 \varphi - 2 \right)) \end{aligned} \tag{5.65}$$

$$\begin{aligned} I_{T2,rms}^2 = \frac{I_o^2}{128\pi} (&M^3 \cos 3\varphi \cos \theta_z - \frac{4M}{3} \cos \varphi \cos 3\theta_z + M \left(3M^2 + 28 \right) \cos \varphi \cos \theta_z \\ &+ 4 \left(M^2 \cos^2 \varphi + 1 \right) \sin 2\theta_z + 2 \left(\pi - 2\theta_z \right) \left(3M^2 \cos^2 \varphi + 2 \right)) \end{aligned} \tag{5.66}$$

$$\begin{aligned} I_{D2,rms}^2 = \frac{-I_o^2}{128\pi} (&M^3 \cos 3\varphi \cos \theta_z - \frac{4M}{3} \cos \varphi \cos 3\theta_z + M \left(3M^2 + 28 \right) \cos \varphi \cos \theta_z \\ &+ 4 \left(M^2 \cos^2 \varphi + 1 \right) \sin 2\theta_z - 2 \left(\pi + 2\theta_z \right) \left(3M^2 \cos^2 \varphi + 2 \right)) \end{aligned} \tag{5.67}$$

A comparison of analytically calculated average and rms current with the simulation results is presented in Table 5.9. The results indicate that the analytical values

have very high accuracy, and hence the conduction loss in the semiconductor devices can also be calculated to a very high accuracy using these values.

Table 5.9: Comparison of analytical and simulation values of average and rms currents through devices.

Device	T_1	D_1	T_2	D_2
$I_{avg,analytical}$ (A)	51.69	51.69	252.81	2.81
$I_{avg,sim}$ $(A)@f_{sw} = 333Hz$	50.26	50.60	254.58	1.30
$I_{avg,sim}$ $(A)@f_{sw} = 1665Hz$	49.27	50.40	255.92	1.73
$I_{rms,analytical}$ (A)	102.06	144.34	394.78	19.91
$I_{rms,sim}$ $(A)@f_{sw} = 333Hz$	104.37	146.93	396.19	9.24
$I_{rms,sim}$ $(A)@f_{sw} = 1665Hz$	101.86	142.36	399.50	16.03

5.5.1.2 Switching loss

The switching loss characteristics as a function of current, $e_{sw}(i)$, from an experimental result can be approximated as in (5.17). Substituting the upper arm current (i_{au}), which flows through the semiconductor devices of the submodules in the upper arm, the expressions for switching loss can be derived as in (5.68)–(5.71):

$$P_{T1,sw} = U_c \cdot \frac{1}{2\pi} f_{sw} \int_{z2}^{z3} \left(k_{1T} \cdot i + k_{2T} \cdot i^2 \right) d\omega t \tag{5.68}$$

$$
\begin{aligned}
P_{T1,sw} = & \frac{U_c I_o f_{sw}}{32\pi} \Big[4k_{1T} \left(M \left(\pi + 2\theta_z \right) \cos\varphi - 4\cos\theta_z \right) \\
& + k_{2T} I_o \left\{ \left(\pi + 2\theta_z \right) \left(M^2 \cos^2\varphi + 2 \right) - 4\cos\theta_z \left(\sin\theta_z + 2M\cos\varphi \right) \right\} \Big]
\end{aligned} \tag{5.69}
$$

$$P_{T2,sw} = U_c \cdot \frac{1}{2\pi} f_{sw} \int_{z1}^{z2} \left(k_{1T} \cdot i + k_{2T} \cdot i^2 \right) d\omega t \tag{5.70}$$

$$
\begin{aligned}
P_{T2,sw} = & \frac{U_c I_o f_{sw}}{32\pi} \Big[4k_{1T} \left(M \left(\pi - 2\theta_z \right) \cos\varphi + 4\cos\theta_z \right) \\
& + k_{2T} I_o \left\{ \left(\pi - 2\theta_z \right) \left(M^2 \cos^2\varphi + 2 \right) + 4\cos\theta_z \left(\sin\theta_z + 2M\cos\varphi \right) \right\} \Big]
\end{aligned} \tag{5.71}
$$

The diodes D_1 and D_2 follow the same expressions as that for switches T_2 and T_1, respectively, but with loss coefficients k_{1D} and k_{2D}. These expressions are used in

later sections to calculate the conduction and switching loss in an MMC at rated speed operation.

5.5.2   Low-speed operation - with common mode voltage injection

All semiconductor devices have either maximum conduction loss or maximum switching loss or both at zero speed. The total loss in the devices in the worst–case decides the current limit the converter can yield.

Considering V/f control of the machine, the amplitude of the applied voltage to the motor is decreased as the speed decreases to maintain a constant (1 pu) flux in the stator of the motor. Hence, at very low frequency or zero frequency, the modulation index (M) is very small (in the range of 0.03–0.05 pu) to compensate only for the drop in the stator resistance and switching components. According to (5.43), the dc component of the arm current ($I_{z,dc}$) approaches zero for the very low value of M. In this case:

$$\hat{V}_{ph,peak} = \frac{M \cdot v_{dc}}{2} \qquad\qquad (5.72)$$

$$i_{u,a} = \frac{\hat{I}_o}{2} \qquad \text{and,} \qquad i_{l,a} = -\frac{\hat{I}_o}{2} \qquad\qquad (5.73)$$

The output current in all phases and all arms will be dc current, but the instantaneous sum of the three-phase output currents will still be zero. As shown in Fig. 5.8, if the output current is positive dc in the bridge leg "A", the current either flows through the diode D_1 and charges the submodule capacitor, or it flows through the switch T_2 and bypasses the capacitor. Thus, the submodule capacitors in the upper arm in the upper arm keep on continuously charging and the capacitors in the lower arm keep on continuously discharging. A longer duration (at low frequency or zero frequency operation) can charge the capacitor to an unacceptably high value above its rated value, and the opposite will happen in the lower arm. To avoid such continuous charging and discharging of the capacitors, the arm current needs an ac component superimposed with the dc current such that the resultant current both charges and discharges the capacitor, and keeps the voltage ripple within the permissible limit.

Assuming the ac component as the sinusoidal current of angular frequency ω_{com}, and constants k_1 and k_2 as the factor by which the dc and ac components should

be scaled, the arm currents for phase "a" can be formulated as:

$$i_{u,a} = k_1 \frac{\hat{I}_o}{2} + k_2 I_o \sin(\omega_{com} t)$$

$$i_{l,a} = - k_1 \frac{\hat{I}_o}{2} + k_2 I_o \sin(\omega_{com} t)$$

(5.74)

The simple way to solve this problem could be to induce common mode sine wave current in the arms in such a way that the arm currents in (5.74) become equal to (5.45). Assuming the induced common mode current has the same frequency as the rated nominal frequency, the ac current will now circulate within the arms whereas the dc current will flow out of the bridge legs into the windings of the machine. By flipping the position of the ac and dc part of the currents in (5.45), it can be observed that the maximum DC output current can be half of the nominal output current to keep the peak of the arm current the same as in the case of rated frequency operation. For example, with $\hat{I}_o = 100A$, $M = 1$ and $\cos \varphi = 1$, the instantaneous upper arm current using (5.45) is $i_u = 50 \sin \omega t + 25 \ A$. Now, at zero speed, when the output current is only dc current, a similar waveform to match the peak of the upper arm current at rated frequency operation could be achieved by common mode sinusoidal current injection as in (5.74) and can be made as: $i_u = 25 + 50 \sin \omega_{com} t \ A$. In the latter equation, $25 \ A$ is the maximum dc current from each arm. Hence, a total of $50 \ A$ from a bridge leg can be delivered from the converter without exceeding the current rating of the semiconductor devices. Hence, the theoretical limit of the output torque from a half-bridge MMC at zero speed can be a maximum of 50%, if the semiconductor devices are designed for rated speed operation.

A high-frequency sinusoidal current injection in the arm currents was first proposed in [9] and later a square wave harmonic injection method followed in [10]. The amplitude of the common mode current through each arm as presented in [10] is as follows:

$$i_{z,ac,ref} = \frac{1}{V_{com}} \left(\frac{v_{o,ref}^{*2}}{v_{dc}/2} - \frac{v_{dc}}{2} \right) i_o \sin \omega_{com} t + \frac{v_{o,ref}^* i_o}{v_{dc}} - I_{z,dc}$$

(5.75)

The equation can be simplified to:

$$i_{z,ac,ref} = \left(\frac{m_n^2 - 1}{M_{com}} \sin \omega_{com} t + \frac{m_n}{2} \right) i_o - I_{z,dc}$$

(5.76)

where,

$$m_n = M \sin \omega t \qquad \text{and} \qquad M_{com} = \frac{V_{com}}{v_{dc}/2}$$

(5.77)

Substituting (5.76) in (5.39), the upper arm current can be expressed as:

$$i_{a,u} = i_o \left[\frac{(1+m)}{2} + \frac{(m^2 - 1)}{M_{com}} \sin \omega_{com} t \right] \tag{5.78}$$

The total modulation signal excluding the contribution from the CCS control becomes:

$$m = M \sin \omega t + M_{com} \sin \omega_{com} t \tag{5.79}$$

At low speed, as $\omega \to 0$ and $M \to 0$, upper arm current can be rewritten as:

$$i_{a,u} \approx \frac{\hat{I}_o}{2} \left(1 - \frac{2}{M_{com}} \sin \omega_{com} t \right) \tag{5.80}$$

and,

$$m \approx M_{com} \sin \omega_{com} t \tag{5.81}$$

5.5.2.1 Conduction and switching loss in MMC at dc operation

In this section, the equations for average and rms currents to calculate the conduction loss at standstill condition are derived:

$$I_{T1,avg,dc} = \frac{\hat{I}_o}{4\pi} \left[\left(\frac{2}{M_{com}} - M_{com} \right) + \sin \theta_x \right] \cos \theta_x \tag{5.82}$$

$$I_{T2,avg,dc} = \frac{\hat{I}_o}{4\pi} \left[\pi + 2\theta_x - \frac{1}{2} \sin 2\theta_x + \left(\frac{2}{M_{com}} + M_{com} \right) \cos \theta_x \right] \tag{5.83}$$

$$I_{D2,avg,dc} = \frac{\hat{I}_o}{4\pi} \left[\pi - 2\theta_x + \frac{1}{2} \sin 2\theta_x - \left(\frac{2}{M_{com}} + M_{com} \right) \cos \theta_x \right] \tag{5.84}$$

$$
\begin{aligned}
I_{T1,rms,dc}^2 = \frac{\hat{I}_o^2}{16\pi} &\left[\left(\frac{2}{M_{com}^2} - 1 \right) (\pi - 2\theta_x) - 2 \left(\frac{1}{M_{com}} - M_{com} \right) \cos \theta_x \right. \\
&\left. + 2 \left(\frac{1}{M_{com}^2} - 1 \right) \sin 2\theta_x - \frac{2}{3M_{com}} \cos 3\theta_x \right]
\end{aligned}
\tag{5.85}
$$

$$
\begin{aligned}
I_{D1,rms,dc}^2 = \frac{\hat{I}_o^2}{16\pi} &\left[\left(\frac{2}{M_{com}^2} - 1 \right) (\pi + 2\theta_x) + 2 \left(\frac{1}{M_{com}} - M_{com} \right) \cos \theta_x \right. \\
&\left. - 2 \left(\frac{1}{M_{com}^2} - 1 \right) \sin 2\theta_x + \frac{2}{3M_{com}} \cos 3\theta_x \right]
\end{aligned}
\tag{5.86}
$$

$$I_{T2,rms,dc}^2 = \frac{\hat{I}_o^2}{16\pi} \left[\left(\frac{2}{M_{com}^2} + 3 \right) (\pi + 2\theta_x) + 2 \left(\frac{7}{M_{com}} + M_{com} \right) \cos\theta_x \right.$$
$$\left. - 2 \left(\frac{1}{M_{com}^2} + 1 \right) \sin 2\theta_x - \frac{2}{3M_{com}} \cos 3\theta_x \right] \tag{5.87}$$

$$I_{D2,rms,dc}^2 = \frac{\hat{I}_o^2}{16\pi} \left[\left(\frac{2}{M_{com}^2} + 3 \right) (\pi - 2\theta_x) - 2 \left(\frac{7}{M_{com}} + M_{com} \right) \cos\theta_x \right.$$
$$\left. + 2 \left(\frac{1}{M_{com}^2} + 1 \right) \sin 2\theta_x + \frac{2}{3M_{com}} \cos 3\theta_x \right] \tag{5.88}$$

where,

$$\theta_x = \sin^{-1} \left(\frac{M_{com}}{2} \right) \tag{5.89}$$

$$P_{T1sw,dc} = \frac{U_c f_{sw} \hat{I}_o}{8\pi} \left[k_{1T} \left((\pi - 2\theta_x) - \frac{8}{M_{com}} \cos\theta_x \right) \right.$$
$$+ k_{2T} I_o \left((\pi - 2\theta_x) \left(\frac{2}{M_{com}^2} + 1 \right) \right.$$
$$\left. \left. - \frac{8}{M_{com}} \cos\theta_x + \frac{2}{M_{com}^2} \sin 2\theta_x \right) \right] \tag{5.90}$$

$$P_{T2sw,dc} = \frac{U_c f_{sw} \hat{I}_o}{8\pi} \left[k_{1T} \left((\pi + 2\theta_x) + \frac{8}{M_{com}} \cos\theta_x \right) \right.$$
$$+ k_{2T} I_o \left((\pi + 2\theta_x) \left(\frac{2}{M_{com}^2} + 1 \right) \right.$$
$$\left. \left. + \frac{8}{M_{com}} \cos\theta_x - \frac{2}{M_{com}^2} \sin 2\theta_x \right) \right] \tag{5.91}$$

Similar to the case at rated speed operation, the expressions for switching loss in diodes D_1 and D_2 are the same as that for switch T_2 and T_1, respectively.

5.6   Loss analysis of the converter topologies

The conduction and switching losses cause the rise of the junction temperature of the semiconductor devices. The maximum operating temperature sets the limit to the total loss a switch or diode can incur. Therefore, the current through these

Table 5.10: Market Overview of High Voltage and High Current Semiconductor Devices for High-Power Converters [79, 80, 81].

Manufacturer	Device Type	U_{CE} [V]	U_{dc}^* [V]	Ic [A]
Hitachi ABB	IGCT (Presspack)	6500	4000	3800
		4500	2800	6500
		4500	2800	6000
	BIGT (Presspack)	5200	3400	3000
IXYS	IGBT (Presspack)	6500	3600	1890
		4500	2800	3000
Toshiba	IEGT (Presspack)	4500	2700	2100

The variables used in the table are: Maximum collector-emitter voltage of the device at $25\,^\circ C$, U_{CE}; Permanent dc-link voltage, U_{dc}^*; Continuous collector current of the device, I_c. The device acronyms used are: Integrated Gate-Commutated Thyristor, IGCT; Bi-Mode Insulated Gate Transistor, BIGT; Insulated Gate Bipolar Transistor, IGBT; Injection-Enhanced Gate Transistor, IEGT.

devices is also limited such that the total loss is within the limit and the junction temperature of the devices also remains well within the maximum operating temperature.

5.6.1 Available semiconductor devices

There exist many types of semiconductor devices (Thyristors, MOSFETs, IGBTs, IGCTs, and others) in different formats (discrete, modules, presspack, and others). To achieve high-power converters, high voltage and high current devices are preferable. The IGCT devices' performance is close to the physical limit possible using Silicon material; therefore, these semiconductor devices could be the best candidate for high-power converters based on Si material [60]. In the future, high-performance SiC devices might overcome and a smaller converter could be possible and a filter at the output can be used to deal with high dv/dt. The semiconductor devices available in the market at the moment with the highest voltage and current ratings to achieve a high-power converter of around 100 MVA are presented in Table 5.10.

The semiconductor devices with higher voltage ratings are not available with higher currents (e.g., 6500 V IGBTs) or with matching high current diodes (e.g. 6500 V IGCTs) and thus, these are not ideal selections to meet both high voltage and high power requirements. Therefore, IGCT 5SHY 65L4521 from Hitachi ABB with 4500 V and 6500 A and the corresponding diode FRD 5SDF 28L4520 have been considered for further evaluation.

Table 5.11: Key Electrical Parameters of IGCT (ABB 5SHY 45L4520) and Diode (ABB FRD 5SDF 28L4520) at $125°C$ [79].

Parameters	Values
On-state Knee Voltage of IGCT (U_{CE0})	1.84 V
On-state Resistance of IGCT ($R_{CE,on}$)	0.73 $m\Omega$
On-state Knee Voltage of Diode (U_{F0})	2.036 V
On-state Resistance of Diode (R_d)	0.33 $m\Omega$

5.6.2   Loss in NPC and ANPC converters

The total loss in each semiconductor device of the NPC and ANPC converters is calculated at rated speed operation and zero speed operation using the analytical equations derived in Section 5.3–5.5. The total loss in each device in a converter is the sum of the average conduction loss and average switching loss in that device over one fundamental cycle.

For the analysis of losses in both NPC and ANPC converters, the IGCT from ABB (5SHY 45L4520) in Table 5.10 and the corresponding diode (FRD 5SDF 28L4520) are selected. The IGCTs have relatively lower switching loss compared to IGBTs for high voltage and high current semiconductor devices, therefore, the former is favored for this analysis. The key electrical parameters of the selected switch and diode for loss analysis are presented in Table 5.11. The switching frequency (f_{sw}) is chosen as 250 Hz and dc-link voltage (U_{dc}) is selected as 5.6 kV such that the $\frac{U_{dc}}{2U_{dc}^*}$ ratio is 1. The analysis is done assuming the same type of switches and diodes at each position in the converters.

5.6.2.1   Rated speed operation

In a full-size converter-fed synchronous machine, the rated operation of the converter is when the machine is running at rated speed and at rated load. Since the exciter current in a synchronous machine is controlled by a separate converter, the machine can always run at unity power factor, i.e., at $cos\varphi = 1$ in turbine mode and at $cos\varphi = -1$ in pump mode.

Considering these operating points of the machine, the conduction and switching losses in each IGCT and diode at different positions in a bridge leg of NPC and ANPC have been calculated. The analytically calculated losses of the semiconductor devices are presented in Fig. 5.10. The figure shows that the diode D_5 incurs a loss of 4.4 kW, the maximum loss in the NPC converter. Therefore, it is considered

a reference component for other diodes as well. The loss in the same diode in the ANPC converter is almost half because the current through this diode is shared by the switch T_5.
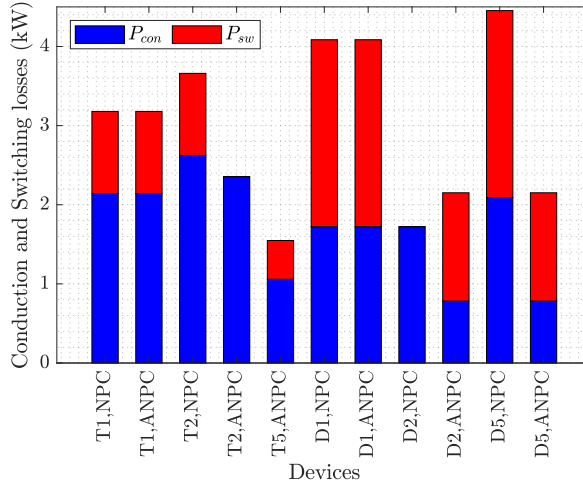
Figure 5.10: Worst-case losses in each device of NPC and ANPC converters at $\hat{I}_o = 3000A$, $f_n = 50Hz$ and switching frequency (f_{sw}) = 250 Hz. The devices used are ABB IGCT 5SHY 45L4520 and ABB FRD 5SDF 28L4520. The legends used are Conduction loss, P_{con} and Switching loss, P_{sw}. The total loss in the device D_5 in the NPC converter and D_1 in the ANPC converter are the highest and are considered as reference devices for the respective converters while dimensioning the devices.

5.6.2.2 Zero speed operation

All semiconductor devices in the NPC and ANPC converters have either maximum conduction loss or maximum switching loss or both at zero speed. The devices stressed by both types of losses decide the current limit a converter can provide at the start-up of the machine. The total loss in the devices increases by a large margin at dc operation. The worst-case losses in devices at each position of both NPC and ANPC converters at zero speed are calculated using the analytical equations and are presented in Fig. 5.11.

At 60% of $\hat{I}_o$, the total loss in diode D_5 of the ANPC converter is similar to the total loss at the rated frequency in the reference device D_1 as shown in Fig. 5.12. The remaining devices have losses well below the reference devices. However, the total loss in the devices T_2 and D_5 of the NPC converter are still higher than the reference value. It means in the case of the NPC converter, the dc current should be reduced further to keep the losses within the limit. The total loss in all the devices in the NPC converter is within the limit when the dc current is about 33% of full load current at rated speed.

Figure 5.11: Worst-case losses in each device of NPC and ANPC converters at $\hat{I}_o = 3000A$, $f_n = 0\ Hz$, and switching frequency (f_{sw}) = 250 Hz. The current comes out of the converter bridge leg to run the machine as a motor (in this application, the scenario is starting the machine in pumping mode). The devices D_1 and D_2 in the NPC case and D_1, D_2, and T_5 in the ANPC case do not conduct for positive dc current, and therefore, the loss is zero for these devices. The devices used are ABB IGCT 5SHY 45L4520 and ABB FRD 5SDF 28L4520.
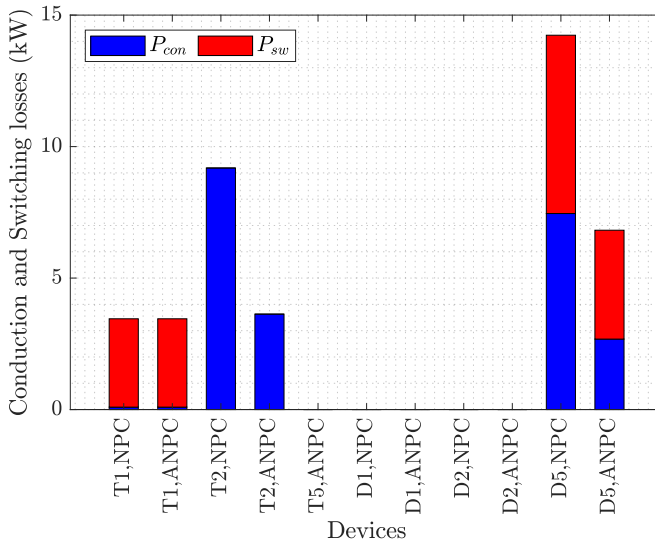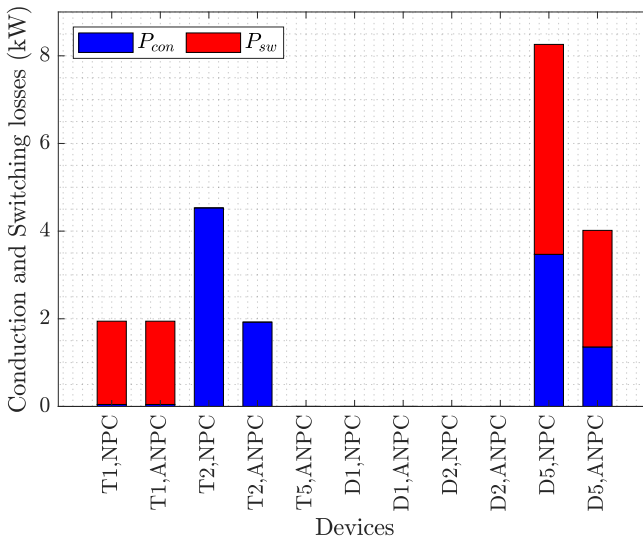

Figure 5.12: Worst-case losses in each device of NPC and ANPC converters at $\hat{I}_o = 1800A$, $f_n = 0\ Hz$, and switching frequency (f_{sw}) = 250 Hz. The current comes out of the converter bridge leg to run the machine as a motor. The devices used are ABB IGCT 5SHY 45L4520 and ABB FRD 5SDF 28L4520.

From this analysis, it is confirmed that the NPC converter can withstand only 33% of full load current at zero speed whereas the same value approaches around 60% in the case of the ANPC converter with the selected devices. Thus, ANPC becomes the preferable choice for an application where high starting torque is required. This torque at zero speed can further increase if the switching loss in the devices is lower or the devices are stressed to their maximum thermal limit.

5.6.3 Losses in modular multilevel converter

The loss analysis of the MMC is carried out with the same semiconductor devices used in the NPC and ANPC converters. The analytical equations derived in previous sections are used to calculate the losses in each device of the submodule. The machine-side converter in a back-to-back converter system will always be operated at unity power factor ($\cos \varphi = 1$) in order to achieve the smallest possible size of the converter, as is the case in a converter-fed synchronous machine.

For the loss analysis in the semiconductor devices of the MMC, the IGCT 5SHY 65L4521, 2800 V, 6500 A from Hitachi ABB and the matching diode FRD 5SDF 28L4520 are selected. The IGBTs have higher switching loss compared to IGCTs at the same switching frequency, and therefore, are not favored for this analysis. The key electrical parameters of the selected switch and diode for loss analysis are presented in Table 5.12. The switching frequency (f_{sw}) is chosen as 250 Hz to have good control of the arm current and to incur less switching loss. The analysis is done assuming the same type of switches and diodes at each position in the converters.

Table 5.12: Key Electrical Parameters of IGCT 5SHY 65L4521 and Diode FRD 5SDF 28L4520 at $140°C$ [79].

Parameters	Values
On-state Knee Voltage of IGCT (U_{CE0})	1.11 V
On-state Resistance of IGCT ($R_{CE,on}$)	0.297 $m\Omega$
On-state Knee Voltage of Diode (U_{F0})	1.10 V
On-state Resistance of Diode (R_d)	0.47 $m\Omega$

The switching loss coefficients of the selected IGCT and diode have been calculated using the curve fitting technique as expressed in (5.17) and presented in Table 5.13.

The stack of the semiconductor devices is assumed to have the double side cooled with $5\ l/min$ water (with 50 % Glycol), which gives the parameters of the thermal circuit as shown in Table 5.14 [82].

Table 5.13: Switching loss curve fitting coefficients of the selected IGCT and diode at $140°C$.

Parameters	Values
k_{1T}	$4.7 \times 10^{-3}\ J/A$
k_{2T}	$3.17 \times 10^{-7}\ J/A^2$
k_{1D}	$1.303 \times 10^{-2}\ J/A$
k_{2D}	$-1.33 \times 10^{-6}\ J/A^2$

Table 5.14: Thermal resistance of different sections of the cooling circuit with double side cold plates [82].

Parameters	Values
$T_{ambient}$	$40\ °C$
$R_{th,j-c}$	$6.8\ °K/kW$
$R_{th,c-h}$	$2.2\ °K/kW$
$R_{th,h-w}$	$5.5\ °K/kW$

5.6.3.1   Rated speed operation

The total loss at rated frequency and unity power factor is calculated for each semiconductor device in a submodule using the expressions (5.52)–(5.67) and is presented in Fig. 5.13. The IGCT 5SHY 65L4521 positioned as T_2 incurs the maximum loss and the switching devices must be rated as per the rating of this device. At a peak output current of $\hat{I}_o = 5.5\ kA$, the conduction and switching losses in the IGCT T_2 are $2.944\ kW$ and $2.392\ kW$, respectively. The total loss of $5.336\ kW$ in the device with the double side cooling arrangement as in Table 5.14 can raise the steady state junction temperature up to $117°C$, which is well within the maximum operating temperature of the device ($140°C$).

5.6.3.2   Zero speed operation

A similar loss analysis as in the case of rated speed operation is carried out for the zero-speed operation. The modulation index of the sinusoidal common mode injection signal has been chosen as $M_{com} = 0.5$ because the study in [10] demonstrates that a similar value gives a submodule voltage ripple of less than 20% in the low and zero speed region. The total loss in each device in a submodule has been calculated using (5.82)–(5.91). The iterative loss calculation with various dc output currents from the bridge leg shows that the loss with 35% of peak current at rated operation ($\hat{I}_o$) yields the same loss as in the case of rated speed operation.
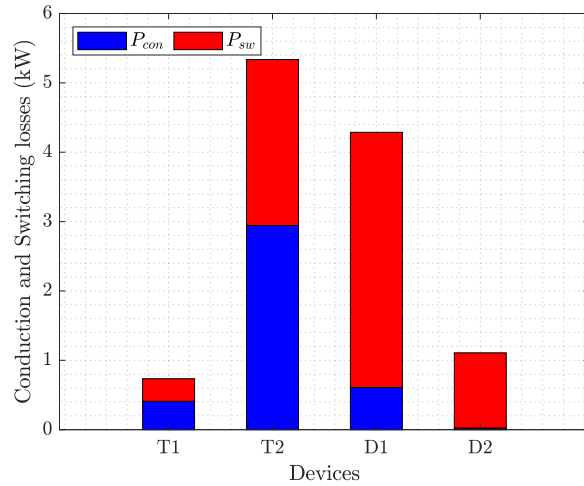
Figure 5.13: Conduction and switching loss in the semiconductor devices of a submodule at rated frequency output and $\hat{I}_o = 5500\ A$.

The loss at $\hat{I}_o = 0.35 I_{o,ratedSpeed} = 0.35 \cdot 5500A = 1925\ A$ is presented in Fig. 5.14.

This analysis shows that the MMC with half-bridge submodules can yield about 35% of rated torque at zero speed or standstill, which satisfies the startup requirement of the reversible pump turbine with water in the runner housing.
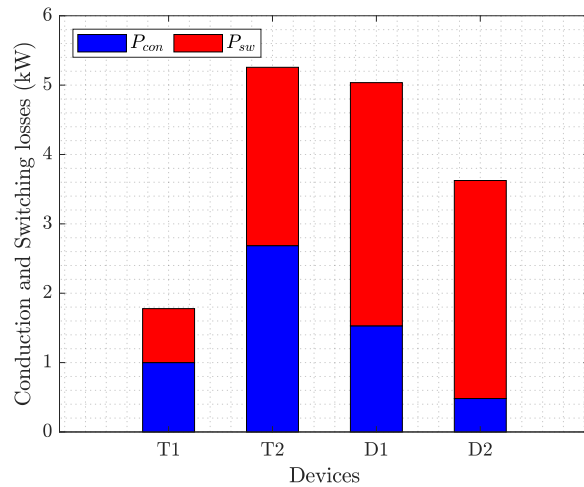
Figure 5.14: Conduction and switching loss in the semiconductor devices of a submodule at zero frequency output and $\hat{I}_o = 0.35 \cdot I_{o,ratedSpeed} = 1925\ A$.

5.7   Evaluation and comparison of converter topologies

The selected three converter topologies: an NPC converter, an ANPC converter, and an MMC have already been evaluated for the startup torque they can produce. Further to this, these converters are evaluated for the PSHP application based on the flexibility they can provide for fast transition from generation and pump mode, the number of semiconductor components and silicon area, requirements of passive components including dv/dt filter, and the efficiency of the converters. The basis of evaluation is followed as proposed in [83].

5.7.1   Converter configuration for transformerless connection

One of the major requirements of a full-size converter for PSHPs is a transformer-less connection to the machine and the grid-side transformer. In other words, only the converter should be placed between the generator transformer (the transformer that connects the machine to the grid) and the synchronous machine.

As the semiconductor devices are rated for their blocking voltage, it is necessary to determine the dc-link voltage of the converter according to the ac voltage output, which is in the range of 13–15 kV for a synchronous machine of 100 MVA. The relation between the ac output voltage and the dc-link voltage in a PWM modulated converter is as in (5.92) [84]:

$$U_{ll,peak} = \frac{\sqrt{3}}{2} M \cdot U_{dc} \tag{5.92}$$

where $U_{ll,peak}$ is the peak value of phase-to-phase ac output voltage, U_{dc} is the pole-to-pole dc-link voltage, and M is the peak value of sinusoidal modulation index. With the space vector PWM modulation or the sinusoidal PWM with third harmonics injection technique, the modulation index can be increased to $\frac{2}{\sqrt{3}}$ ($\approx$ 1.1547) to achieve the maximum output voltage for the same dc-link voltage. In this case, the output voltage and dc-link voltage can be related as:

$$U_{ll,peak} = U_{dc} \tag{5.93}$$

From (5.93), the dc-link voltage required for a 15 kV (rms) output is 21.2 kV. Normally, a margin of 4% is required to determine the dc-link voltage of the converters to drive the current through the machine at the peak of the output voltage [85]. This gives a required dc-link voltage of 22 kV. The selected devices, IGCT 5SHY 65L4521 and Diode FRD 5SDF 28L4520, have a voltage rating of 4500 V, a permanent dc-link voltage (U_{dc}^*) rating of 2800 V, and a current rating of 6500 A. Therefore, with the permanent dc-link voltage (U_{dc}^*) rating of the selected device is 2800 V, at least four IGCTs need to be connected in series at each position of the

Table 5.15: Number of semiconductor devices per bridge leg for NPC, ANPC, and MMC topologies for 15 kV rms output voltage.

Converter topology	Diodes	IGCTs	Remarks
NPC	30	20	
ANPC	30	30	
MMC	36	36	see note below

The number of semiconductor devices must be multiplied by three for a three-phase system to get the total number of devices in the converters. In the case of MMC, 2N, i.e., 18 additional thyristors (one across each submodule) are required to protect the converter against the dc-link short circuit case.

NPC and ANPC converter configuration shown in Fig. 5.1 and Fig. 5.5 to block the half of the dc-link voltage. A dv/dt filter can also be required to filter the sharp and large voltage steps to protect the stator winding insulation.

In the case of MMC, considering a maximum voltage ripple of 10% on the submodule capacitor in a low-speed region, the required dc-link voltage is 23.5 kV. The required number of submodules (N) will then be eight in each arm of three phases with the selected IGCTs. As a general rule of reliability, one extra submodule is added and this will lead to nine in each arm, i.e. 18 submodules per bridge leg.

5.7.2 Semiconductor devices

The dc-link voltage required for transformerless connection is the basis for the number of semiconductor devices to be connected in series. One additional set of IGCT and diode is added in series for redundancy. This leads to 5 IGCTs and 5 diodes at each position of the NPC and ANPC converters. In an MMC, one submodule constitutes of two IGCTs, two diodes, and one additional IGCT to bypass the module during fault conditions. Similar to the case of NPC and ANPC converters, one additional submodule is added to each arm for redundancy purposes. The number of semiconductor devices required in each bridge leg of these converters is summarized in Table 5.15.

5.7.3 Power loss and junction temperature

The power loss analysis based on analytical loss equations is carried out for NPC and ANPC in [8] shows that for a junction temperature of $120°C$, both of these converters can deliver an output current of 4000 A (peak) with IGCT 5SHY 65L4521 and Diode FRD 5SDF 28L4520. A similar analysis for MMC presented in [86]

reveals that MMC bridge legs can deliver up to 5500 A (peak). This corresponds to an output power capacity of 73 MVA for three-level converters compared to 100 MVA for MMC at a voltage output of 15 kV and at a rated frequency.

5.7.4   Device per kW

Since all three topologies are compared for high-power applications, the same type of semiconductor devices are considered for comparison. Hence, the device per kW indirectly provides the Silicon chip area used per kW in the converters. According to Table 5.15, the total number of semiconductor devices used for the NPC converter is 50 per bridge leg (i.e., 150 in total) and the power output is 73 MVA. Hence, the device per kW for this converter is 2.06 device/MVA (0.49 MVA/device). The same value for the ANPC converter is 2.47 device/MVA (0.41 MVA/device), which is about 20% higher than that of the NPC converter. The similar merit for MMC is 2.16 device/MVA (0.47 MVA/device), only 4.8% higher than that of the NPC converter if the thyristor for protection circuit is not considered (2.70 device/MVA including the protection thyristors).

5.7.5   Harmonics in output

The multiple steps of voltage in an MMC make it produce significantly less THD in the output voltage compared to the other alternatives considered for this application. The shape of the output voltage of an MMC is close to sinusoidal and can be connected directly to the grid side or machine side without a passive filter. Looking into the shape of the output voltages from an MMC, NPC, and ANPC, it is obvious that the MMC has the least THD in its output. The voltage level of the MMC can also be chosen freely by adapting the number of submodules close to the rated voltage of the machine.

5.7.6   Startup torque

A typical torque-speed characteristic of an RPT is shown in Fig. 2.4. The startup torque (torque at zero speed) in pump mode is about 12% with the turbine submerged in water.

An ANPC converter can yield relatively high torque compared to MMC topology. In [8], it is stated that the ANPC converter can provide up to 60% torque at zero speed. Further, according to [10], MMC can provide up to 40% if startup torque and the submodule capacitor voltages of the MMC can be kept within the limit by injecting square wave common mode voltage and a circulating current in each leg. Furthermore, an analysis based on power loss in the converter using the analytical loss equations demonstrates that the MMC with IGCTs and corresponding diodes can yield only up to 35% of torque at the startup of the machine [86].

5.7.7   Fast transition from generation to pump mode

The fast transition from generation to pump mode or vice versa is important if the power plant is supposed to regulate intermittent power generation from other renewable sources like wind and solar in a wide range during its operation. The transition from pump mode to generation mode is relatively easy as the water is flowing against the gravity in pump mode. Therefore, it takes a shorter time to switch the mode from pump to generation in existing power plants than to switch the mode from generation to pump mode. From Fig. 2.4, it can be observed that the torque requirement exceeds the torque in the normal operating region around zero speed with a maximum opening of the guide vanes. The converters rated for the normal operating region cannot provide such torque. The converters need to be oversized to meet such requirements. As mentioned in [87, 88, 89], direct MMC with full-bridge submodules can be an alternative if fast transition at the full opening is demanded by the system integration. This solution employs a larger number of semiconductor devices, and consequently, will be a costlier solution.

5.7.8   Passive components

The passive elements in MMC are arm inductors and submodule capacitors. In three-level converters, the dc-link capacitor is a series and parallel connection of several low-voltage capacitors and the same can be imported to the MMC topology. The benefit of the application in MMC is that it does not have the risk of bearing uneven voltage sharing among the capacitors if the capacitance in the series stacks differ by a small margin.

The size of the capacitor in MMC and three-level are quite different. In the three-level, only the ripple current flows through the dc link capacitor, whereas, in the case of MMC, the load current itself is modulated through the submodule capacitor. Therefore, MMC employs relatively larger capacitors compared to NPC and ANPC converters. In MMC, the normalized energy storage requirement is around 25 kJ/MVA [90].

5.7.9   Output (dv/dt or sine) filter

Three-level converters produce output voltage in steps of ($U_{dc}/2$) and lead to a significant amount of harmonics (THD is 16.86%) in the output voltage [91]. MMC has very small steps in the output voltage (U_{dc}/N) and is quite close to the sinusoidal voltage. Therefore, the output filter can be avoided or a very small dv/dt filter can fulfill the cable reflection associated requirement in the case of MMC.

The relatively high voltage step in three-level converters requires a conditioning filter at the output. In the case of retrofit projects, particularly, the space for the

new converter for the synchronous machine may not be available just beside the machine and a cable of 50–60 m may connect the two. Such a long cable with fast switching devices can lead to voltage doubling at the machine terminals due to reflection in the cable and a dv/dt filter may be required at the output of the converter. In addition, the losses in the damper bars of the synchronous machine due to high-order harmonics must also be considered. In some cases, this may lead to the requirement of a sine wave filter at the converter output terminals.

5.7.10 EMI related issues

The three-level converters produce output voltage in only two steps whereas MMC outputs the same in multiple steps (equal to a number of submodules). Therefore, NPC and ANPC will have the common-mode voltage with lower order harmonics components compared to that in the case of MMC. Hence, the conducted electromagnetic interference (EMI) issue is more prominent in NPC and ANPC converters compared to the MMC counterpart. Consequently, the size of the EMI filter is smaller in the case of MMC than for the NPC/ANPC converters. At present, the large-size converters of 100 MVA for pumped storage applications are viable only using IGCTs, which can switch at a relatively very low switching frequency (less than 500 Hz). The dv/dt of IGCTs during turn-off is about $1 \; V/ns$. Wide bandgap semiconductor devices like SiC MOSFETs can switch tens of times faster than IGCTs. Therefore, the EMI issue is going to be a relatively more pronounced problem in the converters with new devices and EMI filters can become an integral part of the converter.

5.7.11 Control related issues

An ANPC converter can be controlled at zero frequency the same way as it is controlled at rated frequency. MMC needs a special control algorithm to inject high-frequency common mode current in the arms in the low-frequency operating region to control the submodule capacitor voltage within the limit. This requires, for example, a common mode current injection of frequency around 45 Hz for a rated system of 50 Hz when operated below 15 Hz [10]. The higher the frequency of common mode voltage, the better the control of the capacitor voltage but this will lead to higher switching frequency and consequently, higher losses in the semiconductor devices.

Since the switching frequency needs to be very high in the case of MMC to have control in the low-speed region, it may not be advantageous to employ MMC in high-power applications using IGCTs. It can be considered as a topology for the future when switching devices with low switching loss will be available in high voltage and high current ratings.

Table 5.16: Average and RMS current through semiconductor devices of NPC converter at dc operation (at the start-up of the machine).

Converter topology	Startup torque	No. of devices	device /MVA	dv/dt filter	Harmonics
NPC	33 %	150	2.06	required	high
ANPC	60 %	180	2.47	required	high
MMC	35 %	270	2.70	can be avoided	low

5.7.12 Efficiency

Since the average and rms current through the semiconductor devices of MMC is relatively smaller than in the case of other topologies, conduction loss in the MMC devices is significantly lower. The MMC yields higher efficiency than 3-level converters and reaches above 99%.

5.8 Summary of comparison

The quantitative and qualitative characteristics of converters enlisted in Section 5.7 are summarized in Table 5.16. The summary table suggests that all three converters meet the application-associated requirements of Section 5.1, except ANPC has the advantage of producing high startup torque compared to the others.

5.9 Selection of converter

The selection of a machine-side converter will be based on the comparison carried out in the previous section. The grid side converter can be selected based on the special case $f_n = 50\ Hz$ analysis. The converters can be of the same type or a hybrid type.

Three possible converter solutions for executing the variable speed operation of a pumped storage plant with synchronous machines are presented. All three converters can achieve an output voltage of 13–15 kV (rms) with the available semiconductor devices for transformerless connection to the machine and the generator transformer. The comparisons show that all can meet the requirement of startup torque of 12% for a fast startup with water in the turbine casing. However, ANPC is the best solution if a fast transition from generation mode to pump mode is required because it can provide up to 60% torque at zero speed in contrast to 33% and 35% from NPC and MMC, respectively. Therefore, a controlled transition with

the partial flow can be executed. Yet, MMC can yield a converter size of higher power capacity close to 100 MW, whereas ANPC can yield up to 75 MW without paralleling the multiple IGCTs. In addition, MMC can be the solution without a dv/dt filter at the output or with a relatively small filter, if needed, compared to the ANPC converter. Additionally, unlike three-level converters, MMC needs a special control strategy of high-frequency common mode injection to operate at lower frequencies, which demands a higher switching frequency operation to control the common mode current. Therefore, MMC with half-bridge submodules cannot be the best choice for high-power applications with devices like IGCTs.

Having examined all the attributes of these converters, it is evident the ANPC converter can serve the specification the best with startup and fast transition of modes. Hence, it can be regarded as a possible alternative for variable speed operation of a pumped storage plant with a full-size converter using the available semiconductor devices.

Chapter 6

Control of Active Front End Converter

*In this chapter, the topology of the grid-side converter and its control are discussed. This converter operates at an almost constant frequency and supports the grid with reactive power. The virtual inertia control of the Active Front End and its impact on the size of the converter are also presented. The chapter briefly describes a few important features that the grid-side converter must incorporate. The chapter addresses, in part, the **Research question 1** and **Research question 2**. Since this topic is not the main scope of this research, the control of the grid-side converter in the context of PSHP is discussed only briefly.*

6.1 Introduction

The grid-side converter, also known as the active front end (AFE) converter in drive applications, serves as the gateway for power flow into the grid. Chapter 7 describes the control mode of this converter during turbine and pump operation. In a synchronous machine powered by a full-size converter, the AFE plays a crucial role in regulating reactive power and providing virtual inertia.

In the context of a converter-fed synchronous machine, the inertia of the machine is decoupled from the grid. However, this decoupling allows for the added advantage that the speed of the machine can be allowed to deviate because it is not directly connected to the grid. The rapid control capabilities of the converter enable the transfer of energy to and from the inertia of the rotor shaft more quickly compared to a directly connected system. This characteristic significantly enhances grid stability, a concept commonly referred to as virtual inertia or synthetic inertia.

6.2   Converter topology for grid-side

The grid-side converter is connected to the low-voltage side of the generator transformer, which steps up the voltage to the transmission line voltage. Therefore, the output voltage requirement is the same as that for the synchronous machine, i.e., 13–15 kV rms. Generally, the frequency converters are rated for operation at nominal frequency, i.e., at 50 or 60 Hz in a grid-connected operation. As explained in Chapter 5, the total loss in the converter is minimum while operated at rated frequency. Since the frequency of the grid is always stable at a nominal frequency, the grid-side converter can be a three-level NPC converter or MMC that can match the voltage of the synchronous machine.

6.3   Reactive power contribution

In a grid-connected system, the grid-side converter is responsible for the reactive power supply to the grid. The power factor of the grid-side converter operation directly impacts the size of the converter. For example, the semiconductor devices of the converter must be dimensioned for $1.25I_n$ if it is operated at a power factor of 0.8 compared to the unity power factor operation.

In the case of MMC, the output power factor will have a direct impact on the size of the sub-module capacitor. The size increases inversely with the load power factor.

6.4   Virtual inertia contribution

6.4.1   Virtual inertia in turbine mode

The grid-side converter running in a frequency droop control mode (also known as grid forming mode in literature) experiences a step power load whenever there is a decay in frequency. A constant df/dt is equivalent to a constant power step for the converter. Therefore, while connected to the grid, the grid-side converter needs to supply additional power steps in addition to the steady-state power. In a directly grid-connected synchronous machine, the first few seconds of this power come from the inertial energy stored in the rotating shaft of the machine until the governor reacts to supply more water to the turbine. In a converter-fed synchronous machine system, the power step caused due to change in frequency is very quickly transferred to the machine shaft as there is very little energy stored in the dc-link capacitor. However, this inertial energy from the shaft in this case flows through the converter.

In contrast to copper as the winding material in the stator of synchronous machines which can be overloaded for several minutes, the frequency converters constitute very thin semiconductor dies and have a very small thermal time constant (less

than a second). As a result, these converters must be rated to handle both steady-state and inertial power, even though the latter is only needed for a few seconds. This means that if a converter is rated in the same way as a synchronous machine, it won't be able to provide any inertial power while operating at full load. Consequently, if delivering inertial power at full load is necessary, this leads to an increase in the size of the converter.

When the grid-side converter is rated solely for steady-state active power, the contribution of virtual inertia can only be realized at partial load. However, if the desired virtual inertia contribution during operation near full load extends to a range of 2–5 seconds, this would necessitate an additional increase in the current rating of the converter.

6.4.2   Virtual inertia in pump mode

The behavior of the converter control is different in pump mode as the grid-side converter is responsible for the dc-link voltage of the back-to-back converter setup. Any negative change in frequency can be supported by the grid-side converter by immediately releasing the pumping power. This will lead to reduced dc-link voltage, and consequently, reduced speed of rotation of the reversible pump-turbine to reduce the water flow. This case has been experimentally verified in the laboratory and is presented in Chapter 7. However, the opposite phenomenon needs to be handled carefully. Any positive change in grid frequency needs to be compensated by the grid-side converter by consuming a step power. Such step power will raise the dc-link voltage to the maximum limit due to the very small energy storage capacitor at the dc-link. The machine-side converter responds to such increment in frequency by increasing the pump power and hence the increased flow toward upstream. A control method like feed-forward power can be added to the machine in pump mode.

6.5   Shaft inertia of the synchronous machine

The inertia requirement in a conventional hydropower plant depends on the length of the tunnel and penstock (only the latter if there is a surge chamber). If there is a sudden load step on the machine, the inertia of the rotor delivers the energy until the water flow in the penstock increases, and the potential energy of the water gets converted into mechanical energy. The acceleration time the water (T_{wt}) through the penstock is $T_{wt} = \frac{L}{gA} \frac{Q_R}{H_R}$ as presented in Chapter 3. Further, the mechanical time constant (T_m) of the synchronous machine rotor is chosen such that $\frac{T_m}{T_{wt}} > 6$ [92]. This leads to a very high energy storage requirement in the rotor of a hydropower generator.

In a full-size converter-fed PSHP system, although the synchronous machine is physically decoupled from the constant frequency electrical grid, it remains tightly connected electrically due to the very limited energy storage capacity of the dc-link capacitor. Any grid transients are swiftly transferred to the dc-link capacitor through the fast control of the AFE, and subsequently, to the synchronous machine via the machine-side converter.

The findings presented in Chapter 3 indicate that the rotor speed must not deviate by more than 10%, as further reduction can have a detrimental effect on the torque output of the turbine and may lead to instability. Hence, the requirement for rotor shaft inertia based on the ratio $\frac{T_m}{T_{wt}} > 6$ remains valid, even in the case of a full-size converter-fed PSHP. Further research can explore alternative methods of energy storage on the DC-link to assess their potential in reducing the need for such a significant shaft inertia.

6.6 Conclusion

The grid-side converter consistently operates close to the rated output frequency of the converter. Consequently, when sizing the converter, it's crucial to consider the current it needs to provide at the rated frequency of operation and at the rated load. Both the three-level NPC converter and MMC converter meet these criteria. To fulfill its role in providing reactive power and virtual inertia at full-load operation, the grid-side converter should be designed to achieve approximately 120% of the nominal stator rating of the synchronous machine.

Chapter 7

Secondary Control Strategy

*In this chapter, the control methods to start, stop, and transition the mode from the pump operation to the turbine operation and vice versa are presented. In addition, the effect of low voltage ride through on the grid side converter is explained for both pump and turbine modes of operation. The control strategy was verified in a laboratory arrangement with a 100 kVA synchronous machine connected to the grid via a two-level back-to-back converter. The experimental results of operation at the system level and at the inner current control level are depicted with characteristic plots. This chapter addresses the **Research questions 3 and 4**.*

7.1   Introduction

In a pumped storage plant with a full-size converter-fed synchronous machine, the speed of the machine can be varied independently with respect to the grid frequency. This feature gives the advantage of being able to run the turbine at its maximum efficiency point as the head and water flow vary during both turbine and pump operation.

In addition, the synchronous machine can always be controlled at a unity power factor such that the machine will experience the least possible loss at any point of operation. Since the excitation current is also controlled separately by a dc-dc converter, maximum torque per amp control comes to be the same as unity power control, unlike with the permanent magnet synchronous machines.

The flexibility to control the power consumption in pump operation can be controlled dynamically, which proves to be important in stabilizing the grid frequency during disturbances.

In this chapter, all the flexibilities that can be achieved by the installation of a full-size converter in a pumped storage plant are experimentally executed. The following control-related issues in a pumped storage power plant are addressed:

- efficiency optimization control

- start, stop, and mode transition in both pump and turbine operation

- impact of low voltage ride through in pump and turbine operation

7.2   Control method

The innermost control of the converter, which controls the d- and q- axes currents, and the excitation current to produce the required torque were already discussed in Chapter 4. Also, there exist several converter topologies to meet the converter requirements as described in Chapter 5. The system level control, also known as a secondary controller, controls the power to and from the grid and produces optimal speed based on the hydraulic parameters. This control strategy can be developed independently regardless of the converter topology controlling the inner current controllers.

The secondary controller takes all the measured parameters and commands from power plant operators and transmission system operators (TSO) as inputs and pro-
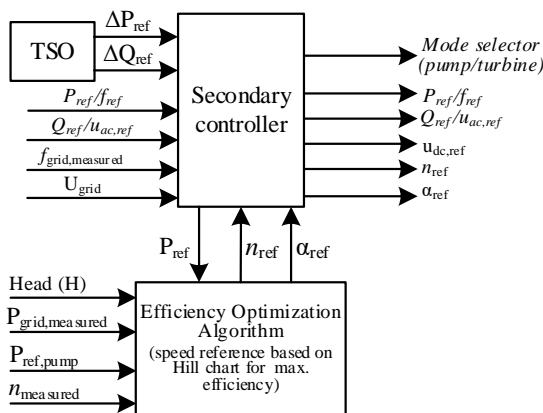
Figure 7.1: Schematic showing secondary layer control strategies for the full-size back-to-back converters. The plant operator normally sets the active and reactive power references (input to the secondary controller). The TSO provides incremental changes dynamically according to the instantaneous grid parameters. The Efficiency Optimization Algorithm processes the net head (H) and power reference (P_{ref}) in both turbine and pump mode and determines the speed of rotation of the RPT. The references produced by the secondary controller are passed to the converter controllers. A set of converter controllers is activated depending on the mode of operation (pump/turbine).

duces the optimal reference speed in both pump and turbine modes. In addition, it also produces the active and reactive power references for the grid side converters as depicted in Fig. 7.1. The efficiency optimization algorithm is considered part of the secondary control layer, which takes hydraulic parameters like head and water flow as inputs in turbine mode to decide the optimal speed of the turbine based on the Hill chart curves for that particular turbine. The Hill chart parameters provided by the turbine manufacturer can be inserted as a look-up table in the system. Similarly, the controller produces the speed reference and the guide vane angle reference in the pump mode based on the power reference (power available by TSO or the plant operator) with which it can pump the water upstream.

The references produced by the secondary controller are passed to the individual converter control system that controls that particular variable as shown in Fig. 7.2. Both the active front end (grid side) and machine side converters control the different variables in pump and turbine modes. In pump mode, the grid side con-
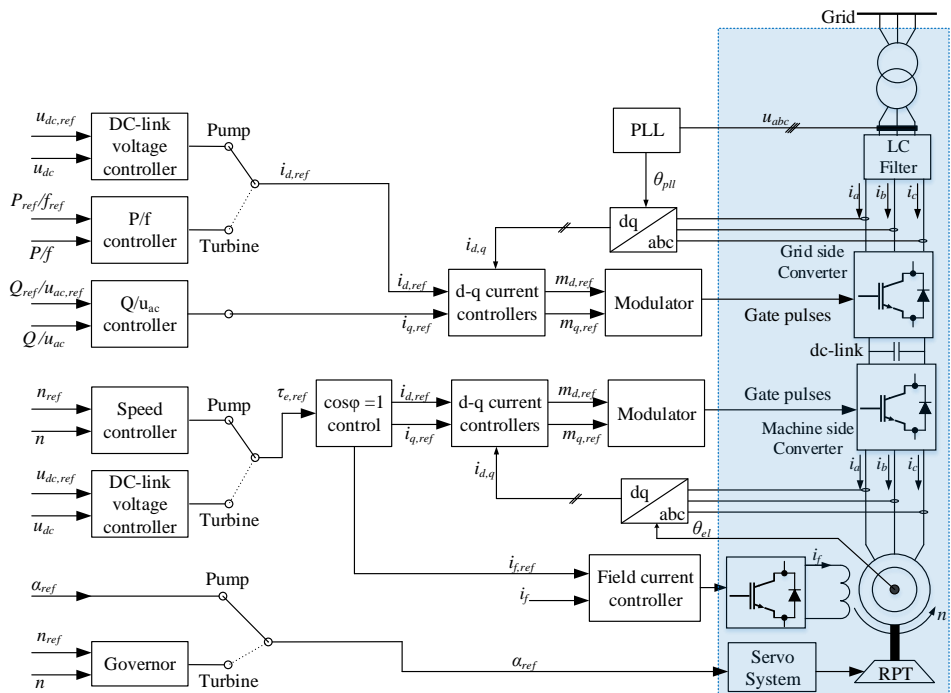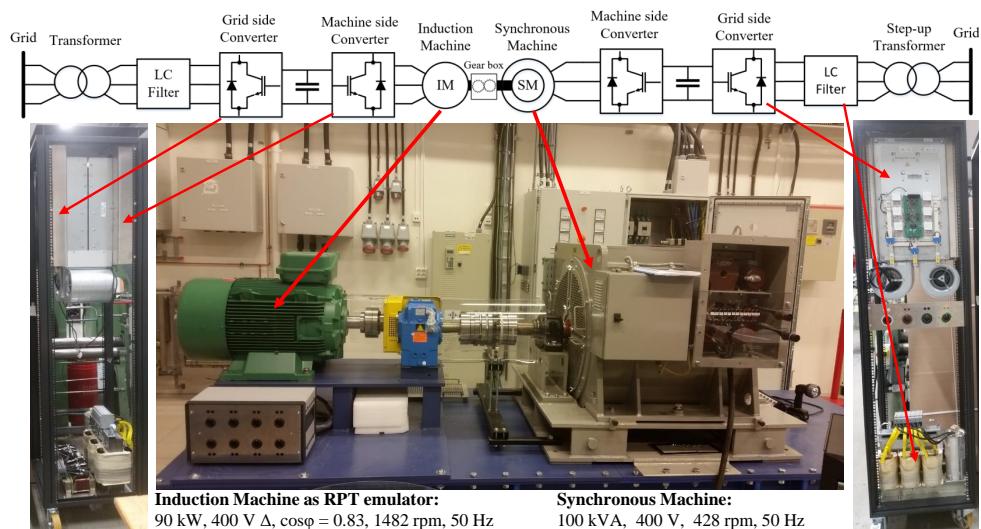

Figure 7.2: Schematic of the overall control of the full-size back-to-back converters. All the references to the controllers (on the left side of the figure) come from the secondary controller and the Efficiency Optimization Algorithm. All the controllers are proportional-integral (PI) controllers. The shaded region consists of the physical components of the power plant.

verter controls the dc-link voltage and the reactive power to the grid, whereas the machine side converter controls the speed of the machine. In turbine mode, the machine side converter controls the dc-link voltage, whereas the grid side converter controls the active and reactive power flow to the grid based on voltage and frequency droop. The governor controls the turbine speed in turbine mode, and therefore, the guide vane opening angle is determined by the governor, itself. The guide vanes are normally kept fully open while running in pump mode. The power and the water flow in pump mode are controlled by adjusting the speed of the machine using the machine-side converter.

7.3   Laboratory setup

There exist various types of converters that can serve the purpose of a full-size converter in a back-to-back converter configuration. The secondary control strategy can be developed such that it is independent of the type of converter installed for the grid-side and machine-side converters. Therefore, to validate the overall system level of control, a two-level back-to-back converter setup has been chosen as the laboratory prototype for this work as shown in Fig. 7.3.

The down-scaled laboratory setup consists of a synchronous machine as in the case of fixed speed PSHPs and a two-level three-phase back-to-back converter set

Induction Machine as RPT emulator:
90 kW, 400 V Δ, cosφ = 0.83, 1482 rpm, 50 Hz

Synchronous Machine:
100 kVA, 400 V, 428 rpm, 50 Hz

Figure 7.3: 100 kVA laboratory prototype. The right half of the gearbox with the synchronous machine (SM) and back-to-back converter is the setup for which the control strategies have been proposed and tested. The left half of the setup with the induction machine (IM) and the back-to-back converter is emulating the reversible pump-turbine as is the case in a PSHP.

to verify the control principles. The field current is controlled by a separate full-bridge dc-dc converter and the field current reference ($i_{f,ref}$) is set to the converter from the SM converter over the CAN bus. Another two-level three-phase back-to-back converter with an induction machine (IM) is connected via a gearbox (left half from the gearbox of Fig.7.3) to emulate the reversible pump-turbine (RPT). The model of the RPT, waterway, governor control, and efficiency optimization algorithm is simulated in a real-time simulator (OPAL-RT with MATLAB Simulink models). The model also serves as the secondary controller as presented in Fig. 7.1. In addition, it initiates the transition of operation mode (turbine to pump or vice versa) and generates references and control mode of operation for the converters. The speed reference in turbine mode and the torque load in pump mode are transferred to the IM converter over a high-speed optical fiber link. The IM drive control is tuned to accurately follow the simulated speed of the RPT model. The overall laboratory setup follows the control structure shown in Fig. 7.1 and 7.2 except for the efficiency optimization part. The main objective is to validate that the control principles work as proposed. The specifications of converters and the electrical machines are presented in Table 7.1.

The power electronic converters connected to the synchronous machine and induction machine, the exciter winding of the synchronous machine, and the grid are controlled by separate control boards, which incorporate embedded system-on-module (SOM) from AVNET PicoZed™ with a custom designed carrier board. The analog-to-digital (AD) converters on the carrier board receive the line current, DC-link voltage, and encoder measurements, which are the essential signals for the control software. The carrier boards also include an optical fiber communication interface, which forms a ring network among the control boards and the OPAL-RT. The SOM on the control boards are loaded with their respective control software for the machine-side and grid-side converters. The control software was developed during this work in C++ programming language.

The electrical power of the synchronous machine is 100 kVA in the available laboratory setup presented in Fig. 7.3. The model of the pumped storage plant and reversible pump-turbine have been modified to match one of the four units of a real power plant of 708 MW (one unit of 177 MW). The mechanical time constant of the emulated model is made 10 seconds as in the case of the real power plant, which is only 1 second in the laboratory setup. The hydraulic parameters used to emulate the pumped storage plant in the laboratory are presented in Table 7.2.

Table 7.1: Specification of electrical equipment of the experimental setup.

Converter specification - grid side	
Rated power	100 kVA
Rated dc-link voltage (U_{dc})	650 V
DC-link capacitor (C_{dc})	1.5 mF
Switching frequency (f_{sw})	4 kHz
Converter side inductor (L_1)	$0.4\ mH$
AC side capacitor (C_{ac})	$27.9\ \mu F \Delta$
Grid side inductor (L_2)	$18\ mH$
Induction machine specification	
Rated power	90 kW
Rated voltage	400 V
Rated current	165 A
Power factor (p.f.)	0.83
Rated speed	1482 rpm
Synchronous machine specification	
Rated power	100 kVA
Rated voltage	400 V
Rated current	144.3 A
Rated speed	428.57 rpm
x_d	1.27 pu
x_q	0.75 pu
x_d'	0.8 pu
x_d''	0.3359 pu
x_q''	0.3176 pu
T_d'	N/A
T_d''	4.6 ms
T_q''	4.27 ms
Rated excitation current (I_f)	56 A

 Note: All the converters are identical. The machine-side converter outputs are directly connected to the machines, whereas those of the grid-side converters are connected to the grid via an L-C-L filter.

Table 7.2: Hydraulic parameters of the scaled hydropower plant.

Power plant parameters	
Rated power (4 units)	708 MW
Rated head (H_0)	425 m
Rated discharge (Q_0)	170 m^3/s
Headrace tunnel	
Length (L_1)	10.65 km
Cross-section area (A_1)	100 m^2
Water time constant (T_{w1})	4.25 s
Penstock parameters	
Length (L_2)	151.2 m
Cross-section area (A_2)	6.16 m^2
Water time constant (T_{w2})	1 s
Turbine parameters	
Maximum discharge ($Q_{r,max}$)	42.5 m^3/s
Rated discharge (Q_r)	38.25 m^3/s
Rated head (H)	425 m
Rated speed (Ω_R)	750 rpm
σ	0.369
ψ	0.418
ξ	1.0
α_{1R}	36°
Frictional coefficient (r_m)	0.05
Mechanical time constant (T_m)	10 s

Note: The turbine parameters σ, ψ, and ξ are geometrical constants of a given turbine. α_{1R} is the opening of the guide vanes at rated discharge. The hydraulic parameters are taken from a real pumped storage power plant. The reversible pump-turbine data is based on the theoretical design and has been verified in another study within the same research project [93].

7.4   Experimental results

The following control strategies with a full-size converter setup have been experimentally verified for the control of the PSHP:

1. Start the machine in turbine mode and load it to steady state load via grid side converter

2. Start the machine in pump mode from a standstill with water in the turbine casing and load it to the steady state value

3. Switch the mode of operation from pump to turbine mode without disconnecting from the grid

4. Switch the mode of operation from the turbine to pump mode without disconnecting from the grid

5. Low voltage ride through in turbine mode

6. Low voltage ride through in pump mode

In electrical terms, the turbine and pump mode can be interchanged with generation mode and motoring mode, respectively. The active power (p) and the current (i_o) out of the converter are assumed positive. Consequently, the active power (p) out of the converter in pump mode is positive and the power into the converter in turbine mode is negative. Moreover, the speed (n) is considered positive in turbine mode, while in pump mode, it is negative (also shown in Fig. 2.4 of Chapter 2). Hence, the electrical torque (τ_e) stays negative in both modes of operation as:

$$ p = n \cdot \tau_e \begin{cases} n > 0, \ \tau_e < 0 & \text{:turbine mode} \\ n < 0, \ \tau_e < 0 & \text{:pump mode} \end{cases} \tag{7.1} $$

The experimental results presented in the later sections follow this sign convention. In addition, the water flow (q) is positive while flowing downwards from the headrace to the tailrace in the turbine mode, and it is negative in the pump mode.

Since the hydraulic components like RPT, waterway, and penstock are modeled in OPAL-RT, the system level variables like water flow (q) and guide vanes opening (α) are recorded in the Simulink model. The converter control variables like the speed of the synchronous machine (n), electrical torque (τ_e), electrical power (p), and dc-link voltage (u_{dc}) are measured using a digital oscilloscope, which records data at each interrupt cycle of the control software. The recorded measurements are plotted using MATLAB and presented in this section. The list of symbols used in the figures is listed in Table 7.3.

Table 7.3: List of symbols used in figures

| Guide vanes opening	α
Water flow through the RPT in per unit	q_{pu}
Speed of the RPT in per unit	n_{pu}
Electrical torque produced by the synchronous machine in per unit	$\tau_{e,pu}$
Electrical power produced by the synchronous machine in per unit	p_{pu}
dc-link capacitor voltage reference	$u_{dc,ref}$
Measured dc-link capacitor voltage	$u_{dc,meas}$

7.4.1 Startup in turbine mode from standstill

The startup process in turbine mode is partly similar to the conventional method where the guide vanes opening is set to a fixed opening optimized for a particular turbine unit (also known as idle position) and allows the machine to accelerate to the nominal speed. The excitation system is then turned on. Since the rated voltage is available at the terminals, the dc-link capacitor is charged to the peak value of ac voltage through diode rectification. The machine-side converter for the synchronous machine is then set to run state (start switching the semiconductor devices) to reach the dc-link voltage reference (which is around 0.9–1.0 pu). With a stable dc-link voltage, the AFE is started and synchronized to the grid. The startup process in turbine mode is presented in Fig. 7.4, and the response of the dc-link voltage controller is presented in Fig. 7.5.

In the experimental setup presented in Fig. 7.3, there is no external pre-charge circuit for the dc-link capacitor on the machine-side converter. As the stator voltage builds up in turbine mode, the dc-link is charged through diodes of the SM side converter. Subsequently, as the converter on the synchronous machine (SM) side begins switching to regulate the dc-link voltage, controller saturation induces voltage oscillation in the dc-link as shown in Fig. 7.5. This is primarily attributed to the fact that the dc-link voltage is already at the peak of the stator voltage, and there is no alternative power source to the dc-link (such as a pre-charge circuit). The dc-link voltage reference is filtered with a first-order low-pass filter. This filter does not affect the dynamic behavior of the system because once the dc-link voltage reaches its set point, it is never changed during its normal operation.
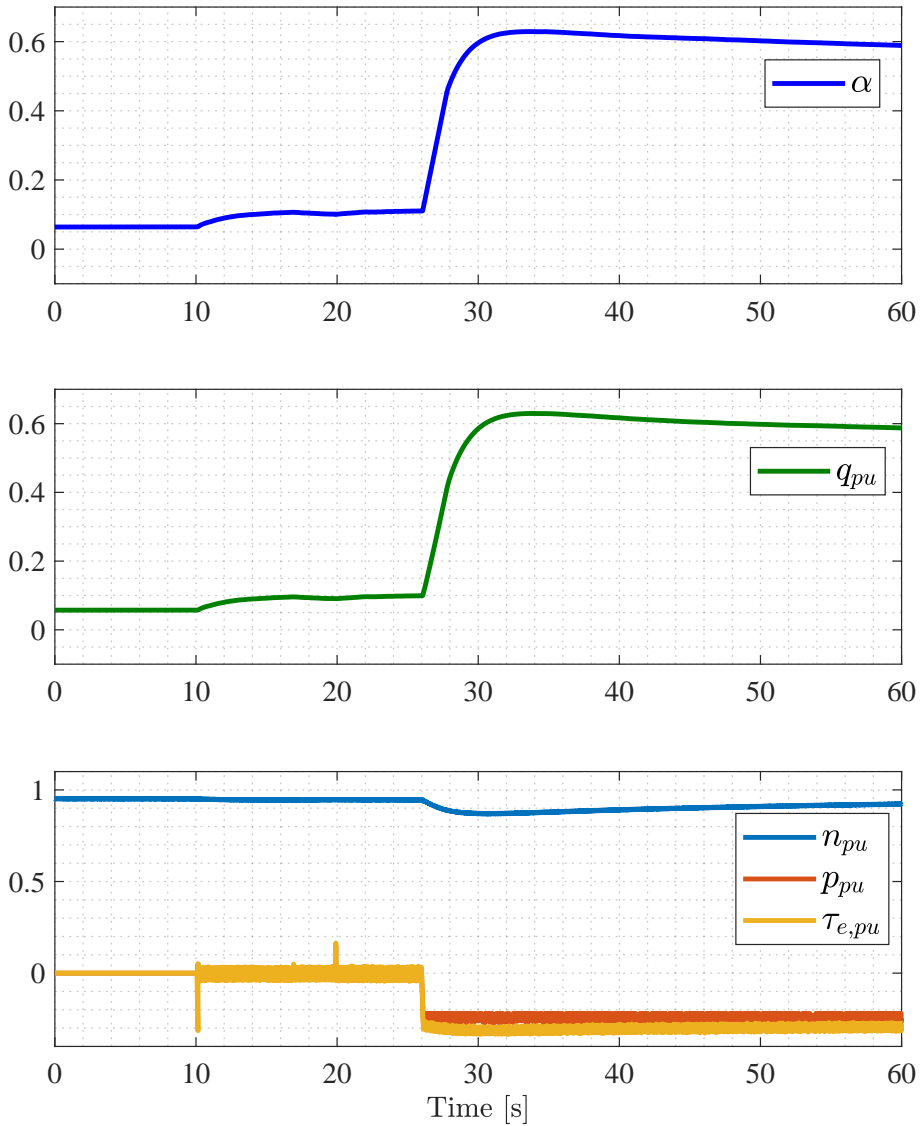
Figure 7.4: Startup in turbine mode from standstill. Prior to $t = 10s$, the turbine governor controls the guide vanes (α) to run the turbine to 1 pu speed as in the case of a traditional fixed speed PSHP. At $t = 10s$, the machine side converter is started and the charging of the dc-link capacitor is the reason for the transient in the torque. The water flow (q_{pu}) increases to cover the losses in the machine and the converter. At $t = 20s$, the grid converter is started and synchronized to the grid. At $t = 26s$, a power output of -0.25 pu is injected into the grid using the grid-side converter. The recovery of speed takes around 60 seconds which is completely acceptable since the grid frequency and turbine speed are decoupled.
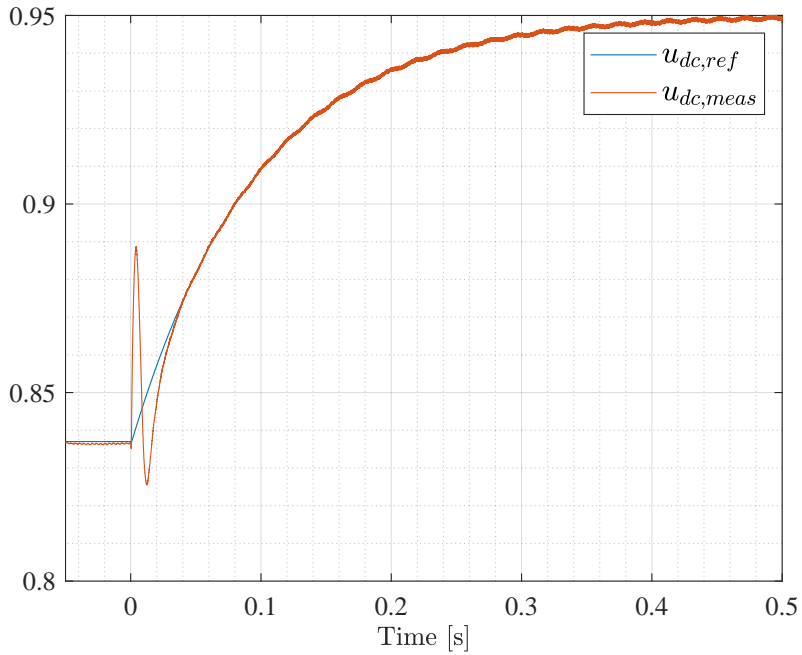
Figure 7.5: Startup of synchronous machine-side (SM) converter in dc-link control. The dc-link voltage is controlled without pre-charge, which is the case during the black start of the power plant. The dc-link voltage before $t = 0s$ is from the diode rectification of the converter. The switching is enabled at $t = 0s$ and the reference voltage (0.95 pu) is passed through a filter. The switching event leads to oscillation in the voltage due to the saturation of the controller, which is difficult to avoid since the dc-link voltage is already at the peak of ac voltage.

7.4.2   Startup in pump mode from standstill

Startup in pump mode from a standstill is the major challenge of state-of-the-art pumped storage hydropower plants. In existing power plants, the water from the turbine casing is depressed below the runner level so that the runner stays in the air. The method requires less torque to accelerate the machine to synchronous speed. There exist several methods to execute this, for example, soft starter, Load Commutated Inverter (LCI), pony motor, auxiliary turbine, using a rotor converter and short-circuiting the stator in a DFIM setup, and some others [46, 94].

The RPT requires a starting torque of around 13% of its nominal torque when submerged in water. In a PSHP with a full-size converter-fed synchronous machine, the AFE is started first in dc-link control. After the dc-link voltage stabilizes to its reference value, the SM machine-side converter is started in speed control mode. The machine setup is accelerated to the rated speed at the desired rate by controlling the ramp time from the secondary controller. As the speed increases, the torque capability of the converters also increases. The speed reaches to steady state value within 5–6 mechanical time constant considering the lower torque capability of the converter in low-speed region. The guide vanes are then opened to pump the water upstream. The speed is adjusted to control the water flow, and consequently, the active power is consumed from the grid as presented in Fig. 7.6.

The results verify that the loading in pump mode is quite sensitive to the change in speed. In this case, the zero torque loading in pump mode is at the speed of -0.93 pu, and the torque loading increases by 0.6 pu when the speed changes by only 0.07 pu.

7.4.3   Transition from the pump to turbine mode

The transition from the pump to turbine mode is fast even in fixed-speed PSHP as the water flows from the headrace to the tailrace once the pumping power is disconnected. Yet in this case, the machine starts to rotate in the opposite direction, and the phase sequence of the grid needs to be altered for re-synchronization in generation mode. This procedure is not required in a full-size converter-fed synchronous machine. The controlled transition in a converter-fed operation has been tested as follows and presented in Fig. 7.7.

The system is running in pump mode with AFE in dc-link control mode and SM drive in the speed control with a speed in the range of -1 to -1.1 pu. When the transition of operation mode is initiated, the speed is decreased to the value where the load torque due to pumping action is minimum, i.e., water flow is zero, and the guide vanes are closed to the minimum level (the opening level used at the start in generation mode) so that the pumping power consumed from the grid is close to
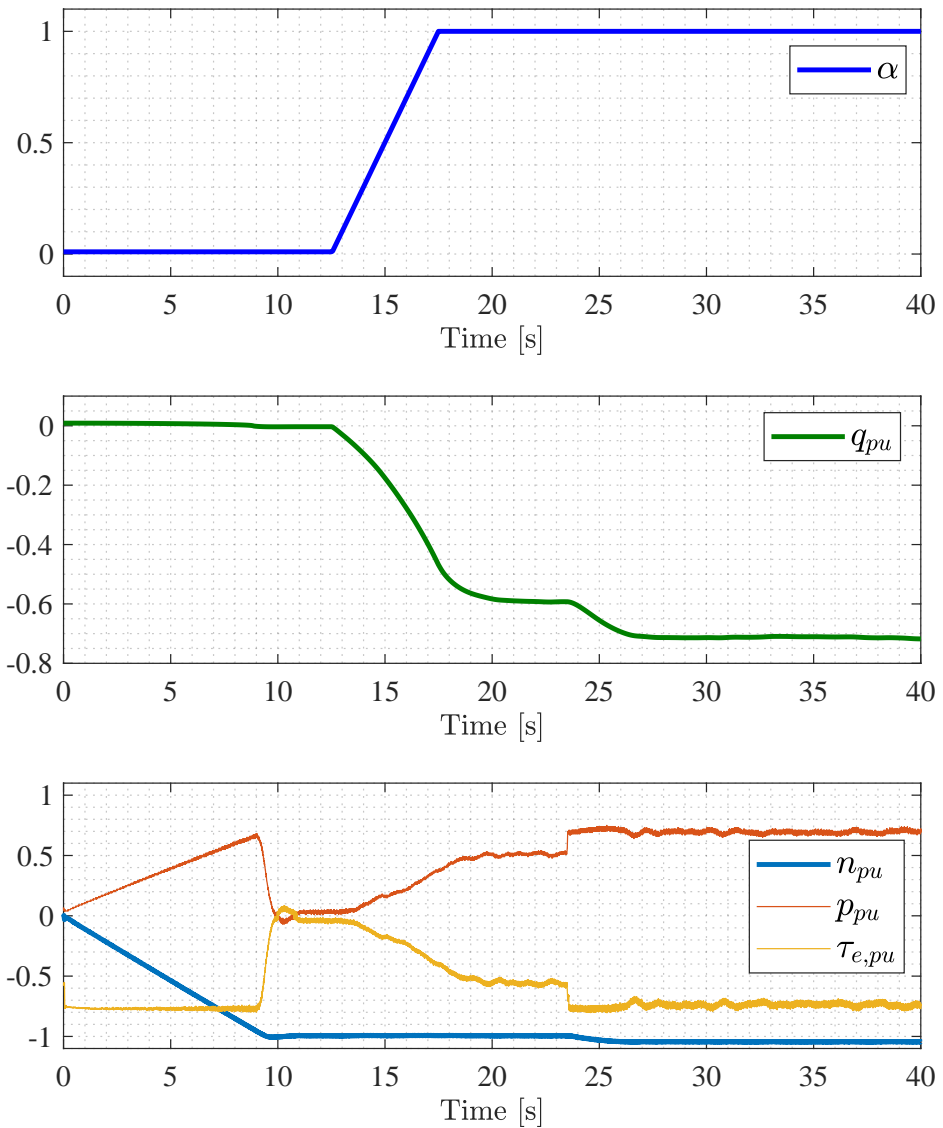
Figure 7.6: Startup in pump mode. From $t = 0s$ to $t = 10s$, the pump speed is accelerated to -1 pu. At $t = 12.5s$, guide vanes have started to open and the torque loading on the SM increases, and consequently, the power consumption increases. The water flow increases to -0.6 pu. At $t = 23.5s$, the speed is further increased to -1.05 pu to increase the water flow, and hence the torque loading and the power on the machine increase. The load changes sharply in this region as expected from the torque-speed characteristics shown in Fig. 2.4. The oscillation in the water flow reflects on the torque and power of the synchronous machine. It takes several minutes for the water to stabilize.
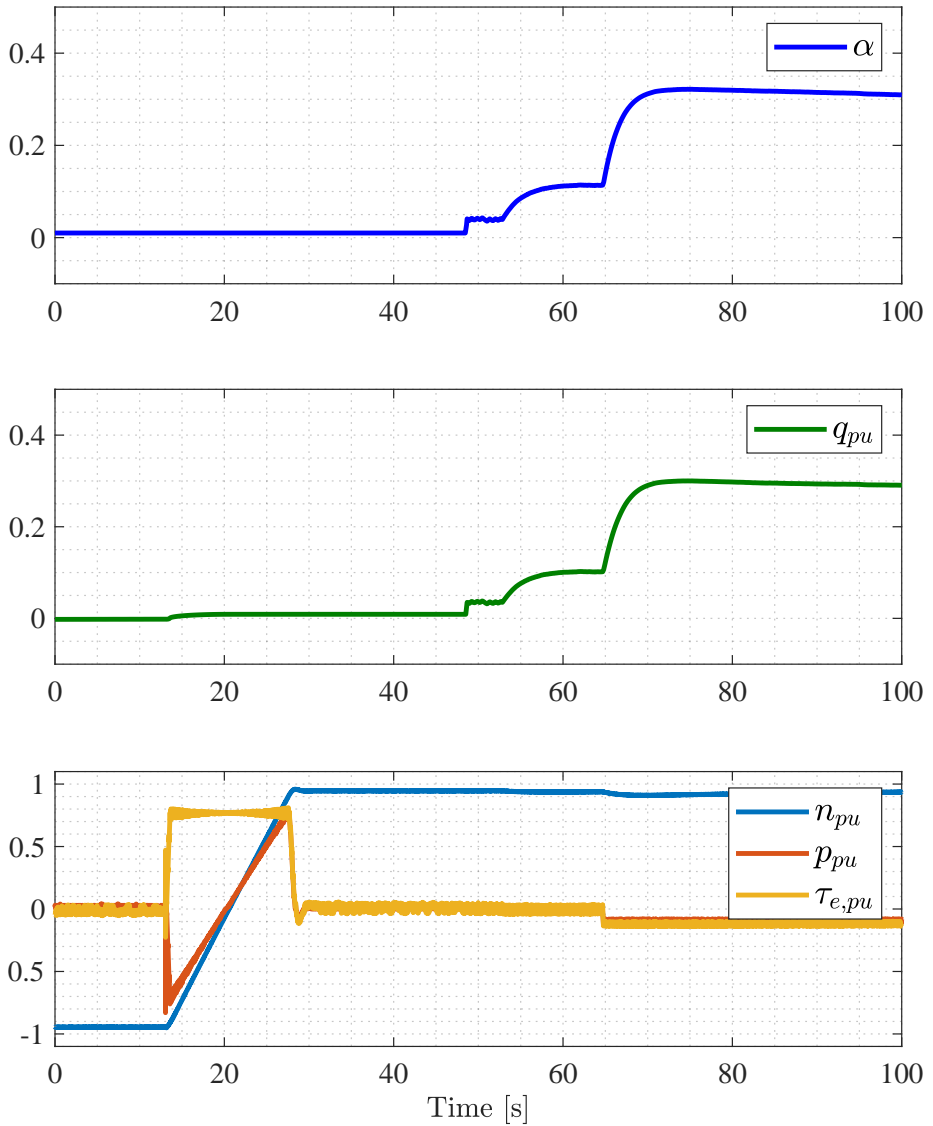
zero. The secondary controller that initiates the mode transition changes the speed reference to 1.0 pu to turn the rotation in the direction of turbine operation. The SM drive ramps the speed in the positive direction to the reference value. Now, the control mode of the converters is changed. The SM drive controls the dc-link voltage and the AFE remains synchronized to the grid but is now controlled as a virtual synchronous machine. The turbine governor is then enabled to control the speed of the machine to the reference value generated by the efficiency optimization algorithm. The power to the grid is now controlled by AFE running in power control mode or in frequency droop to the grid. The further sequence is the turbine mode of operation is the same as explained in the start-up in turbine mode of operation.

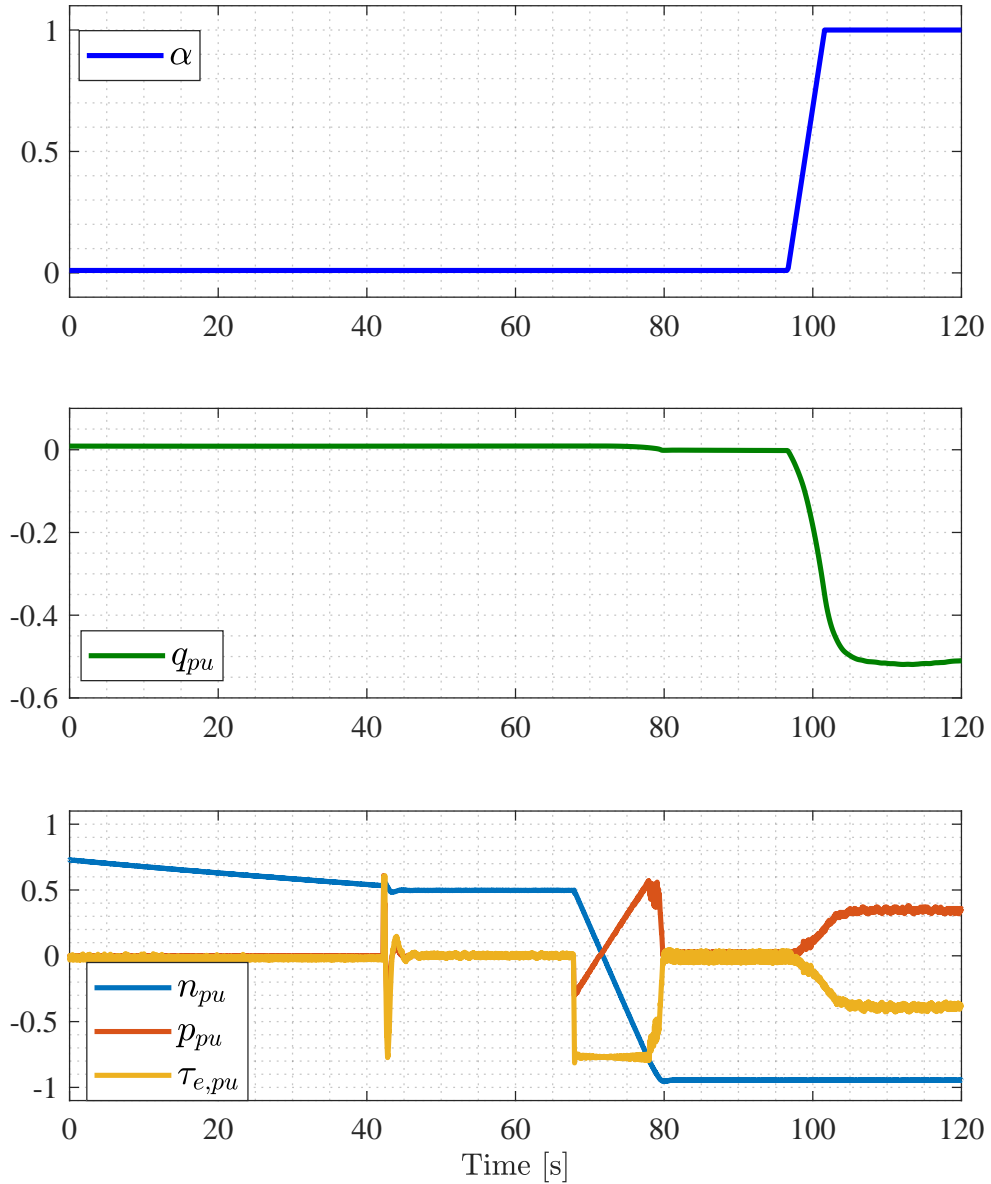### 7.4.4   Transition from the turbine to pump mode

The transition from turbine to pump mode is not possible without stopping the system in a PSHP with a fixed-speed synchronous machine or with a DFIM technology because the phase sequence of the stator connection needs to be changed to rotate the machine in the opposite direction.

When the secondary controller initiates the transition of operation mode from the turbine to pump mode, the AFE regulates the power to the grid close to zero, and accordingly, the guide vanes come to their minimum position as the load is minimum. The control mode of converters is then switched such that AFE controls the dc-link voltage and SM drive controls the speed. Now, the speed reference is set to -1 pu and the SM drive slowly ramps down the speed to the reference value to turn the rotation to the direction of pump mode. In the experimental setup, -0.93 pu is the zero water flow point where the pressure inside the turbine casing is equal to the static pressure in the penstock due to the gross head. Therefore, the speed is normally set to this value but a higher value is also allowed since the guide vanes are closed. The guide vanes are slowly opened to their maximum opening. The speed of the RPT is adjusted to control the pumping power to the available power from the grid or to the power set point ($P_{ref,pump}$) provided by the plant operator via the secondary controller. Since the torque loading is steep in pumping mode (as shown in Fig. 2.4), a small change in speed leads to a significant change in water flow and hence in pumping power.

The change in the control mode of the power drives affects the transition from the turbine to pump mode. The change of the control mode of the power drives should always be carried out when the speed is positive and at least around 0.5 pu because crossing zero speed with SM drive in dc-link control is not possible. The rotor at zero speed does not have any power to inject into the dc-link to control the voltage to the reference value.

Figure 7.7: Transition from pump to turbine mode. From $t = 0s$ to $t = 13s$, the RPT is running in pump mode and the guide vanes have been closed to initiate the transition of the mode of operation from the pump to the turbine. At $t = 13s$, the secondary controller changes the speed reference from -1 pu to 1 pu to turn the machine in the direction of turbine mode. At $t = 48s$, the governor is activated for speed control. At $t = 53s$, the control mode of the SM converter is switched from speed control to dc-link control and the same occurs for the grid-side converter from dc-link control to grid-connected u_{ac} and f_{grid} control. At $t = 65s$, the machine is loaded using grid-connected AFE.

Figure 7.8: Transition from turbine to pump mode. From $t = 0s$ to $t = 42s$, the RPT is running in turbine mode and the guide vanes are closed to initiate the transition of mode from the turbine to pump mode. At $t = 42s$, the control mode of the SM converter is switched from dc-link control to speed control and the same occurs for the grid-side converter from grid-connected u_{ac} and f_{grid} control to dc-link control. At $t = 68s$, the secondary controller changes the speed reference from 0.5 pu to -0.93 pu to turn the machine to the pump mode direction. At $t = 97s$, the guide vanes are opened to pump the water.

7.4.5   Low voltage ride through in turbine mode

Low voltage ride through (LVRT) is the functionality of the grid-side converter that is capable of tolerating a voltage dip or complete short circuit for a pre-specified time according to Grid-code regulation. The converter must not trip even though the voltage dips to zero for 150 ms [95, 96]. The worst-case scenario of zero voltage at AC terminals leads to a blockade of power flow from the machine to the grid. This case is similar to the load rejection case in a grid-connected synchronous machine.

As presented in Fig. 7.9, when the voltage dip occurs at $t = 0s$, the power out of the grid-side converter is blocked. Consequently, the electrical torque production from the machine-side converter is controlled to approximately zero to maintain the dc-link voltage to its set point. The governor of the RPT reacts immediately to control the guide vanes to maintain the reference speed of the machine, and consequently, the water flow also decreases from 0.62 pu to 0.49 pu. The fast reaction of the governor allows the machine speed to increase only by 2% as shown in the zoomed-in view of Fig. 7.9. The field weakening control of the synchronous machine controls the stator flux such that the stator voltage does not exceed the rated voltage in case of load rejection or low voltage ride-through conditions.

In turbine mode, the machine-side converter runs in dc-link control mode and the grid-side converter in grid forming mode. When the voltage dip occurs at $t = 0s$, the load rejection causes a sharp rise in dc-link voltage, which in turn controls the flow of current from the machine to the converter as shown in Fig. 7.10. The rise in voltage is less than 2%. When the grid is restored, the sudden loading causes a fall of around 3% in dc-link voltage, which is well within the permissible deviation. The d- and q- axes currents are controlled to zero during the voltage dip because there is no active power flow into the dc-link and the machine is magnetized only from the excitation converter.
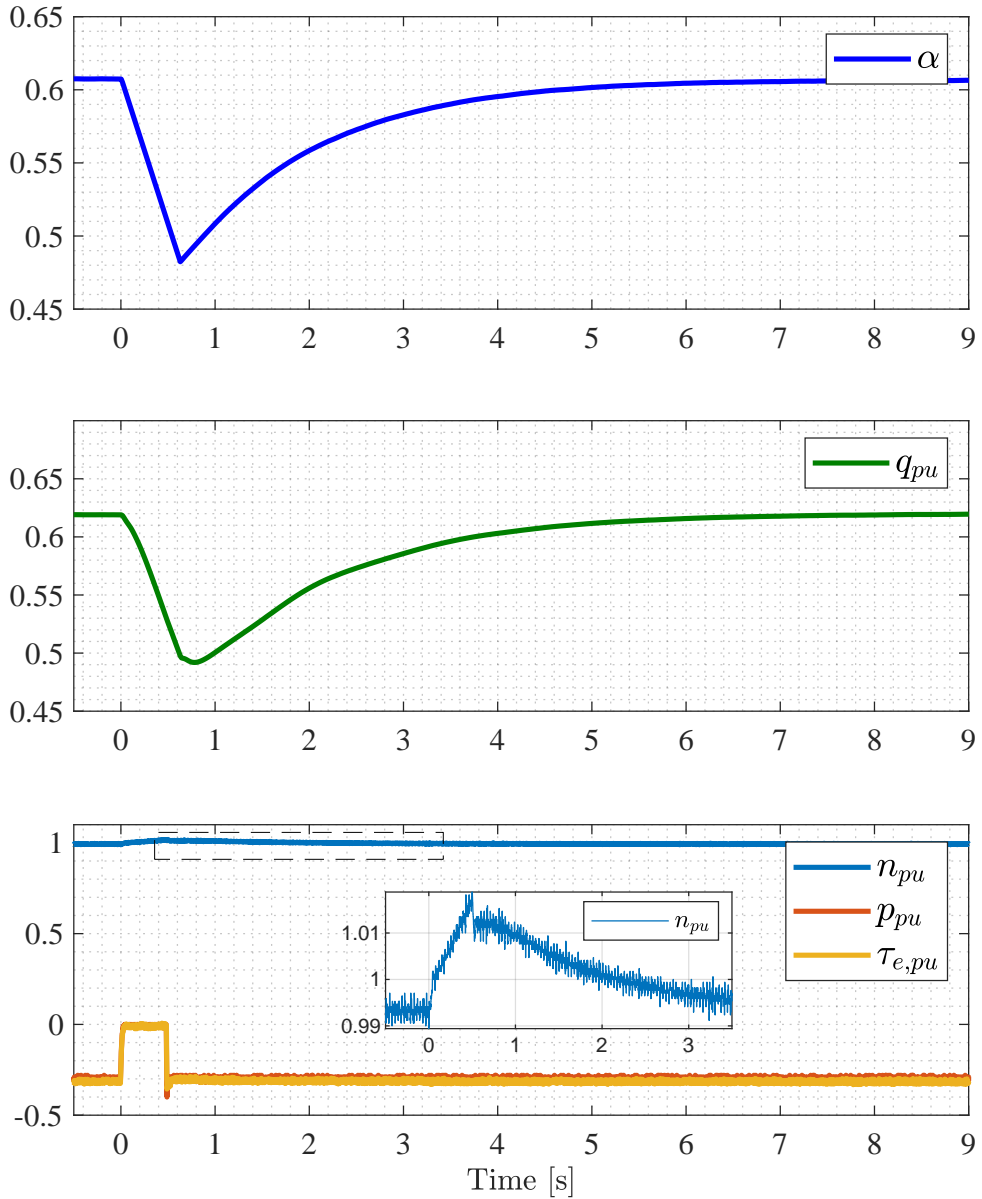
Figure 7.9: Low voltage ride through in turbine mode and the response of the hydraulic system. At $t = 0s$, a voltage dip on the grid side occurs and the power flow from the machine to the grid is blocked. The speed increases, but the governor activates and controls the speed. After the grid is restored, the electrical torque is again impressed on the RPT, and the governor again reacts by opening the guide vanes to the pre-fault position and hence the water flow.
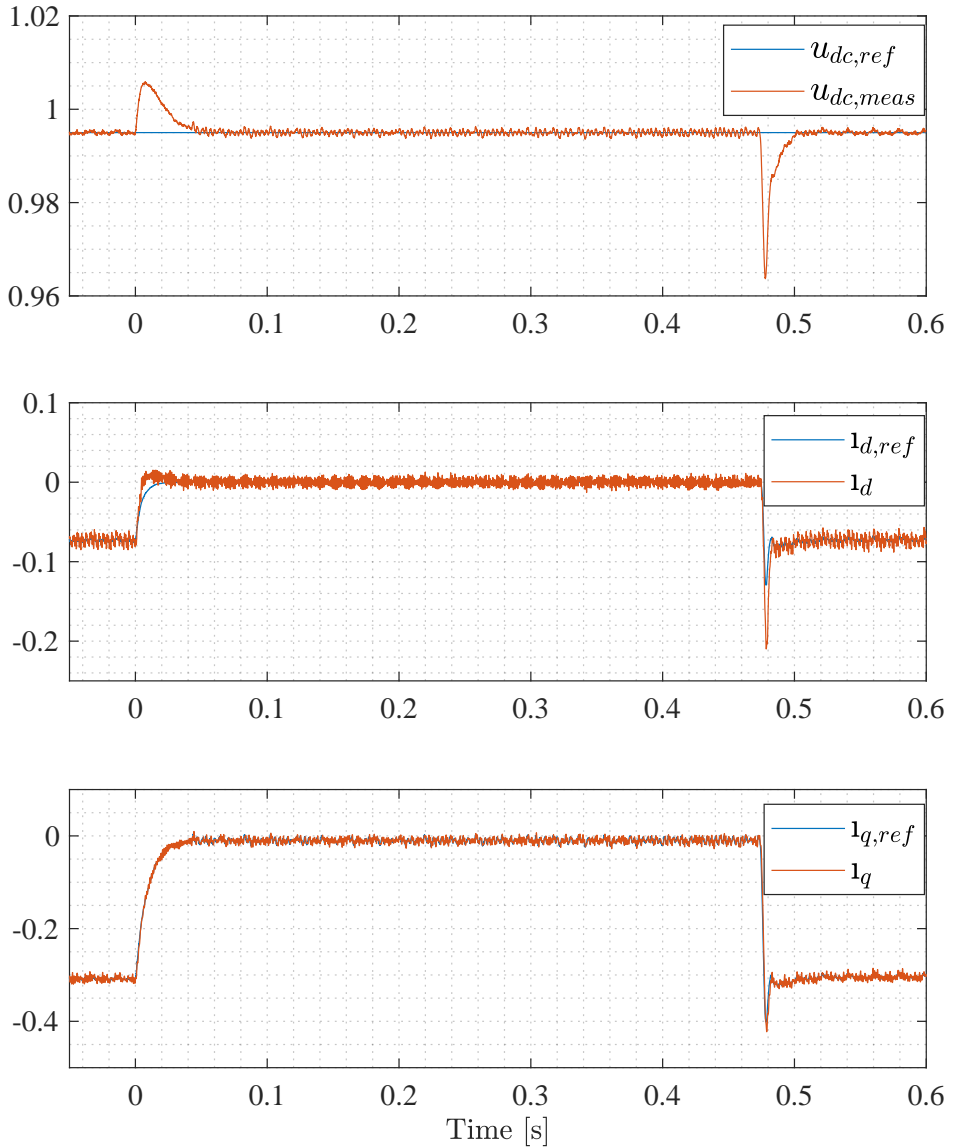
Figure 7.10: Low voltage ride through in turbine mode and the response of synchronous machine drives control parameters. Here the SM drive is in dc-link voltage control. At $t = 0s$, the grid voltage disappears and the power flow to the grid is blocked, and therefore, there is a rise in dc-link voltage. After 0.5 seconds of the grid disturbance, the power flow is resumed and the sudden loading gives a downward spike in dc-link voltage at $t = 0.48s$.
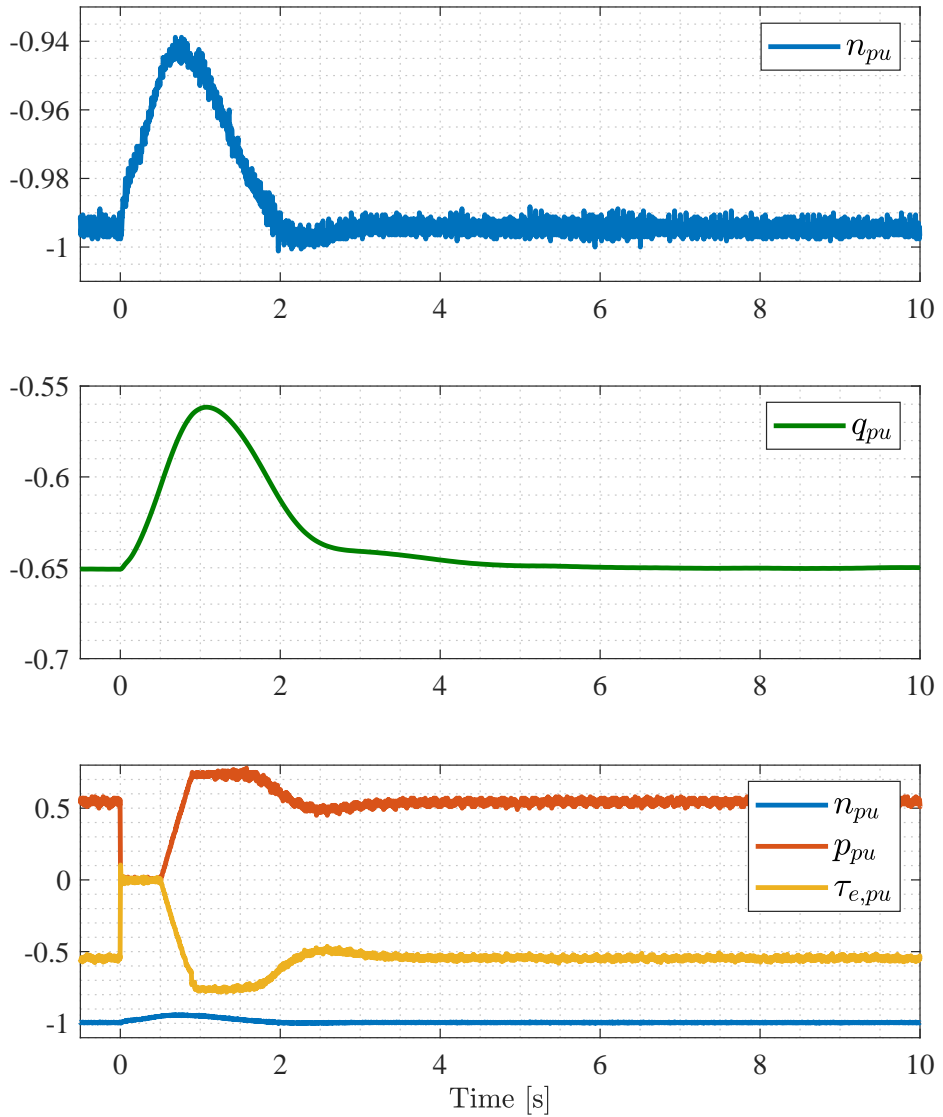
7.4.6   Low voltage ride through in pump mode

When there is a voltage dip at the ac terminals of the grid-side converter, the power available for pumping will be limited significantly due to the current rating of the semiconductor devices. The worst-case scenario is that there could be a short circuit at the AC terminals and the pumping power would completely be stopped. Since the electrical torque that is balancing the opposing torque produced by the water head disappears, the speed will decrease almost linearly with time. The mechanical time constant of the machine shaft is about 10 seconds, and therefore, the unavailability of pumping power for a duration of 0.5 seconds will lead to a 5% fall in speed. The fall in speed will lead to reduced pumping water flow as well. The guide vane remains fully open unless the short circuit is prolonged and a shutdown procedure is initiated.

The experimental result of this case is presented in Fig. 7.11. The short circuit at AC terminals occurs at $t = 0s$. Since there is no electrical power available, the electrical torque ($\tau_{e,pu}$) falls to zero, and so does the pumping power (p_{pu}). The speed falls from the steady state speed of 1 pu to 0.94 pu and the pumping water flow decreases from 0.65 pu to 0.56 pu. After the grid is restored at $t = 0.5s$, the electrical torque overshoots beyond its pre-fault value to achieve the reference speed. The water flow is also restored to its previous value as it depends on the speed of rotation. The system stabilizes in less than 10 seconds.

Some notable dynamics occur between the control parameters of the power converters as well. In pump mode, the grid-side converter controls the dc-link voltage and the machine-side converter controls the speed of the machine. During a short circuit, there is no power available to the dc-link; therefore, the machine-side converter runs in limitation to keep the dc-link voltage at the minimum set value of 0.91 pu as shown in Fig. 7.12. In this case, the converter imposes a very small torque on the rotating shaft to supply charging current to the dc-link capacitor. Since the energy required to maintain the dc-link voltage is quite low, it is not visible in the results. After the fault is cleared, the torque limit is slowly released for smooth loading of the grid, and the speed of the machine and dc-link voltage are restored to their pre-fault value.

Figure 7.11: Low voltage ride through in pump mode and the response of the hydraulic system. At $t = 0s$, a voltage dip on ac side of the grid-side converter occurs. Consequently, the electrical torque driving the machine disappears. The guide vane is fully open in pump mode, and therefore, the load torque produced by the pumping head causes the speed to fall until the grid recovers at $0.5s$.
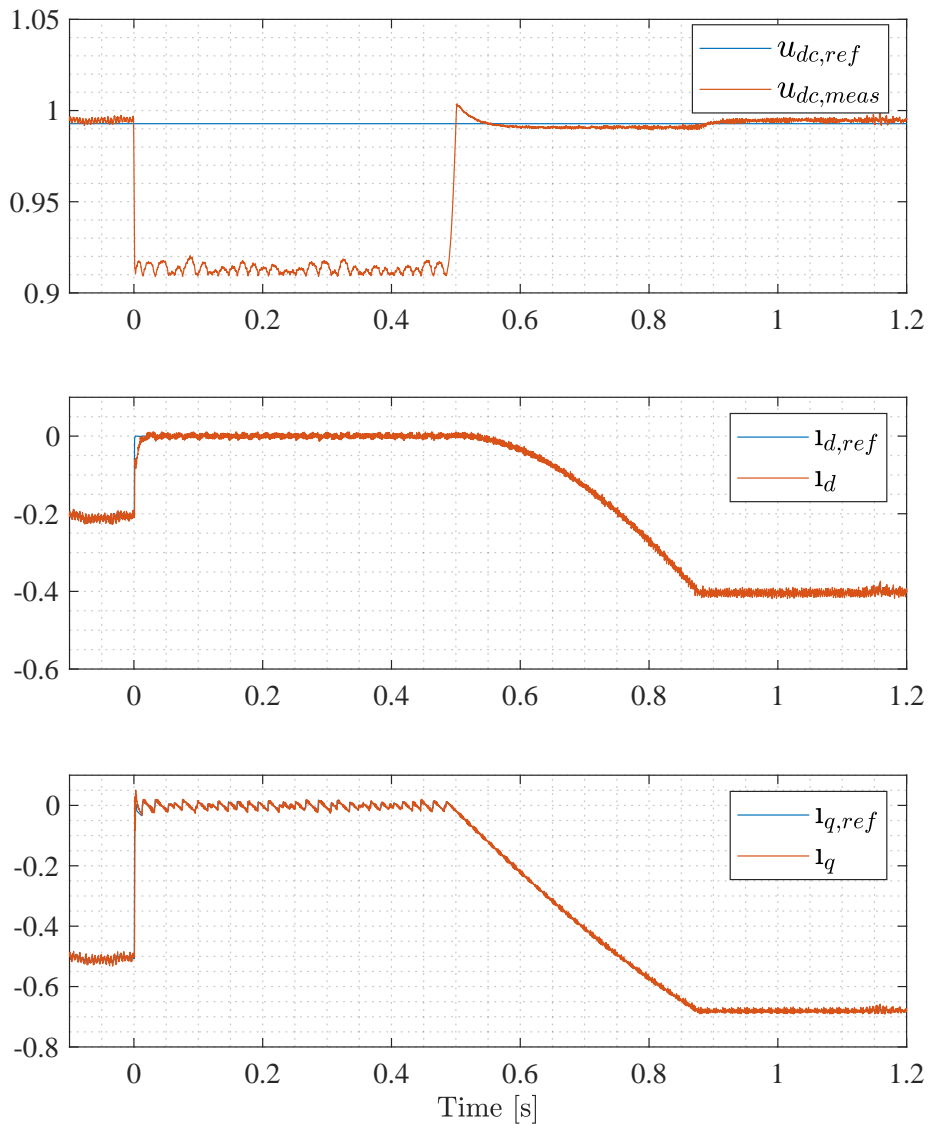
Figure 7.12: Low voltage ride through in pump mode and the response of synchronous machine drives control parameters. At $t = 0s$, a voltage dip occurs on the grid-side converter, and the power available for pumping disappears. The grid-side converter now has no power to control the dc-link voltage, and therefore, the dc-link voltage also experiences a steep fall. The dc-link voltage limiter in the SM converter supplies the power needed to keep the dc-link voltage to its minimum limit value. The grid is restored at $t = 0.5s$, and the power is available on the grid side. The grid-side converter controls the dc-link voltage to the reference value, and the limit on the d- and q-axis currents is slowly released to continue pumping.

7.5 Discussion

The most important operational scenarios of a PSHP with a full-size converter-fed synchronous machine have been presented. The experimental arrangement and the results demonstrate the control methods that can be implemented in a future PSHP. A few notable events from the experimental setup are worth presenting and are listed as follows:

1. In the laboratory setup, the OPAL-RT was used as the secondary controller, which had very fast communication to the grid-side converter over an optical fiber link whereas a relatively slow MODBUS TCP communication towards the machine-side converter. The transition could have been made faster and smoother with the optical fiber link to both converters, which could not be established in the laboratory due to a lack of hardware accessories. A faster communication to both of the back-to-back converters is crucial because none of the converters control the dc-link voltage during the mode transition and it stays at its upper or lower limit. In addition, the dynamics of the dc-link voltage controller can also be made smoother if both converter would have been controlled from the same control board.

2. The start-up time in pump mode is presented as 5–6 mechanical time constant because the machine-side converter has a limited torque capability in the low-speed region. It is about 33% for a 3-level NPC converter with IGCTs as presented in Chapter 5. In addition, the opening of the guide vanes takes approximately 30 seconds for a turbine unit in the range of 100 MW. Also, the start-up in turbine mode and in case of mode transitions can be made faster by implementing automated sequences.

3. A few instances of converters tripping unnecessarily during the experiment prompted the understanding that the control mode of converters should only be changed when the speed of the RPT is positive. The speed is assumed positive for turbine operation and negative for pump operation. If the control mode of the machine-side converter is changed from speed control to dc-link control when the speed is negative, the turbine governor will control the speed to the positive speed while changing the mode from pump to turbine. This will pass through zero speed when the SM converter is controlling the dc-link voltage. At zero speed, there is no EMF induced in the synchronous machine and the dc-link voltage uncontrollably drops below its lower limit causing an unnecessary trip.

4. The torque-speed characteristic of the RPT is quite steep in the nominal operating region in the pump mode. Therefore, the speed must be varied quite slowly to adapt to the power available from the grid. A slow change in speed also leads to smaller oscillations in the penstock and waterways.

7.6   Summary

Both the primary (stator current control) and the secondary controller for the control of a pumped storage plant were tested in a prototype laboratory setup. The experimental results verify the seamless transition of the mode of operation from the pump to the turbine and vice versa. The methodology implemented to handle the fault cases like low voltage ride through in both pump and turbine modes shows that the operation of the plant is not affected. These functionalities are very important for the reliable operation of a pumped storage plant.

Chapter 8

Conclusion and Future Work

8.1 Conclusion

With the growing production of power from intermittent renewable energy sources such as wind and solar, the need for variable-speed operation in pumped storage plants has gained significance. This is essential to maximize the utilization of clean energy from these sources and minimize energy curtailment. This thesis argues that it is feasible to retrofit existing fixed-speed synchronous machine-based pumped storage plants with frequency converters, thereby enabling variable-speed operation.

Upon examining the hydraulic system parameters, it became evident that there is potential to derive advantages from allowing the machine speed to deviate from the synchronous speed when it is decoupled from the grid. However, this deviation does not yield any benefits in terms of dampening the oscillations in the surge shaft and tunnel, as the period of oscillation spans minutes, and the machine shaft lacks the necessary inertial energy to address such a prolonged duration. Additionally, a slower speed would necessitate a larger torque to maintain constant power, resulting in a larger converter size and associated costs. Hence, the utilization of shaft inertia proves more efficient during part-load operation compared to operations close to full load.

The basic requirements for the converter for such cases are a transformerless connection of the converter to the stator of the machine and to the generator transformer which is around 13–15 kV rms for a machine in the range of 100 MVA, high torque in the low-speed region and provision of a starting torque around 13% at standstill.

The power plants fitted with reversible pump-turbine typically require 13% of rated torque at startup in pump mode. There exist several multilevel converter topologies that can fulfill this requirement. A detailed study of NPC, ANPC, and MMC converter topologies revealed that an NPC converter can provide 30%, ANPC can provide about 60% and MMC can provide about 35% of rated torque at standstill with state-of-the-art IGCTs as switching devices. An ANPC converter offers the best performance for starting torque and can be the potential solution for the machine-side converter. Since the grid side converter has an output frequency that is almost constant, both MMC and NPC converters can be the possible solution.

An additional sine wave filter or dv/dt filter may be required depending upon the type of insulation of the machine and the loss in the damper bars due to higher-order harmonics applied by the converter.

Detailed control strategies with a full-size converter were investigated in a laboratory prototype of a 100 kVA setup with an emulated reversible pump turbine. All the possible scenarios that can occur in such a system were experimentally verified. The test cases were a startup in pump and turbine mode, mode transition from the turbine to pump, mode transition from pump to the turbine, and low voltage ride through for a duration of 0.5 seconds in both pump and turbine mode.

With a full-size converter, a seamless transition from the turbine to pump mode and vice versa can be executed. This is one of the key advantages if a large power oscillation from the wind and solar plants needs to be regulated using pumped storage plants. The transition time can be less than one minute considering the mechanical time constant of the machine is 12 seconds.

In turbine mode, the low voltage ride-through behavior closely resembles load rejection in a directly grid-connected synchronous machine. The proposed control strategy, which restricts power to the dc-link based on the dc-link voltage limiter, has been successfully tested in experiments. A similar scenario was also examined in pump mode, and it was noted that a brief loss of grid power for 0.5 seconds did not have a critical impact on the decrease in speed. The dc-link voltage could be kept at its lower limit by absorbing power from the inertia of the shaft.

When a synchronous machine is powered by a full-size converter, it becomes possible to attain both maximum torque per amp and control for unity power factor by adjusting the excitation current based on the immediate torque requirements. This capability proves advantageous, especially in new PSHP installations, where the machine can be specifically designed to operate at unity power factor.

8.2   Future work

- Controlling the excitation and the stator converter from the same control board such that field current can be dynamically controlled in the same interrupt as the stator current. This would lead to achieving faster control of stator flux, and hence better torque control of the machine during dynamics.

- In this work, the control strategies have been tested with a reversible pump-turbine model emulated using a back-to-back converter-fed induction machine. The same strategies could be tested using a reversible pump turbine prototype in the laboratory.

- The total loss in the NPC and ANPC converters can be measured and the loss equations can experimentally be verified.

- Modular multilevel converters with half-bridge modules can be connected to the stator of the synchronous machine and the startup can be emulated. The startup load torque from the RPT can be increased to test the practical limit of the half-bridge MMC.

- MMC with batteries or other energy storage across submodules could also solve the problem of low starting torque. In addition, this will decouple the transient between the machine and the grid. For example, failure of the grid while the RPT is running in turbine mode may cause a steep rise in dc-link voltage. This can be avoided if there is an energy storage connected to the dc-link which can store the energy until the normal shutdown procedure is executed. Consequently, the machine also will not reach runaway speed and will experience less wear and tear.

Bibliography

[1] H. Kolstad, "Control of an Adjustable Speed Hydro utilizing Field Programmable Devices," PhD Thesis, Norwegian University of Science and Technology (NTNU), 2003.

[2] C. Farell and J. Gulliver, "Hydromechanics of Variable Speed Turbines," *Journal of Energy Engineering*, vol. 113, no. 1, pp. 1–13, 1987.

[3] M. Valavi and A. Nysveen, "Variable-speed operation of hydropower plants: Past, present, and future," in *2016 XXII International Conference on Electrical Machines (ICEM)*, Sep. 2016, pp. 640–646.

[4] M. Basić, P. C. O. Silva, and D. Dujić, "High Power Electronics Innovation Perspectives for Pumped Storage Power Plants," *Hydro 2018*, p. 10, Oct. 2018.

[5] Ø. J. Linnebo, "Turtallstyring og lastkontroll av pumpeaggregater: Metoder og løsninger for eksisterende og nye anlegg (in Norwegian)," in *Produksjonsteknisk Konferanse (PTK)*, Oslo, 2013.

[6] L. Empringham, J. W. Kolar, J. Rodriguez, P. W. Wheeler, and J. C. Clare, "Technological Issues and Industrial Application of Matrix Converters: A Review," *IEEE Transactions on Industrial Electronics*, vol. 60, no. 10, pp. 4260–4271, 2013.

[7] D. Casadei, G. Grandi, C. Rossi, A. Trentin, and L. Zarri, "Comparison between back-to-back and matrix converters based on thermal stress of the switches," in *2004 IEEE International Symposium on Industrial Electronics*, vol. 2, 2004, pp. 1081–1086 vol. 2.

[8] R. Tiwari, R. Nilsen, and A. Nysveen, "Active NPC Converter for Variable Speed Operation of Pumped Storage Hydropower Plant," in *IECON 2020 The 46th Annual Conference of the IEEE Industrial Electronics Society*, Singapore, 2020, pp. 1211–1216.

[9] A. J. Korn, M. Winkelnkemper, and P. Steimer, "Low output frequency operation of the Modular Multi-Level Converter," in *IEEE Energy Conversion Congress and Exposition*, 2010, pp. 3993–3997.

[10] M. Hagiwara, I. Hasegawa, and H. Akagi, "Start-Up and Low-Speed Operation of an Electric Motor Driven by a Modular Multilevel Cascade Inverter," *IEEE Transactions on Industry Applications*, vol. 49, no. 4, pp. 1556–1565, 2013.

[11] A. Antonopoulos, L. Ängquist, S. Norrga, K. Ilves, L. Harnefors, and H. Nee, "Modular Multilevel Converter AC Motor Drives With Constant Torque From Zero to Nominal Speed," *IEEE Transactions on Industry Applications*, vol. 50, no. 3, pp. 1982–1993, 2014.

[12] W. F. Pickard, "The History, Present State, and Future Prospects of Underground Pumped Hydro for Massive Energy Storage," *Proceedings of the IEEE*, vol. 100, no. 2, pp. 473–483, 2012.

[13] Linth-Limmern - Securing future electricity supply | GE Renewable Energy. [Online]. Available: https://www.ge.com/renewableenergy/stories/linthal-securing-future

[14] T. Beyer, "Goldisthal Pumped-Storage Plant: More than Power Production," *Hydro Review*, vol. 15, no. 1, Mar. 2007. [Online]. Available: https://www.hydroworld.com/articles/print/volume-15/issue-1/articles/goldisthal-pumped-storage-plant-more-than-power-production.html

[15] Voith builds the first pumped storage plant in Germany. [Online]. Available: https://www.voith.com/ca-en/markets-industries/hydro-power/pumped-storage-plants-541.html

[16] Voith Pumped storage machines. [Online]. Available: https://voith.com/ca-en/11_06_Broschuere-Pumped-storage_einzeln.pdf

[17] "Lithium-Ion Battery." [Online]. Available: https://www.cei.washington.edu/education/science-of-solar/battery-technology/

[18] Outline History of Nuclear Energy. [Online]. Available: https://toshiba-mirai-kagakukan.jp/en/learn/history/ichigoki/index.htm

[19] World's First Adjustable-Speed Pumped-Storage Generating System. [Online]. Available: https://www.world-nuclear.org

[20] H. Schlunegger and A. Thöni, "100MW full-size converter in the Grimsel 2 pumped-storage plant," *Innsbruck, Hydro*, 2013. [Online]. Available: www.grimselstrom.ch/home/download/1291

[21] H. Schlunegger, "A 100MW converter for the Grimsel 2 pumped storage plant," *ABB Review*, p. 6, 2014.

[22] A. Christe, A. Faulstich, M. Vasiladiotis, and P. Steinmann, "World's First Fully-Rated Direct ac/ac MMC for Variable-Speed Pumped-Storage Hy-

dropower Plants," *IEEE Transactions on Industrial Electronics*, pp. 1–10, 2022.

[23] E. F. W. Alexanderson and E. L. Phillipi, "History and development of the electronic power converter," *Electrical Engineering*, vol. 63, no. 9, pp. 654–657, 1944.

[24] B. K. Bose, "The past, present, and future of power electronics [Guest Introduction]," *IEEE Industrial Electronics Magazine*, vol. 3, no. 2, pp. 7–11, 14, 2009.

[25] M. Yano, S. Abe, and E. Ohno, "History of Power Electronics for Motor Drives in Japan," in *2004 IEEE Conference on the History of Electronics*, 2004, p. 11.

[26] H. Akagi, "The state-of-the-art of power electronics in Japan," *IEEE Transactions on Power Electronics*, vol. 13, no. 2, pp. 345–356, 1998, conference Name: IEEE Transactions on Power Electronics.

[27] Y. Li and Y. W. Li, "The Evolutions of Multilevel Converter Topology: A Roadmap of Topological Invention," *IEEE Industrial Electronics Magazine*, vol. 16, no. 1, pp. 11–18, 2022.

[28] K. Matsuse, S. Saito, and S. Tadakuma, "History of Motor Drive Technologies in Japan, Part 1 [History]," *IEEE Industry Applications Magazine*, vol. 19, no. 6, pp. 10–17, 2013, conference Name: IEEE Industry Applications Magazine.

[29] D. Frank, "The development of power electronics in Europe," in *2004 IEEE Conference on the History of Electronics*, 2004, p. 11.

[30] G. S. Zinoviev and N. N. Lopatkin, "Evolution of multilevel voltage source inverters," in *2008 9th International Conference on Actual Problems of Electronic Instrument Engineering*, vol. 01, 2008, pp. 125–136.

[31] P. Wheeler, J. Rodriguez, J. Clare, L. Empringham, and A. Weinstein, "Matrix converters: a technology review," *IEEE Transactions on Industrial Electronics*, vol. 49, no. 2, pp. 276–288, 2002.

[32] J. Lung, Y. Lu, W. Hung, and W. Kao, "Modeling and Dynamic Simulations of Doubly Fed Adjustable-Speed Pumped Storage Units," *IEEE Transactions on Energy Conversion*, vol. 22, no. 2, pp. 250–258, 2007.

[33] T. Kuwabara, A. Shibuya, H. Furuta, E. Kita, and K. Mitsuhashi, "Design and dynamic response characteristics of 400 MW adjustable speed pumped storage unit for Ohkawachi Power Station," *IEEE Transactions on Energy Conversion*, vol. 11, no. 2, pp. 376–384, 1996.

[34] A. Bocquel and J. Janning, "Analysis of a 300 MW variable speed drive for pump-storage plant applications," in *2005 European Conference on Power Electronics and Applications (EPE)*, Sep. 2005, pp. 1–10.

[35] A. Joseph and T. R. Chelliah, "A Review of Power Electronic Converters for Variable Speed Pumped Storage Plants: Configurations, Operational Challenges, and Future Scopes," *IEEE Journal of Emerging and Selected Topics in Power Electronics*, vol. 6, no. 1, pp. 103–119, 2018.

[36] K. Desingu, R. Selvaraj, T. R. Chelliah, and D. Khare, "Effective Utilization of Parallel-Connected Megawatt Three-Level Back-to-Back Power Converters in Variable Speed Pumped Storage Units," *IEEE Transactions on Industry Applications*, vol. 55, no. 6, pp. 6414–6426, 2019.

[37] J. Koutnik, "Frades II -variable speed pumped storage project and its benefit to the electrical grid," in *International Conference on Renewable Energy*, Jan 2012, pp. 1–7.

[38] "MEGADRIVE-LCI." [Online]. Available: https://new.abb.com/drives/medium-voltage-ac-drives/megadrive-lci

[39] J. M. Merino and A. Lopez, "ABB Varspeed generator boosts efficiency and operating flexibility of hydropower plant," *ABB Review*, no. 3/1996, pp. 33–38, 1996.

[40] T. Kunz, G. Sari, A. Schwery, R. Guillaume, and J.-M. Henry, "Commissioning and operation of variable speed units at the 1000 MW Linthal pumped-storage plant," *The International Journal on Hydropower & Dams*, vol. 24, pp. 50–50, 2017.

[41] E. L. Engevik, T. E. Hestengen, M. Valavi, and A. Nysveen, "Effects of lifting reactance requirements on the optimal design of converter-fed synchronous hydrogenerators," in *2017 IEEE International Electric Machines and Drives Conference (IEMDC)*, 2017, pp. 1–8.

[42] T. Holzer, A. Muetze, G. Traxler-Samek, M. Lecker, and F. Zerobin, "Generator Design Possibilities for Full-Size Converter Operation of Large Pumped Storage Power Plants," *IEEE Transactions on Industry Applications*, vol. 56, no. 4, pp. 3644–3655, 2020.

[43] D. Johannesson, M. Nawaz, and K. Ilves, "Assessment of 10 kv, 100 a silicon carbide mosfet power modules," *IEEE Transactions on Power Electronics*, vol. 33, no. 6, pp. 5215–5225, 2018.

[44] J. Thoma, B. Volzer, D. Kranzer, D. Derix, and A. Hensel, "Design and commissioning of a 10 kv three-phase transformerless inverter with 15 kv silicon carbide mosfets," in *2018 20th European Conference on Power Electronics and Applications (EPE'18 ECCE Europe)*, 2018, pp. P.1–P.7.

[45] D. N. Dalal, H. Zhao, J. K. Jørgensen, N. Christensen, A. B. Jørgensen, S. Beczkowski, C. Uhrenfeldt, and S. Munk-Nielsen, "Demonstration of a 10 kv sic mosfet based medium voltage power stack," in *2020 IEEE Applied Power Electronics Conference and Exposition (APEC)*, 2020, pp. 2751–2757.

[46] T. J. Hammons and J. Loughran, "Starting methods for generator/motor units employed in pumped-storage stations," *Proceedings of the Institution of Electrical Engineers*, vol. 117, no. 9, pp. 1829–1840, Sep. 1970.

[47] M. Canay, "Asynchronous Starting of a 230 MVA Synchronous Machine in 'Vianden 10' Pumped Storage Station," *Brown Boveri Rev.*, vol. 61, no. 7, pp. 313–318, Jul. 1974.

[48] S. Pejovic and B. Karney, "Guidelines for transients are in need of revision," *IOP Conference Series: Earth and Environmental Science*, vol. 22, no. 4, p. 042006, Mar. 2014.

[49] M. F. Svarstad, "Fast Transition between Operational Modes of a reversible Pump-Turbine," PhD Thesis, Norwegian University of Sciency and Technology (NTNU), 2019.

[50] T. K. Nielsen, "Simulation model for Francis and Reversible Pump Turbines," *International Journal of Fluid Machinery and Systems*, vol. 8, no. 3, pp. 169–182, 2015.

[51] X. Yang, C. Yang, C. Yue, D. Yao, and C. Yuan, "Optimized Operation of Hydropower Plant with VSC HVDC Unit Connection," in *CIGRE AORC Technical Meeting*, 2014.

[52] B. Neupane, K. Vereide, and K. K. Panthi, "Operation of Norwegian Hydropower Plants and Its Effect on Block Fall Events in Unlined Pressure Tunnels and Shafts," *Water*, vol. 13, no. 11, 2021. [Online]. Available: https://www.mdpi.com/2073-4441/13/11/1567

[53] M. Bolstad, "Sensorless Control of Synchronous Machines Used in Adjustable Speed Hydro," Master's thesis, Norwegian University of Science and Technology (NTNU), 2018.

[54] H. Bühler, *Einführung in die Theorie Geregelter Drehstromantriebe Band 2. Anwendungen*. Birkhäuser Basel, 1977.

[55] R. Bhatia, H. Krattiger, A. Bonanini, D. Schafer, J. T. Inge, and G. H. Sydnor, "Adjustable speed drive using a single 135000 HP synchronous motor," *IEEE Transactions on Energy Conversion*, vol. 14, no. 3, pp. 571–576, 1999.

[56] G. Sydnor, R. Bhatia, H. Krattiger, J. Mylius, D. Schäfer, and E. Carpenter, "Fifteen years of operation at NASA's National Transonic Facility with the world's largest adjustable speed drive," in *6th IET International Conference on Power Electronics, Machines and Drives (PEMD 2012)*, 2012, pp. 1–10.

[57] L. Empringham, J. W. Kolar, J. Rodriguez, P. W. Wheeler, and J. C. Clare, "Technological Issues and Industrial Application of Matrix Converters: A Review," *IEEE Transactions on Industrial Electronics*, vol. 60, no. 10, pp. 4260–4271, 2013.

[58] K. Sharifabadi, L. Harnefors, H.-P. Nee, S. Norrga, and R. Teodorescu, *Design, Control, and Application of Modular Multilevel Converters for HVDC Transmission Systems*.   John Wiley & Sons, Ltd, 2016.

[59] R. Lund, "Multilevel Power Electronic Converters for Electrical motor Drives," PhD Thesis, Norwegian University of Science and Technology (NTNU), 2005.

[60] P. K. Steimer, O. Senturk, S. Aubert, and S. Linder, "Converter-fed synchronous machine for pumped hydro storage plants," in *2014 IEEE Energy Conversion Congress and Exposition (ECCE)*, Pittsburgh, Sep. 2014, pp. 4561–4567.

[61] "ABB medium voltage AC drives." [Online]. Available: https://new.abb.com/drives/medium-voltage-ac-drives

[62] "GE - Medium Voltage Drives." [Online]. Available: https://www.gepowerconversion.com/product-solutions/medium-voltage-drives/mv7000

[63] "SINAMICS Medium Voltage Converters." [Online]. Available: https://new.abb.com/drives/medium-voltage-ac-drives

[64] T. Wikstroem and D. Cottet, "A 6500 A, 4500V, 94 mm Assymmetric IGCT," in *PCIM Europe digital days 2020; International Exhibition and Conference for Power Electronics, Intelligent Motion, Renewable Energy and Energy Management*, 2020, pp. 1–5.

[65] J. W. Kolar, H. Ertl, and F. Zach, "Calculation of the Passive and Active Component Stress of Three-Phase PWM Converter Systems with High Pulse Rate," in *Proc. Eur. Conf. Power Electronics and Applications*, Aachen, 1989, pp. 1303–1311.

[66] G. Tomta and R. Nilsen, "Analytical Equations for Three Level NPC Converters," in *9th European Conference on Power Electronics and Applications*, Graz, 2001.

[67] R. Lund, J. Beverfjord, S. Øvrebø, and R. Nilsen, "Analytical Power Loss Expressions for Diode Clamped Converters," in *10th European Conference on Power Electronics and Applications*, Dubrovnik and Cavtat, 2002.

[68] P. Barbosa, P. Steimer, J. Steinke, M. Winkelnkemper, and N. Celanovic, "Active-neutral-point-clamped (ANPC) multilevel converter technology," in *2005 European Conference on Power Electronics and Applications*, 2005, pp. 10 pp.–P.10.

[69] Thomas Bruckner, Steffen Bernet, and P. K. Steimer, "The active NPC converter for medium-voltage applications," in *Fourtieth IAS Annual Meeting. Conference Record of the 2005 Industry Applications Conference, 2005.*, vol. 1, 2005, pp. 84–91 Vol. 1.

[70] A. Lesnicar and R. Marquardt, "An innovative modular multilevel converter topology suitable for a wide power range," in *2003 IEEE Bologna Power Tech Conference Proceedings*, vol. 3, Jun. 2003.

[71] ——, "A new modular voltage source inverter topology," in *European Power Electronics (EPE) Conference Proceedings*, 2003.

[72] K. Ilves, A. Antonopoulos, S. Norrga, and H.-P. Nee, "Steady-State Analysis of Interaction Between Harmonic Components of Arm and Line Quantities of Modular Multilevel Converters," *IEEE Transactions on Power Electronics*, vol. 27, no. 1, pp. 57–68, Jan. 2012.

[73] A. Antonopoulos, L. Angquist, and H. Nee, "On dynamics and voltage control of the Modular Multilevel Converter," in *2009 13th European Conference on Power Electronics and Applications*, 2009, pp. 1–10.

[74] Q. Tu, Z. Xu, and L. Xu, "Reduced Switching-Frequency Modulation and Circulating Current Suppression for Modular Multilevel Converters," *IEEE Transactions on Power Delivery*, vol. 26, no. 3, pp. 2009–2017, 2011.

[75] K. Ilves, A. Antonopoulos, L. Harnefors, S. Norrga, and H. Nee, "Circulating current control in modular multilevel converters with fundamental switching frequency," in *Proceedings of The 7th International Power Electronics and Motion Control Conference*, vol. 1, 2012, pp. 249–256.

[76] X. She, A. Huang, X. Ni, and R. Burgos, "AC circulating currents suppression in modular multilevel converter," in *IECON 2012 - 38th Annual Conference on IEEE Industrial Electronics Society*, 2012, pp. 191–196.

[77] G. Konstantinou, J. Pou, S. Ceballos, R. Picas, J. Zaragoza, and V. G. Agelidis, "Control of Circulating Currents in Modular Multilevel Converters Through Redundant Voltage Levels," *IEEE Transactions on Power Electronics*, vol. 31, no. 11, pp. 7761–7769, 2016.

[78] M. Hagiwara, K. Nishimura, and H. Akagi, "A Medium-Voltage Motor Drive With a Modular Multilevel PWM Inverter," *IEEE Transactions on Power Electronics*, vol. 25, no. 7, pp. 1786–1799, 2010.

[79] "Asymmetric and reverse conducting (IGCTs) | Hitachi ABB," [online] https://www.hitachiabb-powergrids.com/offering/product-and-system/semiconductors/integrated-gate-commutated-thyristors-igct/asymmetric-and-reverse-conducting. [Online]. Available: https://www.hitachiabb-powergrids.com/offering/product-and-system/semiconductors/integrated-gate-commutated-thyristors-igct/asymmetric-and-reverse-conducting

[80] "IXYS UK Westcode - Press-pack IGBT Capsules." [Online]. Available: http://www.westcode.com/igbt1.html

[81] "Press-Pack package, Toshiba Electronic Devices & Storage Corporation," library Catalog: toshiba.semicon-storage.com. [Online]. Avail-

able: https://toshiba.semicon-storage.com/ap-en/semiconductor/product/high-power-devices/iegt-ppi/press-pack-package.html

[82] "Webra High Quality Thermal Solutions - Cold Plate Catalogue." [Online]. Available: http://www.webra.se

[83] J. Rodriguez, B. Wu, S. Bernet, N. Zargari, J. Rebolledo, J. Pontt, and P. Steimer, "Design and Evaluation Criteria for High Power Drives," in *IEEE Industry Applications Society Annual Meeting*, 2008, pp. 1–9.

[84] N. Mohan, T. M. Undeland, and W. P. Robbins, *Power Electronics: Converters, Applications, and Design*, 3rd ed.   John Wiley & Sons, Inc., 2002.

[85] D. Krug, S. Bernet, S. S. Fazel, K. Jalili, and M. Malinowski, "Comparison of 2.3-kV Medium-Voltage Multilevel Converters for Industrial Medium-Voltage Drives," *IEEE Transactions on Industrial Electronics*, vol. 54, no. 6, pp. 2979–2992, 2007.

[86] R. Tiwari, R. Nilsen, and A. Nysveen, "Modular Multilevel Converter for Variable Speed Operation of Pumped Storage Hydropower Plants," in *PCIM Europe digital days 2021; International Exhibition and Conference for Power Electronics, Intelligent Motion, Renewable Energy and Energy Management*, 2021, pp. 1–8.

[87] M. Vasiladiotis, R. Baumann, C. Häderli, and J. Steinke, "IGCT-Based Direct AC/AC Modular Multilevel Converters for Pumped Hydro Storage Plants," in *2018 IEEE Energy Conversion Congress and Exposition (ECCE)*, 2018, pp. 4837–4844.

[88] D. Weiss, M. Vasiladiotis, C. Banceanu, N. Drack, B. Odegard, and A. Grondona, "IGCT based Modular Multilevel Converter for an AC-AC Rail Power Supply," in *PCIM Europe 2017; International Exhibition and Conference for Power Electronics, Intelligent Motion, Renewable Energy and Energy Management*, 2017, pp. 1–8.

[89] M. Winkelnkemper, A. Korn, and P. Steimer, "A modular direct converter for transformerless rail interties," in *2010 IEEE International Symposium on Industrial Electronics*, 2010, pp. 562–567.

[90] K. Ilves, S. Norrga, L. Harnefors, and H. Nee, "On Energy Storage Requirements in Modular Multilevel Converters," *IEEE Transactions on Power Electronics*, vol. 29, no. 1, pp. 77–88, 2014.

[91] D. G. Holmes and T. A. Lipo, *Pulse Width Modulation for Power Converters: Principles and Practice, Ch. 3*.   Wiley - IEEE Press, 2003.

[92] A. Kjølle, *Hydropower in Norway - Mechanical Equipment*.   Norwegian University of Science and Technology (NTNU), 2001.

[93] T. I. Reigstad and K. Uhlen, "Variable Speed Hydropower Conversion and Control," *IEEE Transactions on Energy Conversion*, vol. 35, no. 1, pp. 386–393, 2020.

[94] K. Gamlesaeter, "Starting methods for pump stoarge units," in *Cigre*, Paris, France, 1991.

[95] G. Joos, "Wind turbine generator low voltage ride through requirements and solutions," in *2008 IEEE Power and Energy Society General Meeting - Conversion and Delivery of Electrical Energy in the 21st Century*, 2008, pp. 1–7.

[96] Y. Bak, J.-S. Lee, and K.-B. Lee, "Low-Voltage Ride-Through Control Strategy for a Grid-Connected Energy Storage System," *Applied Sciences*, vol. 8, no. 1, 2018. [Online]. Available: https://www.mdpi.com/2076-3417/8/1/57

[97] R. Nilsen, "TET4120 Electric Drives, Course Compendium, Department of Electric Power Engineering, Norwegian University of Science and Technology (NTNU)," 2018.

Appendix A

Modeling of Synchronous Machine

A.1 Voltage equations

Synchronous machine modeling is based on these equations:

$$U_s = R_s I_s + \frac{d\Psi_s}{dt} \tag{A.1}$$

$$U_r = R_r I_r + \frac{d\Psi_r}{dt} \tag{A.2}$$

The above equations can be expanded for stator, field, and damper windings as follows:

$$
\begin{aligned}
U_{sa} &= R_s I_{sa} + \frac{d\Psi_{sa}}{dt} \\
U_{sb} &= R_s I_{sb} + \frac{d\Psi_{sb}}{dt} \\
U_{sc} &= R_s I_{sc} + \frac{d\Psi_{sc}}{dt}
\end{aligned} \tag{A.3}
$$

$$U_f = R_f I_f + \frac{d\Psi_f}{dt} \tag{A.4}$$

$$
\begin{aligned}
U_D &= R_D I_D + \frac{d\Psi_D}{dt} \\
U_Q &= R_Q I_Q + \frac{d\Psi_Q}{dt}
\end{aligned} \tag{A.5}
$$

The per unit voltage equations in a synchronously rotating reference frame i.e., d-q

coordinate can be expressed as:

$$u_d = r_s i_d + \frac{1}{\omega_n}\frac{d\psi_d}{dt} - n\psi_q \tag{A.6}$$

$$u_q = r_s i_q + \frac{1}{\omega_n}\frac{d\psi_q}{dt} + n\psi_d \tag{A.7}$$

$$u_f = r_f i_f + \frac{1}{\omega_n}\frac{d\psi_f}{dt} \tag{A.8}$$

$$0 = r_D i_D + \frac{1}{\omega_n}\frac{d\psi_D}{dt} \tag{A.9}$$

$$0 = r_Q i_Q + \frac{1}{\omega_n}\frac{d\psi_Q}{dt} \tag{A.10}$$

The flux linkages in the above equations can further be expressed as follows:

$$\psi_d = x_d i_d + x_{md}(i_D + i_f) \tag{A.11}$$

$$\psi_q = x_q i_q + x_{mq} i_Q \tag{A.12}$$

$$\psi_f = x_f i_f + x_{md}(i_d + i_D) \tag{A.13}$$

$$\psi_D = x_D i_D + x_{md}(i_d + i_f) \tag{A.14}$$

$$\psi_Q = x_Q i_Q + x_{mq} i_q \tag{A.15}$$

The above equation can be written in matrix format as below:

$$\begin{bmatrix} \psi_d \\ \psi_q \\ \psi_f \\ \psi_D \\ \psi_Q \end{bmatrix} = \begin{bmatrix} x_d & 0 & x_{md} & x_{md} & 0 \\ 0 & x_q & 0 & 0 & x_{mq} \\ x_{md} & 0 & x_f & x_{md} & 0 \\ x_{md} & 0 & x_{md} & x_D & 0 \\ 0 & x_{mq} & 0 & 0 & x_Q \end{bmatrix} \cdot \begin{bmatrix} i_d \\ i_q \\ i_f \\ i_D \\ i_Q \end{bmatrix} \tag{A.16}$$

The relation between self-inductance and mutual inductance can be expressed in terms of leakage factor σ as follows:

$$x_d = x_{md}(1 + \sigma_d) \tag{A.17}$$

$$x_q = x_{mq}(1 + \sigma_q) \tag{A.18}$$

$$x_f = x_{md}(1 + \sigma_f) \tag{A.19}$$

$$x_D = x_{md}(1 + \sigma_D) \tag{A.20}$$

$$x_Q = x_{mq}(1 + \sigma_Q) \tag{A.21}$$

A.2 Alternative pu model

A.2.1 Flux linkage in stator winding

Since the damper winding currents can not be measured, the equations for flux linkages can be rearranged without these currents and can be re-written as follows:

$$\psi_d = \sigma_{dD} x_d i_d + \frac{\sigma_D}{1 + \sigma_D} x_{md} i_f + \frac{\psi_D}{1 + \sigma_D} \tag{A.22}$$

$$\psi_q = \sigma_{qQ} x_q i_q + \frac{\psi_Q}{1 + \sigma_Q} \tag{A.23}$$

$$\psi_f = \sigma_{Df} x_f i_f + \frac{\sigma_D}{1 + \sigma_D} x_{md} i_d + \frac{\psi_D}{1 + \sigma_D} \tag{A.24}$$

$$\frac{d\psi_D}{dt} = -\frac{\psi_D}{T_D} + \frac{x_{md}}{T_D}(i_d + i_f) \tag{A.25}$$

$$\frac{d\psi_Q}{dt} = -\frac{\psi_Q}{T_Q} + \frac{x_{mq}}{T_Q} i_q \tag{A.26}$$

where the relation between leakage factors σ can be expressed as follows:

$$\sigma_{dD} = 1 - \frac{1}{(1 + \sigma_d)(1 + \sigma_D)} \tag{A.27}$$

$$\sigma_{qQ} = 1 - \frac{1}{(1 + \sigma_q)(1 + \sigma_Q)} \tag{A.28}$$

$$\sigma_{fD} = 1 - \frac{1}{(1 + \sigma_f)(1 + \sigma_D)} \tag{A.29}$$

$$r'_d = r_s + \frac{r_D}{(1 + \sigma_D)^2} \tag{A.30}$$

$$r'_q = r_s + \frac{r_Q}{(1 + \sigma_Q)^2} \tag{A.31}$$

$$r'_f = r_f + \frac{r_D}{(1 + \sigma_D)^2} \tag{A.32}$$

$$T_D = \frac{x_D}{\omega_n r_D} \tag{A.33}$$

$$T_Q = \frac{x_Q}{\omega_n r_Q} \tag{A.34}$$

A.2.2 Voltage equations

Similarly, the voltage equations can be rearranged as follows:

$$u_d = r_d' i_d + \frac{\sigma_{dD} x_d}{\omega_n} \frac{di_d}{dt} + \frac{r_D}{(1+\sigma_D)^2}(i_f + \sigma_D T_D \frac{di_f}{dt}) - \frac{\psi_D}{\omega_n T_D(1+\sigma_D)} - n\psi_q$$

$$\text{(A.35)}$$

$$u_q = r_q' i_q + \frac{\sigma_{qQ} x_q}{\omega_n} \frac{di_q}{dt} - \frac{\psi_Q}{(1+\sigma_Q)\omega_n T_Q} + n\psi_d \tag{A.36}$$

$$u_f = r_f' i_f + \frac{\sigma_{fD} x_f}{\omega_n} \frac{di_f}{dt} + \frac{r_D}{(1+\sigma_D)^2}(i_d + \sigma_D T_D \frac{di_d}{dt}) - \frac{\psi_D}{\omega_n T_D(1+\sigma_D)}$$

$$\text{(A.37)}$$

Further substitution in the equations (A.35) – (A.37) modifies the equations to:

$$u_d = r_d'' \cdot i_d + \frac{x_d''}{\omega_n} \cdot \frac{di_d}{dt} - \frac{r_{Rd}'}{x_{Md}} \cdot \psi_{Rd} + r_{Rd}' \cdot i_f + k_{fD} \cdot (u_f - r_f \cdot i_f) - n \cdot \psi_q$$

$$\text{(A.38)}$$

$$u_q = r_q'' \cdot i_q + \frac{x_q''}{\omega_n} \cdot \frac{di_q}{dt} - \frac{r_{Rq}}{x_{Mq}} \cdot \psi_{Rq} + n \cdot \psi_d \tag{A.39}$$

$$u_f = r_f'' \cdot i_f + \frac{x_f''}{\omega_n} \frac{di_f}{dt} - \frac{r_{Rd}''}{x_{Md}} \cdot \psi_{Rd} + r_{Rd}'' \cdot i_d + k_{dD} \cdot (u_d - r_s \cdot i_d + n \cdot \psi_q)$$

$$\text{(A.40)}$$

$$T_D \cdot \frac{d\psi_{Rd}}{dt} = -\psi_{Rd} + x_{Md} \cdot (i_d + i_f) \tag{A.41}$$

$$T_Q \cdot \frac{d\psi_{Rq}}{dt} = -\psi_{Rq} + x_{Mq} \cdot i_q \tag{A.42}$$

where,

$$\psi_{Rd} = \frac{\psi_D}{1+\sigma_D} \tag{A.43}$$

$$\psi_{Rq} = \frac{\psi_Q}{1+\sigma_Q} \tag{A.44}$$

$$r_{Rd} = \frac{r_D}{(1+\sigma_D)^2} \tag{A.45}$$

$$r_{Rq} = \frac{r_Q}{(1+\sigma_Q)^2} \tag{A.46}$$

$$x_{Md} = \frac{x_{md}}{(1+\sigma_D)} \tag{A.47}$$

$$x_{Mq} = \frac{x_{mq}}{(1+\sigma_Q)} \tag{A.48}$$

$$T_D = \frac{x_{Md}}{\omega_n r_{Rd}} \tag{A.49}$$

$$T_Q = \frac{x_{Mq}}{\omega_n r_{Rq}} \tag{A.50}$$

$$r_d'' = r_s + (1 - k_{fD}) \cdot \frac{r_D}{(1 + \sigma_D)^2} = r_s + \frac{r_D}{\left(1 + \sigma_D + \frac{\sigma_D}{\sigma_f}\right) \cdot (1 + \sigma_D)} \quad \text{(A.51)}$$

$$r_f'' = r_f + (1 - k_{dD}) \cdot \frac{r_D}{(1 + \sigma_D)^2} = r_f + \frac{r_D}{\left(1 + \sigma_D + \frac{\sigma_D}{\sigma_d}\right) \cdot (1 + \sigma_D)} \quad \text{(A.52)}$$

$$k_{fD} = \frac{\sigma_D}{\sigma_f \cdot \left(1 + \sigma_D + \frac{\sigma_D}{\sigma_f}\right)} \quad \text{(A.53)}$$

$$k_{dD} = \frac{\sigma_D}{\sigma_d \cdot \left(1 + \sigma_D + \frac{\sigma_D}{\sigma_d}\right)} \quad \text{(A.54)}$$

The voltage equations in (A.38)–(A.40) consist only of the currents as the state variables. Therefore, it becomes easy to apply Modulus Optimum for tuning the controller parameters. The remaining terms in the equations can be used as feed-forward in the controller to enhance the dynamic performance. In a Proportional-Integral controller, this is compensated by the integrated term if the feed-forward terms are not implemented.

Appendix B

Design Rules for PI controllers

B.1   Modulus optimum

The open-loop transfer function of a system with a PI controller, a converter, and a plant with significant damping can be presented as follows:

$$h_o\left(s\right) = K_p \frac{1 + T_i \cdot s}{T_i \cdot s} \cdot K_s \cdot \frac{1}{1 + T_{sum} \cdot s} \cdot \frac{1}{1 + T_1 \cdot s} \tag{B.1}$$

where the first part of the transfer function $K_p \frac{1 + T_i s}{T_i s}$ is the PI controller, K_s is the gain or amplification of the system, $\frac{1}{1 + T_{sum}s}$ is the delay in the system due to converter and filtering mechanism, and $\frac{1}{1 + T_1 s}$ is the transfer function of the plant. Normally, T_1 contributes to the most dominating pole in the system because it is much larger compared to the time delay in the converter and the filter. Therefore, while designing the controller, the time constant of the controller (T_i) is chosen such that it cancels the effect of T_1. Further, the gain (K_p) is chosen such that the closed loop system will have a relative damping of $\frac{1}{\sqrt{2}}$, i.e.:

$$K_p = \frac{T_1}{2 K_s T_{sum}}$$
$$T_i = T_1 \tag{B.2}$$

The tuning method is known as Modulus Optimum. When a full step change of 1 is applied in the input to such a system, the controller tuned using this method yields a rise time of $T_{rise} = 4.7 \cdot T_{sum}$, overshoot of 4.7%, and settling time of $8.4 \cdot T_{sum}$. The method is an excerpt from [97].

B.2   Symmetrical optimum

When the time constant, T_1, is dominant compared to the damping in the process (e.g., the acceleration of a machine or charging of a large capacitor), the open loop transfer function of the system is:

$$h_o\left(s\right) = K_p \frac{1 + T_i \cdot s}{T_i \cdot s} \cdot K_s \cdot \frac{1}{1 + T_{sum} \cdot s} \cdot \frac{1}{T_1 \cdot s} \tag{B.3}$$

where the first part of the transfer function $K_p \frac{1+T_i s}{T_i s}$ is the PI controller, K_s is the gain or amplification of the system, $\frac{1}{1+T_{sum}s}$ is the delay in the system due to converter and filtering mechanism, and $\frac{1}{T_1 s}$ is the integrator of the process. Normally, T_1 contributes to the most dominating pole in the system because it is much larger compared to the time delay in the converter and the filter. Since the transfer function consists of two integrators, the application of the Modulus Optimum criterion will lead to two poles at zero frequency, which gives a phase margin of 0, i.e., a phase shift of $-180°$ when the amplitude of $h_o(s)$ is 1. Therefore, another criterion called Symmetrical Optimum needs to be employed. The gain and time constant of the controller are designed as follows:

$$K_p = \frac{T_1}{\sqrt{\beta} K_s T_{sum}}$$

$$T_i = \beta T_{sum} \tag{B.4}$$

The selection of the controller parameters increases the phase margin in the reason of $\frac{1}{\beta T_{sum}}$ and $1/T_{sum}$ with the highest phase margin occurring at $\frac{1}{\sqrt{\beta} T_{sum}}$. The constant β is selected such that the undershoot in the system response due to load or disturbance is minimum even though this yields a high overshoot for the step input. With $\beta = 4$, the step response has a rise time of $T_{rise} = 3.1 \cdot T_{sum}$, an overshoot of 43%, and a settling time of $16.5 \cdot T_{sum}$. A filter or a ramp function is normally used to avoid overshoot due to changes in input. A higher value of β is chosen when a very fast rise time is not a requirement.

Appendix C

Control Strategies for Synchronous Machine

C.1 Unity power factor control
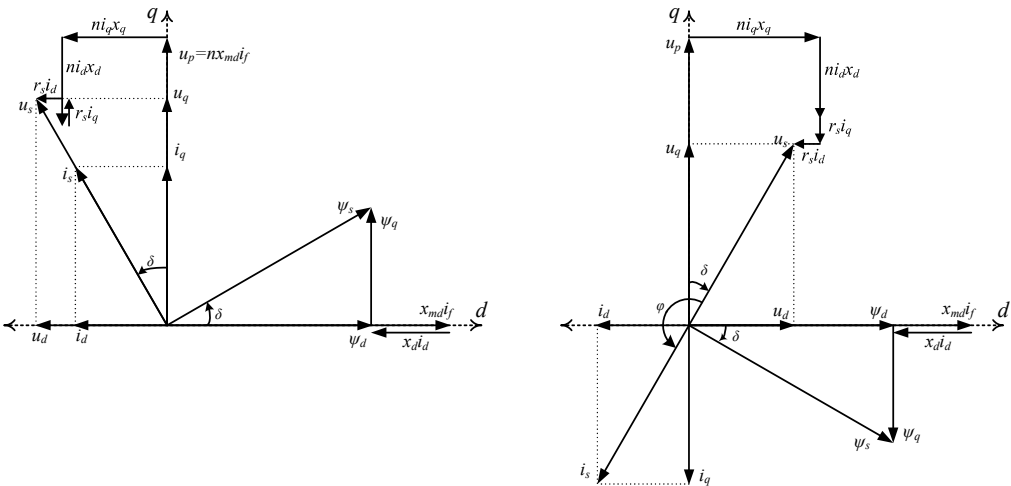
Figure C.1: Phasor diagram of unity power factor control of a synchronous machine.

From the phasor diagram for motor mode operation from Fig. C.1:

$$\tan \delta = \frac{u_d}{u_q} = \frac{i_d}{i_q} \tag{C.1}$$

From (C.1):

$$u_d i_q = u_q i_d \tag{C.2}$$

Substituting u_d and u_q from (4.9) in (C.2):

$$(r_s i_d - n\psi_q)\, i_q = (r_s i_q + n\psi_\mathrm{d})\, i_d \tag{C.3}$$

Since the stator resistance is very small, it can be neglected for simplified expression, and (C.3):

$$\psi_d i_d = -\psi_q i_q \tag{C.4}$$

The torque equation is:

$$\tau_e = \psi_d i_q - \psi_q i_d \tag{C.5}$$

Multiplying both sides of (C.5) by i_d and i_q:

$$\begin{aligned} \tau_e i_d &= \psi_d i_q i_d - \psi_q i_d^2 \\ \tau_e i_q &= \psi_d i_q^2 - \psi_q i_d i_q \end{aligned} \tag{C.6}$$

Substituting (C.4) in (C.6):

$$\begin{aligned} \tau_e i_d &= \psi_d i_q i_d - \psi_q i_d^2 = -\psi_q i_q^2 - \psi_q i_d^2 = -\psi_q \left(i_q^2 + i_d^2\right) \\ \tau_e i_q &= \psi_d i_q^2 - \psi_q i_d i_q = \psi_d i_q^2 + \psi_d i_d^2 = \psi_d \left(i_q^2 + i_d^2\right) \end{aligned} \tag{C.7}$$

Squaring and adding the two parts of (C.7) and using the relation $i_s^2 = i_d^2 + i_q^2$ and $\psi_s^2 = \psi_d^2 + \psi_q^2$:

$$\begin{aligned} \tau_e^2 \left(i_d^2 + i_q^2\right) &= \left(\psi_d^2 + \psi_q^2\right) i_s^4 \\ \Rightarrow \tau_e^2 i_s^2 &= \psi_s^2 i_s^4 \end{aligned} \tag{C.8}$$

$$\tau_e = \pm \psi_s i_s \tag{C.9}$$

The positive sign is used for motor operation, whereas the negative sign is used for generator operation.

From the vector diagram, the necessary condition that needs to be met for $\cos\varphi = 1$ operation is:

$$\tan\delta = -\frac{u_d}{u_q} = \frac{n\psi_q - r_s i_d}{n\psi_d - r_s i_q} \tag{C.10}$$

As assumed earlier, stator resistance (r_s) can be neglected for simplicity and (C.7) becomes:

$$\tan \delta = \frac{\psi_q}{\psi_d} = \frac{x_q i_q}{x_{md} i_f + x_d i_d} \tag{C.11}$$

From the phasor diagram:

$$\begin{aligned} i_d &= - i_s \cdot \sin \delta \\ i_q &= i_s \cdot \cos \delta \end{aligned} \tag{C.12}$$

Substituting (C.12) in (C.11):

$$\tan \delta = \frac{x_q i_q}{x_{md} i_f + x_d i_d} = \frac{x_q i_s \cos \delta}{x_{md} i_f - x_d i_s \sin \delta} \tag{C.13}$$

Solving (C.13) for i_f:

$$i_f = \frac{1}{x_{md}} \left(\frac{x_q i_s \cos^2 \delta}{\sin \delta} + x_d i_s \sin \delta \right) \tag{C.14}$$

From the stator flux relation:

$$\psi_s^2 = \psi_d^2 + \psi_q^2 = (\psi_f - x_d i_s \sin \delta)^2 + (x_q i_s \cos \delta)^2 \tag{C.15}$$

Substituting (C.14) in (C.15):

$$\psi_s^2 = \left(\frac{x_q i_s \cos^2 \delta}{\sin \delta} \right)^2 + (x_q i_s \cos \delta)^2 = x_q^2 i_s^2 \cos^2 \delta \left(\frac{\cos^2 \delta}{\sin^2 \delta} + 1 \right) = \frac{x_q^2 i_s^2}{\tan^2 \delta} \tag{C.16}$$

From (C.9) and (C.16):

$$\tan \delta = \pm \frac{x_q i_s}{\psi_s} = \frac{\tau_e x_q}{\psi_s^2} \tag{C.17}$$

The pole wheel angle (δ) is positive for motor operation and negative for generator operation.

Now, substituting $x_q i_s = \psi_s \tan \delta$ from (C.17) in (C.14):

$$i_f = \frac{1}{x_{md}} (\psi_s \cos \delta + x_d i_s \sin \delta) \tag{C.18}$$

The value of $\cos \delta$ and $\sin \delta$ from (C.17):

$$\cos \delta = \frac{\psi_s}{\sqrt{\psi_s^2 + x_q^2 i_s^2}}$$

$$\sin \delta = \frac{x_q i_s}{\sqrt{\psi_s^2 + x_q^2 i_s^2}}$$

(C.19)

Substituting the value of $\cos \delta$ and $\sin \delta$ from (C.19) in (C.18):

$$x_{md} i_f = \psi_s \frac{\psi_s}{\sqrt{\psi_s^2 + x_q^2 i_s^2}} + x_d i_s \frac{x_q i_s}{\sqrt{\psi_s^2 + x_q^2 i_s^2}} = \frac{\psi_s^2 + x_d x_q i_s^2}{\sqrt{\psi_s^2 + x_q^2 i_s^2}}$$

(C.20)

Hence, for $\cos \varphi = 1$ control:

$$i_f = \frac{1}{x_{md}} \frac{\psi_s^2 + x_d x_q i_s^2}{\sqrt{\psi_s^2 + x_q^2 i_s^2}}$$

(C.21)

C.2   Maximum torque per ampere control

In this method, the stator current can be impressed in the second quadrant such that reluctance torque can be utilized from the saliency of the machine. The field current is controlled in such a way that the stator flux is always constant (equal to 1 p.u.).

$$\tau_e = \psi_d i_q - \psi_q i_d$$

(C.22)

$$\psi_d = x_{md} i_f + x_d i_d$$
$$\psi_q = x_q i_q$$

(C.23)

$$\psi_s^2 = \psi_d^2 + \psi_q^2$$

(C.24)

$$\tau_e = i_q \sqrt{\psi_s^2 - \psi_q^2} - \psi_q i_d$$

(C.25)

$$\tau_e = i_q \sqrt{\psi_s^2 - x_q^2 i_q^2} - x_q i_q i_d$$

(C.26)

$$i_s^2 = i_d^2 + i_q^2$$

(C.27)

Figure C.2: Phasor diagram of maximum torque per ampere control of a synchronous machine.

$$\tau_e = i_q \sqrt{\psi_s^2 - x_q^2 i_q^2} - x_q i_q \sqrt{i_s^2 - i_q^2} \tag{C.28}$$

The value of i_q at which the maximum torque occurs can be derived by equating the derivative of (C.28) w.r.t. i_q and equating to zero:

$$
\begin{aligned}
\frac{d\tau_e}{di_q} &= \sqrt{\psi_s^2 - x_q^2 i_q^2} - \frac{x_q^2 i_q^2}{\sqrt{\psi_s^2 - x_q^2 i_q^2}} - x_q \sqrt{i_s^2 - i_q^2} + \frac{x_q i_q^2}{\sqrt{i_s^2 - i_q^2}} = 0 \\
&= \sqrt{\psi_s^2 - x_q^2 i_q^2} - \frac{x_q^2 i_q^2}{\sqrt{\psi_s^2 - x_q^2 i_q^2}} - x_q i_d + \frac{x_q i_q^2}{i_d} = 0
\end{aligned} \tag{C.29}
$$

Solving for i_d:

$$i_d = \frac{x_q \left(i_s^2 - 2i_q^2 \right) \sqrt{\psi_s^2 - x_q^2 i_q^2}}{\psi_s^2 - 2x_q^2 i_q^2} \tag{C.30}$$

Now, i_q in terms of i_s:

$$i_s^2 = i_d^2 + i_q^2 = \frac{x_q^2 \left(i_s^2 - 2i_q^2 \right)^2 \psi_s^2 - x_q^2 i_q^2}{\left(\psi_s^2 - 2x_q^2 i_q^2 \right)^2} + i_q^2 \tag{C.31}$$

Solving for i_q:

$$i_q = \pm \frac{\psi_s i_s}{\sqrt{\psi_s^2 + x_q^2 i_s^2}} \tag{C.32}$$

Using (C.32) to find ψ_d and ψ_q:

$$\psi_d = \sqrt{\psi_s^2 - \psi_q^2} = \sqrt{\psi_s^2 - x_q^2 i_q^2} = \frac{\psi_s^2}{\sqrt{\psi_s^2 + x_q^2 i_s^2}} \tag{C.33}$$

$$\psi_q = x_q i_q = \pm \frac{x_q i_s \psi_s}{\sqrt{\psi_s^2 + x_q^2 i_s^2}} \tag{C.34}$$

Substituting (C.32) in (C.30) to find i_d in terms of i_s:

$$i_d = \frac{-x_q i_s^2}{\sqrt{\psi_s^2 + x_q^2 i_s^2}} \tag{C.35}$$

The maximum torque for any given i_s is:

$$\tau_e = \psi_d i_q - \psi_q i_d = \pm \psi_s i_s \tag{C.36}$$

From (C.23):

$$x_{md} i_f = \psi_d - x_d i_d = \frac{\psi_s^2 + x_d x_q i_s^2}{\sqrt{\psi_s^2 + x_q^2 i_s^2}} \tag{C.37}$$

Hence, the field current (i_f) to achieve the given ψ_s and i_s is:

$$i_f = \frac{\psi_s^2 + x_d x_q i_s^2}{x_{md} \sqrt{\psi_s^2 + x_q^2 i_s^2}} \tag{C.38}$$

From phasor diagram:

$$\tan(\delta - \varphi) = \frac{i_d}{i_q} = \frac{x_q i_s}{\psi_s} \tag{C.39}$$

and also,

$$\tan \delta = \frac{\psi_d}{\psi_q} = \frac{x_q i_s}{\psi_s} \tag{C.40}$$

From (C.39) and (C.40), it can be observed that $\delta - \varphi = \delta$, i.e., $\varphi = 0$. This shows that maximum torque always occurs with $\varphi = 0$, i.e. maximum torque per ampere (MTPA) control and unity power factor ($\cos \varphi = 1$) control are the same.

Appendix D

Analytical Loss Equations

D.1   Loss equations for NPC converter

$$I_{T1,avg} = \frac{M\hat{I}_o}{4} \cos\varphi + \frac{M\hat{I}_o}{4\pi} \left(\sin|\varphi| - |\varphi|\cos\varphi\right) \tag{D.1}$$

$$I_{D1,avg} = \frac{M\hat{I}_o}{4\pi} \left(\sin|\varphi| - |\varphi|\cos\varphi\right) \tag{D.2}$$

$$I_{T1,rms}^2 = \frac{M\hat{I}_o^2}{6\pi} (1 + \cos\varphi)^2 \tag{D.3}$$

$$I_{D1,rms}^2 = \frac{M\hat{I}_o^2}{6\pi} (1 - \cos\varphi)^2 \tag{D.4}$$

The current through the devices T_1 and D_1 in the NPC and ANPC converter configurations are the same, and therefore, the average and rms currents and hence, the conduction loss in these devices, would be the same in both cases.

The similar expressions for the average and rms currents through the devices T_2, D_2, and D_5 are:

In the NPC converter, diode D_1 and D_2 conduct simultaneously and have the same average and rms current flowing through them:

$$I_{D5,avg,npc} = \frac{1}{2\pi} \int\limits_{3\pi/2+\varphi}^{5\pi/2+\varphi} i_a d\omega t - I_{T1,avg} - I_{D1,avg}$$

$$= \frac{\hat{I}_o}{\pi} \left[1 - \frac{M}{2} \left(\sin|\varphi| + \left(\frac{\pi}{2} - |\varphi| \right) \cos\varphi \right) \right] \tag{D.5}$$

$$I_{D5,rms,npc}^2 = \frac{1}{2\pi} \int\limits_{3\pi/2+\varphi}^{5\pi/2+\varphi} i_a^2 d\omega t - I_{T1,rms}^2 - I_{D1,rms}^2$$

$$= \frac{\hat{I}_o^2}{4} \left[1 - \frac{4M}{3\pi} \left(1 + \cos^2\varphi \right) \right] \tag{D.6}$$

$$I_{T2,avg,npc} = I_{T1,avg,npc} + I_{D5,avg,npc}$$

$$= \frac{\hat{I}_o}{\pi} \left[1 - \frac{M}{4} \left(\sin|\varphi| - |\varphi|\cos\varphi \right) \right] \tag{D.7}$$

$$I_{T2,rms,npc}^2 = I_{T1,rms,npc}^2 + I_{D5,rms,npc}^2$$

$$= \frac{\hat{I}_o^2}{4} \left[1 - \frac{2M}{3\pi} (1 - \cos\varphi)^2 \right] \tag{D.8}$$

D.1.1   Switching loss

The switching loss characteristics as a function of current, $e_{sw}(i)$, from an experimental result, can be approximated as:

$$e_{sw}(i) = k_{1,T} \cdot i + k_{2,T} \cdot i^2 \tag{D.9}$$

where $k_{1,T}$ and $k_{2,T}$ are the curve fitting coefficients determined using the experimental results or manufacturer's datasheet. The same coefficients for diodes are $k_{1,D}$ and $k_{2,D}$.

Using these coefficients, the expressions for calculating the switching loss in each device can be formulated:

$$P_{T1,sw,npc} = \frac{U_{dc}}{2U_{dc}^*} \frac{1}{2\pi} f_{sw} \int_{3\pi/2+\varphi}^{5\pi/2} \left(k_{1,T}i + k_{2,T}i^2 \right) d\omega t$$

$$= \frac{U_{dc}}{2U_{dc}^*} \frac{\hat{I}_o}{2\pi} f_{sw} \left[k_{1,T} \left(1 + \cos\varphi \right) + \frac{\hat{I}_o}{2} k_{2,T} \left(\pi - |\varphi| + \frac{1}{2}\sin 2|\varphi| \right) \right] \tag{D.10}$$

$$
\begin{aligned}
P_{D1,sw,npc} &= \frac{U_{dc}}{2U_{dc}^*} \frac{1}{2\pi} f_{sw} \int_{3\pi/2}^{3\pi/2+\varphi} \left(k_{1,D}i + k_{2,D}i^2\right) d\omega t \\
&= \frac{U_{dc}}{2U_{dc}^*} \frac{\hat{I}_o}{2\pi} f_{sw} \left[k_{1,D}\left(1 - \cos\varphi\right) + \frac{\hat{I}_o}{2}k_{2,D}\left(|\varphi| - \frac{1}{2}\sin 2|\varphi|\right)\right]
\end{aligned}
$$
(D.11)

The equation for switching loss in devices T_1 and D_1 in the ANPC converter is the same as that in the NPC converter. Therefore, (D.10) and (D.1.1) are valid for the ANPC converter as well.

$$
\begin{aligned}
P_{T2,sw,npc} &= \frac{U_{dc}}{2U_{dc}^*} \frac{1}{2\pi} f_{sw} \int_{5\pi/2}^{5\pi/2+\varphi} \left(k_{1,T}i + k_{2,T}i^2\right) d\omega t \\
&= \frac{U_{dc}}{2U_{dc}^*} \frac{\hat{I}_o}{2\pi} f_{sw} \left[k_{1,T}\left(1 - \cos\varphi\right) + \frac{\hat{I}_o}{2}k_{2,T}\left(|\varphi| - \frac{1}{2}\sin 2|\varphi|\right)\right]
\end{aligned}
$$
(D.12)

In case of the ANPC converter, $\hat{I}_o$ is replaced by $\hat{I}_o/2$ in (D.12) to calculate the switching loss in the switches T_2 and T_5.

$$
P_{D2,sw,npc} = 0
$$
(D.13)

$$
\begin{aligned}
P_{D5,sw,npc} &= \frac{U_{dc}}{2U_{dc}^*} \frac{1}{2\pi} f_{sw} \int_{3\pi/2+\varphi}^{5\pi/2} \left(k_{1,D}i + k_{2,D}i^2\right) d\omega t \\
&= \frac{U_{dc}}{2U_{dc}^*} \frac{\hat{I}_o}{2\pi} f_{sw} \left[k_{1,D}\left(1 + \cos\varphi\right) + \frac{\hat{I}_o}{2}k_{2,D}\left(\pi - |\varphi| + \frac{1}{2}\sin 2|\varphi|\right)\right]
\end{aligned}
$$
(D.14)

For the semiconductor devices in the ANPC converter, $\hat{I}_o$ is replaced by $\hat{I}_o/2$ in (D.14) to find the switching loss in the diodes D_2 and D_5.

D.2 Loss equations for ANPC converter

D.2.1 Equations for calculation of average and RMS currents

$$
\begin{aligned}
I_{T1,avg} &= \frac{1}{2\pi} \int\limits_{3\pi/2+\varphi}^{5\pi/2} m_a i_a d\omega t \\
&= \frac{M\hat{I}_o}{4}\cos\varphi + \frac{M\hat{I}_o}{4\pi}\left(\sin|\varphi| - |\varphi|\cos\varphi\right)
\end{aligned}
$$
(D.15)

$$I_{T1,rms}^2 = \frac{1}{2\pi} \int_{3\pi/2+\varphi}^{5\pi/2} m_a i_a^2 d\omega t \tag{D.16}$$

$$= \frac{M\hat{I}_o^2}{6\pi} (1 + \cos\varphi)^2$$

$$I_{D1,avg} = \frac{1}{2\pi} \int_{3\pi/2}^{3\pi/2+\varphi} (-m_a i_a) \, d\omega t \tag{D.17}$$

$$= \frac{M\hat{I}_o}{4\pi} [\sin|\varphi| - |\varphi|\cos\varphi]$$

$$I_{D1,rms}^2 = \frac{1}{2\pi} \int_{3\pi/2}^{3\pi/2+\varphi} m_a i_a^2 d\omega t \tag{D.18}$$

$$= \frac{M\hat{I}_o^2}{6\pi} (1 - \cos\varphi)^2$$

The equations (5.25)–(5.32) can be used to calculate the average and rms current through the other semiconductor devices:

$$I_{T5,avg} = \frac{1}{2\pi} \int_{3\pi/2+\varphi}^{5\pi/2+\varphi} \frac{1}{2} i_a d\omega t - \frac{1}{2} I_{T1,avg} - \frac{1}{2} I_{D1,avg} \tag{D.19}$$

$$= \frac{\hat{I}_o}{2\pi} \left[1 - \frac{M}{2} \left(\sin|\varphi| + \left(\frac{\pi}{2} - |\varphi|\right)\cos\varphi\right)\right]$$

$$I_{T5,rms}^2 = \frac{1}{2\pi} \int_{3\pi/2+\varphi}^{5\pi/2+\varphi} \frac{1}{4} i_a^2 d\omega t - \frac{1}{4} I_{T1,rms}^2 - \frac{1}{4} I_{D1,rms}^2 \tag{D.20}$$

$$= \frac{\hat{I}_o^2}{16} \left[1 - \frac{4M}{3\pi} \left(1 + \cos^2\varphi\right)\right]$$

$$I_{D5,avg} = \frac{1}{2\pi} \int_{3\pi/2+\varphi}^{5\pi/2+\varphi} \frac{1}{2} i_a d\omega t - \frac{1}{2} I_{T1,avg} - \frac{1}{2} I_{D1,avg} \tag{D.21}$$

$$= \frac{\hat{I}_o}{2\pi} \left[1 - \frac{M}{2} \left(\sin|\varphi| + \left(\frac{\pi}{2} - |\varphi|\right)\cos\varphi\right)\right]$$

$$I_{D5,rms}^2 = \frac{1}{2\pi} \int_{3\pi/2+\varphi}^{5\pi/2+\varphi} \frac{1}{4} i_a^2 d\omega t - \frac{1}{4} I_{T1,rms}^2 - \frac{1}{4} I_{D1,rms}^2$$

$$= \frac{\hat{I}_o^2}{16} \left[1 - \frac{4M}{3\pi} \left(1 + \cos^2\varphi \right) \right]$$

(D.22)

$$I_{T2,avg} = I_{T1,avg} + I_{D5,avg}$$

$$= \frac{\hat{I}_o}{2\pi} + \frac{M\hat{I}_o}{8} \cos\varphi$$

(D.23)

$$I_{T2,rms}^2 = I_{T1,rms}^2 + I_{D5,rms}^2$$

$$= \frac{\hat{I}_o^2}{4} \left[\frac{1}{4} + \frac{M}{3\pi} \left(1 + \cos^2\varphi + 4\cos\varphi \right) \right]$$

(D.24)

$$I_{D2,avg} = I_{T5,avg} + I_{D1,avg}$$

$$= \frac{\hat{I}_o}{2\pi} - \frac{M\hat{I}_o}{8} \cos\varphi$$

(D.25)

$$I_{D2,rms}^2 = I_{T5,rms}^2 + I_{D1,rms}^2$$

$$= \frac{\hat{I}_o^2}{4} \left[\frac{1}{4} + \frac{M}{3\pi} \left(1 + \cos^2\varphi - 4\cos\varphi \right) \right]$$

(D.26)

D.2.2 Equations for calculation of switching loss

$$P_{T1,sw} = \frac{U_{dc}}{2U_{dc}^*} \frac{1}{2\pi} f_{sw} \int_{3\pi/2+\varphi}^{5\pi/2} \left(k_{1,T} i + k_{2,T} i^2 \right) d\omega t$$

$$= \frac{U_{dc}}{2U_{dc}^*} \frac{\hat{I}_o}{2\pi} f_{sw} \left[k_{1,T} \left(1 + \cos\varphi \right) + \frac{\hat{I}_o}{2} k_{2,T} \left(\pi - |\varphi| + \frac{1}{2} \sin 2|\varphi| \right) \right]$$

(D.27)

where U_{dc} is the dc-link voltage as shown in Fig. 5.5 and U_{dc}^* is the rated blocking voltage of the device given in the datasheet:

$$P_{D1,sw} = \frac{U_{dc}}{2U_{dc}^*} \frac{1}{2\pi} f_{sw} \int_{3\pi/2}^{3\pi/2+\varphi} \left(k_{1,D} i + k_{2,D} i^2 \right) d\omega t$$

$$= \frac{U_{dc}}{2U_{dc}^*} \frac{\hat{I}_o}{2\pi} f_{sw} \left[k_{1,D} \left(1 - \cos\varphi \right) + \frac{\hat{I}_o}{2} k_{2,D} \left(|\varphi| - \frac{1}{2} \sin 2|\varphi| \right) \right]$$

(D.28)

In sinusoidal PWM modulation, the switch T_2 is continuously "ON" during the interval $3\pi/2$ to $5\pi/2$ ($t = 0.015s$ to $0.035s$ in Fig. 5.6). Therefore, T_2 will have switching loss only if the output current is leading or lagging the modulation signal, m_a, i.e., outside the aforementioned interval:

$$
\begin{aligned}
P_{T2,sw} &= \frac{U_{dc}}{2U_{dc}^*}\frac{1}{2\pi} f_{sw} \int_{5\pi/2}^{5\pi/2+\varphi} \left(k_{1,T}i + k_{2,T}i^2 \right) d\omega t \\
&= \frac{U_{dc}}{2U_{dc}^*} \cdot \frac{\hat{I}_o}{4\pi} f_{sw} \left[k_{1,T}\left(1 - \cos\varphi \right) + \frac{\hat{I}_o}{4} k_{2,T} \left(|\varphi| - \frac{1}{2}\sin 2\,|\varphi| \right) \right]
\end{aligned}
$$
(D.29)

$$
\begin{aligned}
P_{D5,sw} &= \frac{U_{dc}}{2U_{dc}^*}\frac{1}{2\pi} f_{sw} \int_{3\pi/2\,+\varphi}^{5\pi/2} \left(k_{1,D}i + k_{2,D}i^2 \right) d\omega t \\
&= \frac{U_{dc}}{2U_{dc}^*}\frac{\hat{I}_o}{4\pi} f_{sw} \left[k_{1,D}\left(1 + \cos\varphi \right) + \frac{\hat{I}_o}{4} k_{2,D} \left(\pi - |\varphi| + \frac{1}{2}\sin 2\,|\varphi| \right) \right]
\end{aligned}
$$
(D.30)

The diodes D_2 and D_5 have the same switching pattern but in different half cycles; therefore, the switching loss over a cycle in these diodes is equal. The same applies to the switches T_2 and T_5.

Appendix E

Dynamics of DC-link Voltage

E.1 Voltage equation for dc-link capacitor

The voltage across the dc-link capacitor is:

$$u_{dc} = \frac{1}{C_{dc}} \int i_{cap} dt \qquad \text{(E.1)}$$

Since the machine-side converter is controlling the dc-link voltage, the dc current on the grid-side converter (i_{dc2}) can be regarded as the disturbance and can be omitted from the equation for this analysis.

The voltage across the dc-link capacitor is:

$$C_{dc} \frac{du_{dc}}{dt} = i_{cap} = -i_{dc1} \qquad \text{(E.2)}$$
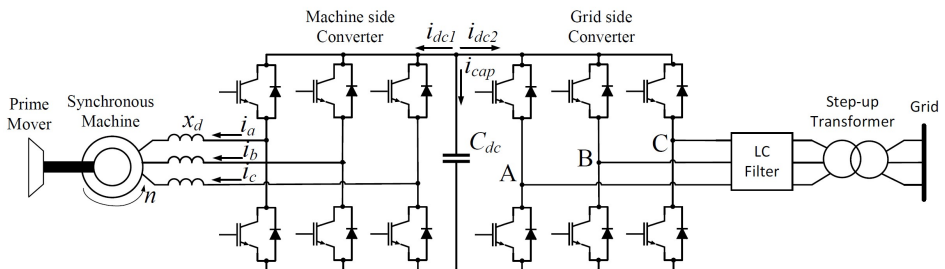
Figure E.1: Schematic of the synchronous machine connected to the grid via a back-to-back two-level three-phase converter.

The per unitized form of (E.2) using time constant T_{dc}, like the mechanical time constant in a motor:

$$T_{dc} \frac{du_{dc,pu}}{dt} = i_{cap} = -i_{dc1} \tag{E.3}$$

The base values for ac quantities for per-unit calculation are selected as follows:

$$I_{base} = \sqrt{2} I_{rms}, \quad U_{base} = \frac{\sqrt{2} U_{ll,rms}}{\sqrt{3}}, \quad \omega_{base} = 2\pi f$$

$$Z_{base} = \frac{U_{base}}{I_{base}} = \frac{1}{\sqrt{3}} \frac{U_{ll,rms}}{I_{rms}} = \frac{U_{ph,rms}}{I_{rms}} \tag{E.4}$$

$$S_{base} = \sqrt{3} U_{ll,rms} I_{rms} = \sqrt{3} \cdot \frac{\sqrt{3} U_{base}}{\sqrt{2}} \cdot \frac{I_{base}}{\sqrt{2}} = \frac{3}{2} U_{base} I_{base}$$

Further, the base values for the dc quantities per-unit calculation are selected as follows:

$$S_{base} = \frac{3}{2} U_{base} I_{base} = U_{dc,base} I_{dc,base} \tag{E.5}$$

In a PWM-modulated converter, for linear modulation, M=1 gives the maximum output voltage:

$$U_{dc,base} = 2 \cdot U_{ph,peak} = 2 \cdot U_{base} \tag{E.6}$$

Using (E.5) and (E.6):

$$Z_{dc,base} = \frac{U_{dc,base}}{I_{dc,base}} = \frac{2 \cdot U_{base}}{\frac{3}{4} I_{base}} = \frac{8}{3} \frac{U_{base}}{I_{base}} = \frac{8}{3} Z_{base} \tag{E.7}$$

Similarly, the time constant of the dc-link capacitor:

$$T_{dc} = \frac{2 * Energy\ stored}{Rated\ power} = \frac{C_{dc} \cdot U_{dc}^2}{S_{base}} = \frac{C_{dc} \cdot 4 U_{base}^2}{\frac{3}{2} U_{base} I_{base}}$$

$$= C_{dc} \cdot \frac{8}{3} \frac{U_{base}}{I_{base}} = C_{dc} \cdot \frac{8}{3} Z_{base} = C_{dc} \cdot Z_{dc,base} \tag{E.8}$$

From ac and dc side power balance:

$$p = u_{dc} \cdot i_{dc} = n \cdot \tau_e \tag{E.9}$$

Formulation of the equation in the per-unit system using (4.46):

$$T_{dc} \frac{du_{dc}}{dt} = i_{cap} = -i_{dc1} - i_{dc2} \tag{E.10}$$

Appendix F

Laboratory Equipment Specifications

F.1 Synchronous machine parameters

Table F.1: Specification of electrical equipment of the experimental setup.

Synchronous machine specification	
Rated power	100 kVA
Rated voltage	400 V
Rated current	144.3 A
Rated speed	428.57 rpm
x_d	1.27 pu
x_q	0.75 pu
x_d'	0.8 pu
x_d''	0.3359 pu
x_q''	0.3176 pu
T_d'	N/A
T_d''	4.6 ms
T_q''	4.27 ms
Rated excitation current (I_f)	56 A

F.2   Converter specification

Table F.2: Specification of electrical equipment of the experimental setup.

Converter specification - grid side	
Rated power	100 kVA
Rated dc-link voltage (U_{dc})	650 V
dc-link capacitor (C_{dc})	1.5 mF
Switching frequency (f_{sw})	4 kHz
Converter-side inductor (L_1)	$0.4\ mH$
AC side capacitor (C_{ac})	$27.9\ \mu F \Delta$
Grid-side inductor (L_2)	$18\ mH$

All the converters are identical. The machine-side converter outputs are directly connected to the machines, whereas the grid-side converters are connected to the grid via an L-C-L filter.

F.3   Induction machine specification

Table F.3: Specification of electrical equipment of the experimental setup.

Induction machine specification	
Rated power	90 kW
Rated voltage	400 V
Rated current	165 A
Power factor (p.f.)	0.83
Rated speed	1482 rpm

The induction machine is coupled to the synchronous machine via a gear with a gear ratio of 3.717.

NTNU
Norwegian University of
Science and Technology